UC Berkeley
UC Berkeley Electronic Theses and Dissertations

## Title

Studies in ancient and novel human pathogens: Mycobacterium tuberculosis and the epsilon variants of SARS-CoV-2

## Permalink

https://escholarship.org/uc/item/40f4f4r1

## Author

Fox, Douglas Michael

## Publication Date

2021

Peer reviewed|Thesis/dissertation

eScholarship.org Powered by the California Digital Library
University of California

# Studies in ancient and novel human pathogens: *Mycobacterium tuberculosis* and the epsilon variants of SARS-CoV-2

By

Douglas Michael Fox

A dissertation submitted in partial satisfaction of the

requirements for the degree of

Doctor of Philosophy

in

Chemistry

in the

Graduate Division

of the

University of California, Berkeley

Committee in charge:

Professor Matthew Francis Co-Chair
Professor Sarah Stanley Co-Chair
Professor Michael Marletta
Professor Daniel Portnoy

Fall 2021

Studies in ancient and novel human pathogens: *Mycobacterium tuberculosis* and the epsilon variants of SARS-CoV-2

© 2021

By Douglas Michael Fox

ABSTRACT

Studies in ancient and novel human pathogens: *Mycobacterium tuberculosis* and the epsilon variants of SARS-CoV-2.

by

Douglas Michael Fox

Doctor of Philosophy in Chemistry

University of California, Berkeley

Professor Matthew Francis, Co-Chair

Professor Sarah Stanley, Co-Chair

Tuberculosis (TB) is a deadly disease that has afflicted humankind throughout history and pre-history before becoming endemic in many parts of the world by the end of the 19$^{th}$ century. Following the discovery of *Mycobacterium tuberculosis (Mtb)* as the causative agent of tuberculosis by Robert Koch in 1882 TB began to be brought under control by a combination of the novel treatment methods (e.g. the sanatorium movement), increasing public health measures, the invention of a partially effective vaccine and, in the mid-20$^{th}$ century, the discovery of effective drugs and drug treatment regimens.

TB incidence has declined throughout the 20$^{th}$ century but remains the leading cause of death due to infectious disease worldwide causing about 1.5 million deaths per year. The failure to develop a fully effective vaccine and the emergence of multiply-, extensively-, and totally drug resistant strains are barriers to more effective TB control and highlight the need to develop novel treatment modalities based on a deeper understanding of *Mtb*'s unique physiology and intracellular niche.

Chapter 1 of this thesis explores *Mtb*'s use of the carbohydrate trehalose that *Mtb,* nearly uniquely among bacteria, utilizes for a variety of essential metabolic and structural purposes. The osmotic stress model demonstrates that *Mtb* regulates and controls its large pool of free trehalose. The results presented here suggest that a deeper understanding of the loci and methods of trehalose regulation and control may open avenues to undermine the fitness of mycobacterial pathogens *in vivo* and, ultimately, during human disease. In Chapter 2, a class of compounds called cationic amphiphilic drugs (CADs) are investigated for their ability to restrict the growth of intracellular *Mtb*.

In 2020 the novel human disease COVID-19 caused by the virus SARS-CoV-2 emerged to displace TB as the leading cause of infectious disease deaths worldwide. In January 2021, two

novel strains of SARS-CoV-2 (B.1.427 and B.1.149) emerged in California and were jointly designated as variants of concern (epsilon) by the World Health Organization. Chapter 3 presents the use of the Syrian hamster model to characterize the virulence, transmissibility, and susceptibility to pre-existing immunity of these variants *in vivo* relative to an earlier strain (B.1 [D614G]). In hamsters, epsilon was found to cause more severe disease and higher viral RNA levels in oropharyngeal swabs compared to B.1. These findings are consistent with human clinical and epidemiological data and help explain the emergence and rapid spread of this variant in early 2021.

TABLE OF CONTENTS


| | |
|---|---|
| Abstract | 1 |
| Table of Contents | i |
| Common Abbreviations | ii |
| Acknowledgements | iii |
| Chapter 1: Free trehalose (TRE) is regulated in *Mycobacterium spp.* under osmotic stress. | 1 |
| Chapter 2: Cationic amphiphilic drugs (CADs) restrict *Mycobacterium tuberculosis* in infected macrophages. | 21 |
| Chapter 3: Assessment of the *in vivo* virulence of B.1.427/1.429 (epsilon) SARS-CoV-2 variants relative to ancestral B.1 (614G). | 44 |

COMMON ABBREVIATIONS

| | |
|---|---|
| cLogP | Calculated octanol-water partition |
| BMM | Bone-marrow derived macrophage |
| CAD | Cationic amphiphilic drug |
| HPAEC-PAD | High performance anion exchange chromatography with pulsed amperometric detection |
| HPI | Hours post infection |
| MFI | Mean fluorescence intensity |
| MOI | Multiplicity of infection |
| *Mtb* | Mycobacterium tuberculosis |
| *Msmeg* | Mycobacterium smegmatis |
| pKa | $-\log_{10}(K_a)$ |
| PLD | Phospholipidosis |
| RLU | Relative luminescence units |
| Tre | Trehalose |
| Tre6P | Trehalose-6-phosphate |
| TMM | Trehalose monomycolate |
| TDM | Trehalose dimycolate |

ACKNOWLEDGEMENTS

The author wishes to express the deepest possible gratitude to Professor Sarah Stanley and great appreciation to Professor Benjamin Swarts, Professor M. Sloan Siegrist, Professor Kimberly Beatty, Professor Marc d'Alarcao, Dr. Kimberly Sogi, Dr. Lauren Wagner, Dr. Mason Appel, Ellen Levitan, Kimberly Fox and Caedmon Whitby.

**Chapter 1: Free trehalose (TRE) is regulated in *Mycobacterium spp* under osmotic stress.**

**Introduction**

Trehalose (Figure 1.1) is a non-reducing carbohydrate made up of two glucose molecules which are bound to each other as alpha glucosides. Trehalose is widely found in bacteria, fungi, plants and flying insects where it provides: (i) protection from numerous environmental stresses (osmotic stress, desiccation, and heat- and cold-shock); (ii) an internal carbon store in microbes; and (iii) a circulating carbon source in the hemolymph of flying insects.

Trehalose (Tre) is essential and highly abundant in all *Mycobacteria spp*. It is present in the cytosol in high concentrations as the free carbohydrate but is also abundantly present in the essential cell wall components, and highly immunostimulatory, glycolipids trehalose monomycolate (TMM) and trehalose dimycolate (TDM). Trehalose and trehalose glycolipids are also abundant in *Corynebacterium spp.* including the highly successful human pathogen *C. diptheria*. [1]

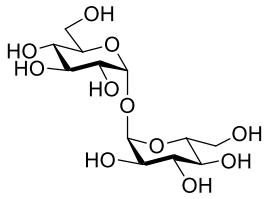



**Figure 1.1 Chemical structure of trehalose (α-D-glucopyranosyl-(1,1)-α-D-glucopyranoside).**

In addition to providing essential carbohydrates and glycolipids, trehalose sits at the intersection of, and may potentially regulate, several essential metabolic pathways (Figure 1.2). Most importantly trehalose drives the synthesis of outer membrane TMM and TDM. Trehalose can also be converted to linear alpha-glucan to supplement other anabolic pathways that create intracellular glycogen, another reservoir of intracellular carbon, and extracellular capsular glucan, which modulates *Mtb*'s interaction with the immune environment *in vivo* [2].

Trehalose also sits atop central carbon metabolism and can draw high energy sugars (glucose-6-phosphate and UDP-glucose) away from glycolysis or the synthesis of glycogen. Alternately, trehalose can be hydrolyzed by trehalase to two glucose molecules which can then be phosphorylated and fed into glycolysis.

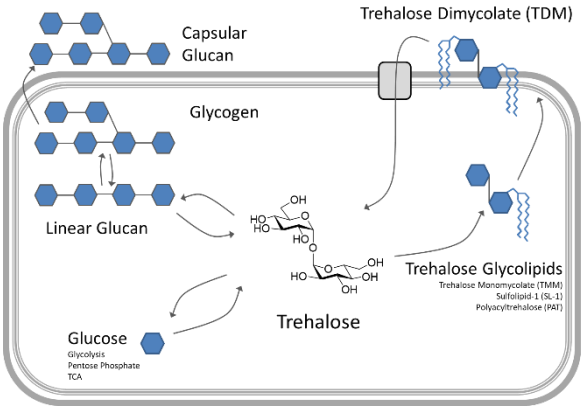



**Figure 1.2 Trehalose at the intersection of essential pathways in *Mycobacterium spp.***

There are three distinct biosynthetic pathways to produce trehalose in *Mycobacterium spp.* (Figure 1.3) [3, 4]. The *otsA-otsB* pathway utilizes glucose-6-phosphate and UDP-glucose to produce trehalose-6-phosphate (*otsA*) which is converted to trehalose by phosphatase OtsB. This is the most common pathway found in other organisms that use trehalose primarily for stress protection. Trehalose can also be produced by the catabolism of glycogen by the *treXYZ* pathway. Debranching by TreX is followed by conversion of the reducing end disaccharide from alpha 1,4 glucan to trehalose by TreY followed by hydrolysis of the terminal disaccharide by TreZ to produce free trehalose. Lastly, trehalose can be interconverted with maltose by TreS. This reaction is reversible and thermodynamically slightly favorable to trehalose formation. Maltose can be committed to glycogen synthesis, however, by the *pep2-glgE* pathway which forms maltose-1-phosphate which is activated to extend the non-reducing end of linear alpha-glucan [5,6]. Linear alpha-glucan is elaborated to branch glycogen and either retained intracellularly as a carbon source or exported to form capsular glucan.

The *otsA-otsB* and *treXYZ* pathways are unidirectional to form trehalose; the trehalase pathway is unidirectional to consume trehalose and produce glucose; and the *treS* pathway is, in principle, bi-directional. The degree of redundancy and flexibility that has evolved to form and utilize a single metabolite suggests how essential trehalose is to mycobacterial physiology.

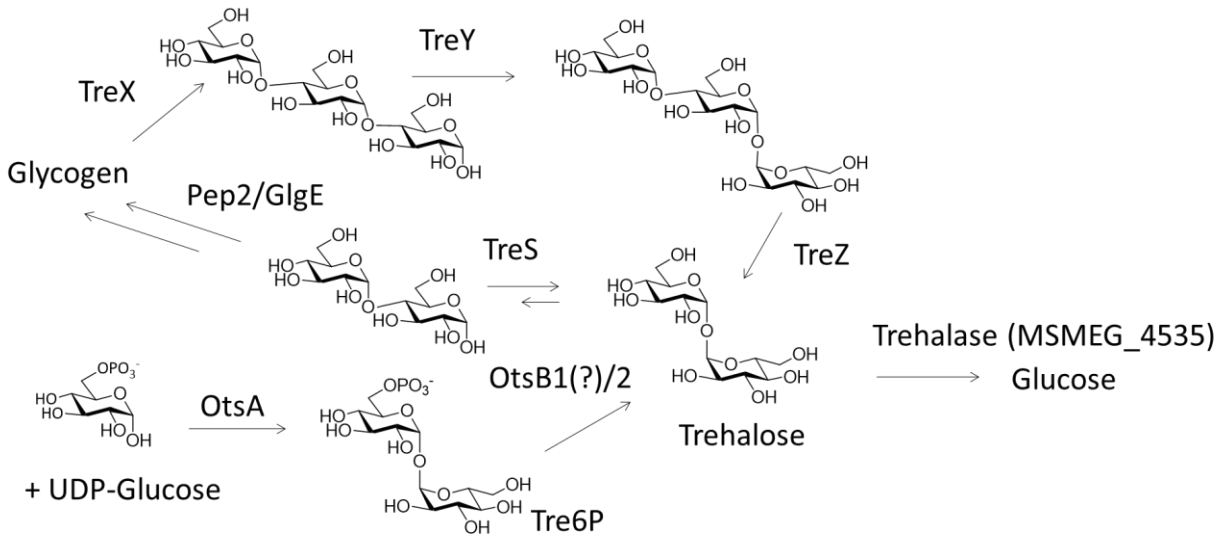



**Figure 1.3. Biosynthetic pathways of trehalose synthesis and utilization in *Mycobacterium spp*.**

Biochemical characterization has been performed for most of the trehalose related enzymes, but the way they function together in livings systems is less well studied. All three pathways have been shown to be fully redundant for purposes of planktonic growth [7] and some intracellular conditions. The *otsA* and *treS* [8] pathways have been shown to be required for full pathogenesis *in vivo* but the mechanisms conferring essentiality are unknown.

The current understanding is that the trehalose pool is large and rapidly turned over, both in the free metabolite and in the Tre-TMM-TDM cycle. The stability of the trehalose pool has been one of its features in studies to date [9]. But the question remains open whether mycobacteria are adapted to ***regulate*** or ***control*** the pool as those terms are understood in metabolic flux analysis. By "regulate" is meant the ability, at a cellular level, to alter, upwards or downwards, the size of a metabolite pool or flux through a pathway. By "control" is meant the ability to maintain the size of a metabolite pool or flux through a pathway in the face of perturbations that would tend to increase or decrease it. For example, the ability of a microbe to accumulate compatible solutes in response to hyperosmotic environments demonstrates the microbe's ability to "regulate" the compatible solutes and their attendant pathways. Alternately, the ability of a microbe to maintain a metabolite pool or flux through a pathway in the face of, for example, nutrient poor medium conditions represents the microbe's ability to "control" the metabolite and related pathways.

It is suspected that the trehalose pool could influence each of the systems it interacts with (cell wall, glycogen, central carbon metabolism) in ways that are crucial during different phases of *Mtb*'s life cycle (transmission, immune encounter, dormancy, reactivation). The influence might be largely passive, for example by establishing a large buffer of trehalose and glucose that can be tapped by each system as needed. Or the influence might be more active, for

example by directing flux into preferred systems based on environmental cues. In either case, a deeper understanding of the loci and methods of regulation and control may open avenues to undermine the fitness of mycobacterial pathogens *in vivo* and, ultimately, during human disease.

In many organisms, osmotic stress is an environmental change that elicits the organism's ability to regulate pools of compatible solutes like trehalose by rapidly accumulating them and equally rapidly disposing of them when the challenge has passed [10]. If mycobacteria regulate the size of their trehalose pool, it is likely they will do so in response to osmotic stress. Therefore, the studies below use osmotic stress to explore if *Mycobacterium spp.* can regulate their trehalose pools and, if so, what is the nature of the response and which of the pathways, if any, are most important to mounting the response.

**Results**

**Free trehalose content in *Mycobacterium smegmatis* (*Msmeg*) and *Mycobacterium tuberculosis* (*Mtb*) is regulated by osmotic stress and controlled by growth phase and medium.** Osmotic stress can be induced by culturing bacteria in several different osmolytes, but the most common method is addition of NaCl to defined culture medium. NaCl at 140 mM (~280 mOsm/L) and above has been shown to induce transcriptional changes as part of *Mtb*'s osmosensory pathways [11,12] without inducing significant cell death.

This study used a 1-hour stress with a supplement of 140 mM NaCl to a variety of media and growth conditions (see Methods). Trehalose content was measured using methods adapted from metabolomics studies [13] to rapidly quench cellular activity to minimize perturbations to dynamic metabolite pools during workup. To quantify trehalose a tandem enzyme assay is used in which porcine trehalose digests free trehalose to 2 molecules of glucose and glucose is quantified by glucose oxidase assay (see Methods for details).

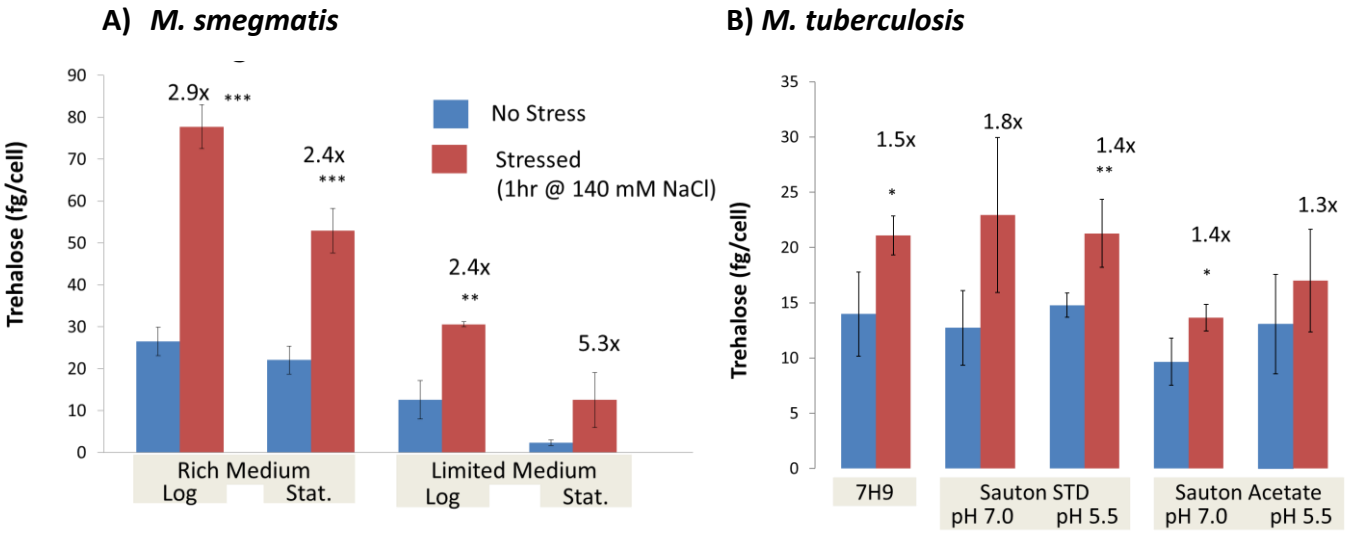


**Figure 1.4. Trehalose content under osmotic stress in *Mycobacterium smegmatis* (*Msmeg*) and *Mycobacterium tuberculosis* (*Mtb*).** Bacteria were grown, stressed with 140 mM NaCl for 1 hour and assayed for trehalose content (n=5). Media conditions are described in Methods. Numbers over bars represent fold change in trehalose content between stressed and unstressed conditions. *Mtb* cultures were all in log phase growth. Asterisks represent p-values comparing stressed and unstressed samples in the same phase, medium or pH conditions (*** $p < 0.001$, ** $p < 0.01$, * $p<0.05$, unpaired, two-tailed Student's t test). The values presented are means ± 1 SD (n=5) and are representative of at least three independent experiments.

Both *Msmeg* (Figure 1.4 A) and *Mtb* (Figure 1.4 B) increase trehalose content in response to osmotic stress. Changes in *Msmeg* are large and statistically significant across most conditions Rich media and log phase growth support larger increases in trehalose in *Msmeg*. The size of the trehalose pool in *Mtb* is lower in rich media relative to *Msmeg*, perhaps reflecting *Mtb*'s lower growth rate and, perhaps, more limited access to nutrients. Acetate is a strictly gluconeogenic medium. *Mtb*'s ability to accumulate trehalose in poor media is not strongly influenced by either pH but is modestly suppressed by reliance on strictly gluconeogenic carbon sources.

The intracellular concentration of trehalose can be inferred from these data. The volume of a *Msmeg* bacterium is around 1 fL. Under osmo-normal conditions, 30 fg/cell would equate to an intrabacterial trehalose concentration of around 167 mM. Under ~280 mOsm/L additional stress from 140 mM NaCl, 75 fg/cell would equate to 420 mM of trehalose. Although it is difficult to estimate the osmotic potential of different solutes in complex mixtures, the addition of ~250 mOsm/L from the additional trehalose would go a considerable length to reducing the osmotic gradient across the membrane and cell wall.

These data demonstrate that *Msmeg* has considerable ability to regulate, but limited ability to control, trehalose under these stress conditions. *Mtb* has a modest ability to both regulate and control trehalose under the tested conditions.

**Kinetics of trehalose accumulation is species dependent.** The speed with which the trehalose response is mounted may suggest something about the nature of the osmotic challenges the bacterium has evolved to anticipate. As a saprophyte, *Msmeg* may be expected to encounter osmotic change as large, unpredictable swings in its physical environment. It is less well known what osmotic stessors *Mtb* encounters during its lifecycle. Tan et al. have demonstrated that the phagosomal environment imposes a chloride stress on *Mtb* corresponding to a 75-90 mM upshift in chloride ion [12]. The osmotic environment of the granuloma, either during formation or dissolution, has not been well defined but might also be expected to impose changes in osmolarity. It has also been hypothesized that confinement in an aerosol droplet during transmission might impose a sharp upshift in osmolarity as water evaporates from a droplet that rapidly loses half its volume [14, 15].

Trehalose was measured a specific timepoints after introduction of stress to determine the kinetics of trehalose responses (Figure 1.5).

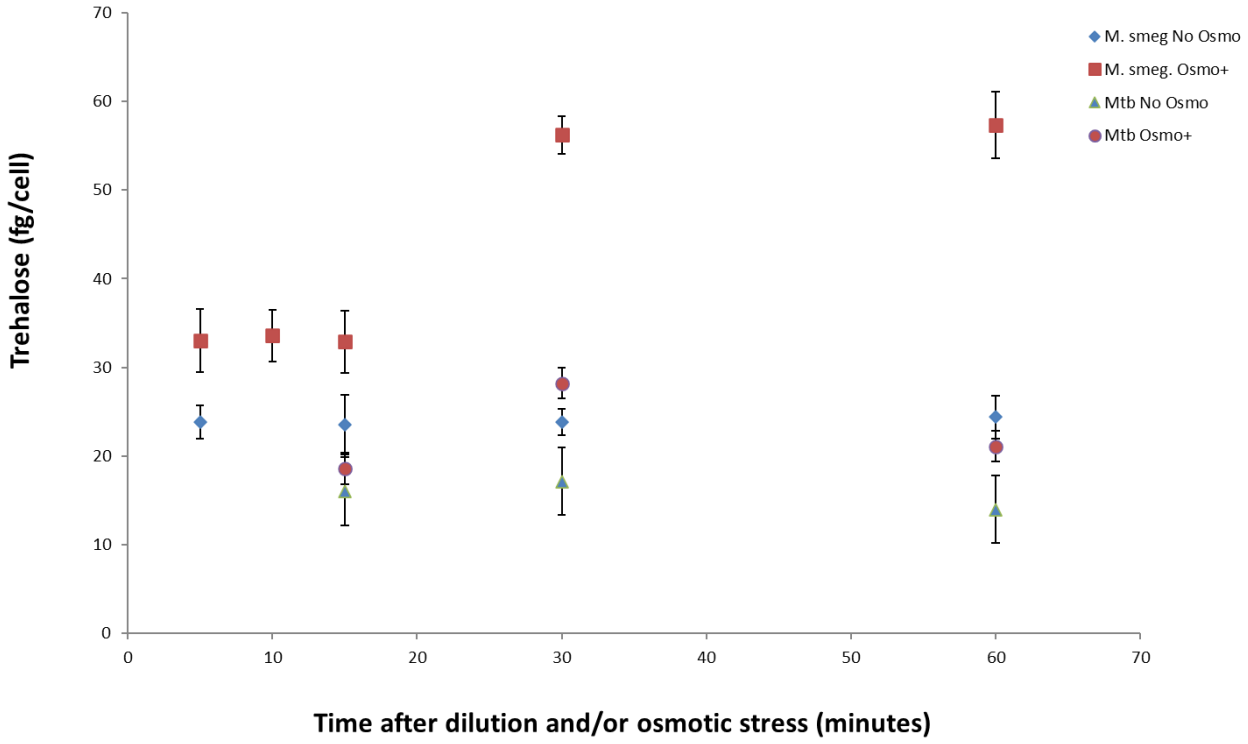


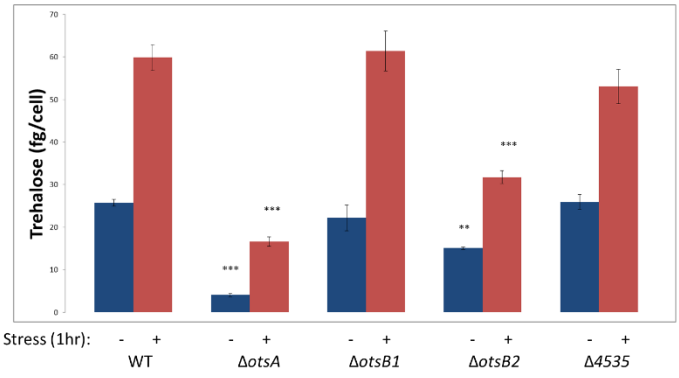

**Figure 1.5. Kinetics of trehalose accumulation in *Mtb* and *Msmeg* under osmotic stress.** Bacteria in log phase growth and rich medium were exposed to 140 mM NaCl stress or dilution only for the indicated periods. Trehalose was extracted by rapid metabolite quenching and quantified. The values presented are means ± 1 SD (n=3) and is representative of at least two separate experiments.

Unstressed *Msmeg* (blue diamonds) and *Mtb* (green triangle) maintained a constant trehalose content, while stressed *Msmeg* (red rectangles) and *Mtb* (red circle) showed little changed in trehalose content until between 15 and 30 minutes after the osmotic stress which were then maintained out to 1 hour. The size of the trehalose pools in this experiment is consistent with Figure 1.4 in which the *Msmeg* trehalose pool is initially larger and more highly upregulated than in *Mtb*.

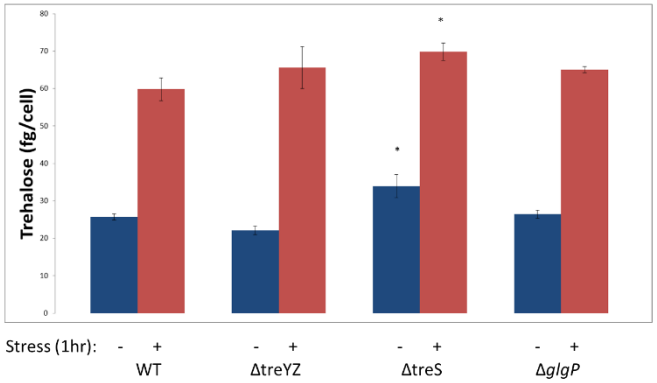
**Trehalose accumulation in Msmeg is pathway dependent.** Trehalose synthesis and degradation is carried out by multiple pathways that provide a great deal of redundancy (Figure 1.3). Although these pathways are fully redundant for normal growth [7] specific pathways might be essential for the trehalose osmosensory response.

*Msmeg* mutants in trehalose synthesis or utilization genes were assessed for their ability to maintain the trehalose pool under normal and stressed conditions and rich or poor medium.

**A) Rich medium, anabolic pathways**




**B) Rich medium, glycogen mobilization pathways**




**C) Nitrogen limited Sauton's**

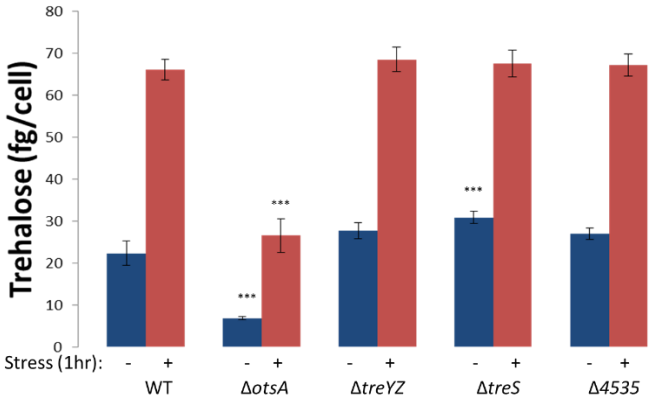



**Figure 1.6. Trehalose accumulation is dependent pathway dependent in *Msmeg*.** Growth medium is (A,B) rich medium or (C) medium favoring glycogen accumulation [16, 17] , with (red) and without (blue) osmotic stress. Bacteria were grown to log phase, stressed with 140 mM NaCl for 1 hour and assayed for trehalose as described in Methods. Δ*4535* lacks the gene for trehalase (trehalose hydrolysis). Asterisks represent p-values comparing trehalose content in the mutant versus wild type under the same conditions (*** $p < 0.001$, ** $p < 0.01$, * $p<0.05$, all by ANOVA with Bonferroni adjustment for multiple comparisons). The values presented are means ± 1 SD of at least three biological replicates.

In both rich and poor medium, loss of the *otsA* pathway results in a much smaller trehalose pool under both stressed and unstress conditions, although the stress response remains robust. This suggests *otsA* is essential for scaling an optimal size trehalose pool but that a sufficient

pool and an osmotic stress response can be mounted by mobilizing glycogen. The putative trehalose-6-phosphatase *otsB1* is irrelevant to the establishment of the trehalose pool and the stress response. *otsB1* has not been characterized and it has been suggested that it's annotation as a trehalose phosphatase is in error [18]. This data is consistent with that possibility.

Loss of the well characterized proven trehalose-6-phosphatase *otsB2* leads to only a small reduction in the unstressed pool and a more considerable reduction of the stressed pool. This is unexpected as there is no known metabolic use for trehalose-6-phosphate (Tre6P) other than phosphate hydrolysis to produce free trehalose and deletion of *otsB2* was expected to be functionally equivalent, from the perspective of trehalose production, as the deletion of *otsA*. It may be that an uncharacterized phosphatase exists that converts Tre6P to Tre that is mobilized in the stress response. Alternately, a Tre processing enzyme might also work on Tre6P and create a substrate that can be mobilized indirectly to Tre under osmotic stress. TreS is one possibility. If TreS coverts Tre6P to maltose-6-phosphate that would provide a pathway to glycogen. The characterization of TreS did not attempt to use Tre6P as a substrate so this possibility has not been directly assessed.

The trehalase mutant (Δ*4535*), like *otsB1*, appears irrelevant in both stressed and unstressed conditions. One might assume that this is expected in rich media conditions in which glucose is already abundant. However in in Sauton's media containing glycerol as the principal carbon source (Figure 1.6C) Δ*4535* remains irrelevant under both conditions. This suggest that mobilization of trehalose towards glycolic flux is not involved in maintaining the trehalose pool or mounting the stress response.

Loss of the glycogen processing gene *treYZ* has no effect suggesting that mobilizing glycogen degradation is not major factor in normal and stressed trehalose pool maintenance. Similarly, loss of *glgP*, which hydrolyses terminal glucoses in glycogen to produce glucose-6-phosphate, has no effect, at least in rich medium. Overall, the data do not indicate a strong role for glycogen degradation in maintaining and regulating the trehalose pool under these conditions.

Interestingly, loss of the bi-directional enzyme TreS leads to small increases in both the unstressed and stressed trehalose pools. TreS interconverts maltose and trehalose in a reaction that is nearly thermodynamically neutral. It has been suggested that mass action may determine the direction of flux through TreS under normal conditions [19]. With the trehalose pool relatively large and the maltose pool relatively small (see Figure 1.8), flux through TreS would be mainly out of the trehalose pool. The data in Figure 1.6 are consistent with that model.

Together these data suggest the critical pathway is the anabolic Tre synthesis pathway through *otsA*. To a lesser extent, limiting outflux from the Tre pool through TreS, but not trehalase, is important for maintaining and regulating the trehalose pool under osmotic stress.

**Growth kinetics are minimally altered under osmotic stress.** The data above looks mostly at short term impact of osmotic stress on the content of the trehalose pool. However osmotic stress might alter the growth kinetics of *Msmeg* in wild-type or mutant strains, implicating those pathways in adaptations to osmotic stress over longer periods of time. Growth curves were monitored by optical density for the wild-type and mutant strain under rich and glycogen-favoring media (Figure 1.7).

In rich medium wild-type *Msmeg* grow to higher density than without stress and the trehalose mutant generally grow to a lower density with the *otsA* mutant most handicapped. The trehalase mutant seems to grow slightly more rapidly without stress but reaches the same density as wild-type. With osmotic stress the wild-type performs similarly to unstressed in log phase but ultimately reaches a lower density than in the unstressed condition. The *otsA* mutant is the most severely affected in both conditions with a lower growth rate in log phase and a lower density in stationary phase.

In limited medium favoring glycogen production, growth rate and stationary phase density are lower than in rich medium as expected. The stress causes growth to slow earlier and slightly limits the extent of growth in stationary phase. Growth kinetics are more uniform across wild-type and the mutants than in rich medium. There are no large differences between wild-type and mutant strains.

Overall, these data suggest that the trehalose response to osmotic stress is adequate to prevent major changes in log phase growth rate or stationary phase culture density. The *otsA* mutant is, perhaps, a bit more attenuated than others suggesting the *otsA* pathway is more important than the other pathways in the longer term growth in both unstressed and stressed conditions.

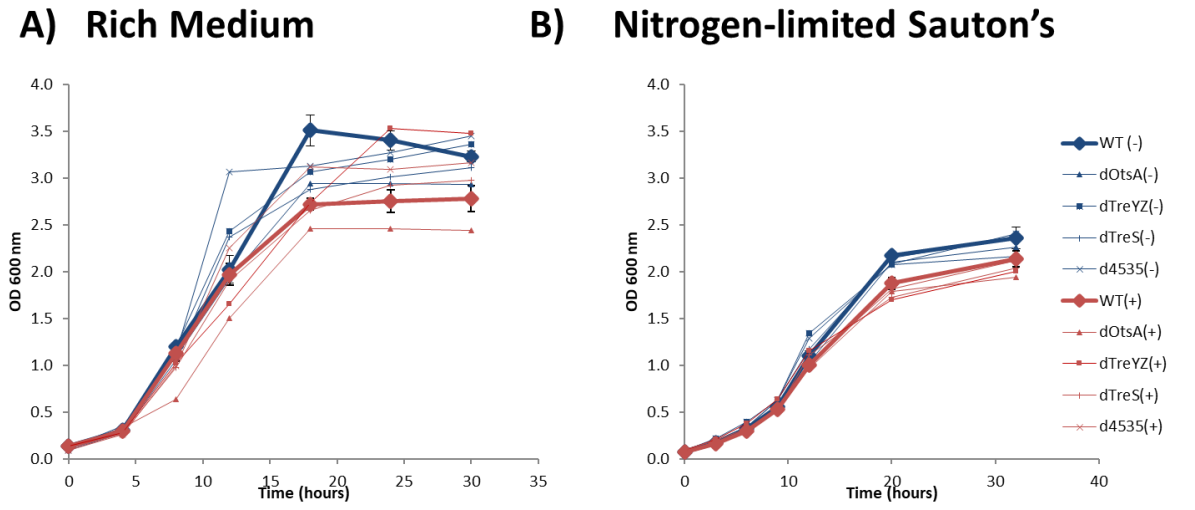


**Figure 1.7. Growth curves of *M. smeg.* wild-type and trehalose mutants.** Growth medium is (A) rich medium or (B) nitrogen-limited Sauton's with (red) and without (blue) osmotic stress. *Δ4535* lacks the gene for trehalase (trehalose hydrolysis). The values presented are means of three technical replicates for representative growth curves. Error bars are ± 1 SD.

**Maltose is low-abundance and does not accumulate in Mtb in response to osmotic stress.** Trehalose is not the only carbohydrate that may accumulate as a compatible solute to equalize osmotic gradients across a membrane. Maltose can also serve as a compatible solute to combat osmotic stress or provide desiccation tolerance. Furthermore, maltose is a known metabolite in mycobacteria and is a single metabolic step removed from the free trehalose pool (Figure 1.3).

*Mtb* in log phase growth were osmotically stressed and metabolites were rapidly quenched and analysed by HPAEC-PAD (see Methods) for maltose content under several medium and pH conditions.

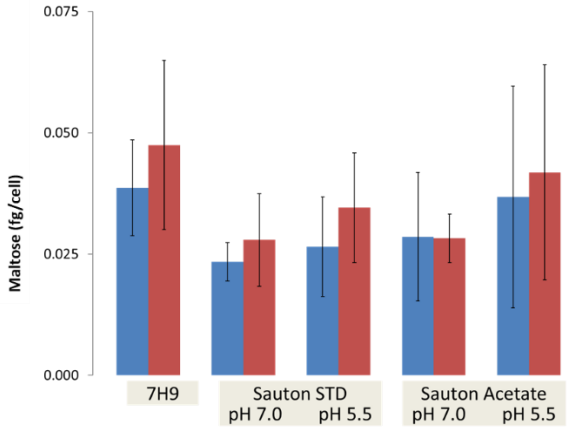



**Figure 1.8. Maltose content in *Mtb* under osmotic stress.** *Mtb* in log-phase growth under the indicated culture conditions was stressed with 140 mM NaCl for 1 hour. Bacteria were rapidly quenched, metabolites were extracted and analyzed by HPAEC-PAD. Data points represent mean +/- s.d. for three technical replicates. Data is representative of two independent experiments.

In *Mtb* maltose is detectable at very low levels under all conditions but is not responsive to osmotic stress. Trehalose levels are approximately 850 times higher under similar conditions (Figure 1.4B). These data suggest that maltose is not accumulated as a compatible solute under osmotic stress. Rather maltose's role is more likely limited to biosynthetic intermediate in the conversion of trehalose to glycogen.

**Other compatible solutes and peptidoglycan are responsive to osmotic stress in *Msmeg*.**

Carbohydrates are not the only compatible solutes that can be accumulated to undermine an osmotic gradient across the cell wall and membrane. Amino acids glutamate, proline, arginine, alanine and serine can also serve as compatible solutes. In general, phenylalanine is not seen as a compatible solute.

*Msmeg* in rich medium was placed under no stress (red) or 140 mM NaCl stress (red) and sampled every thirty minutes up to six hours (Figure 1.9). Early stationary phase was selected to limit the confounding effects of demand for amino acids from growth-related functions. Metabolites were rapidly quenched and extracted and free glutamate, proline, alanine, serine and phenylalanine were analyzed by LC-MS.

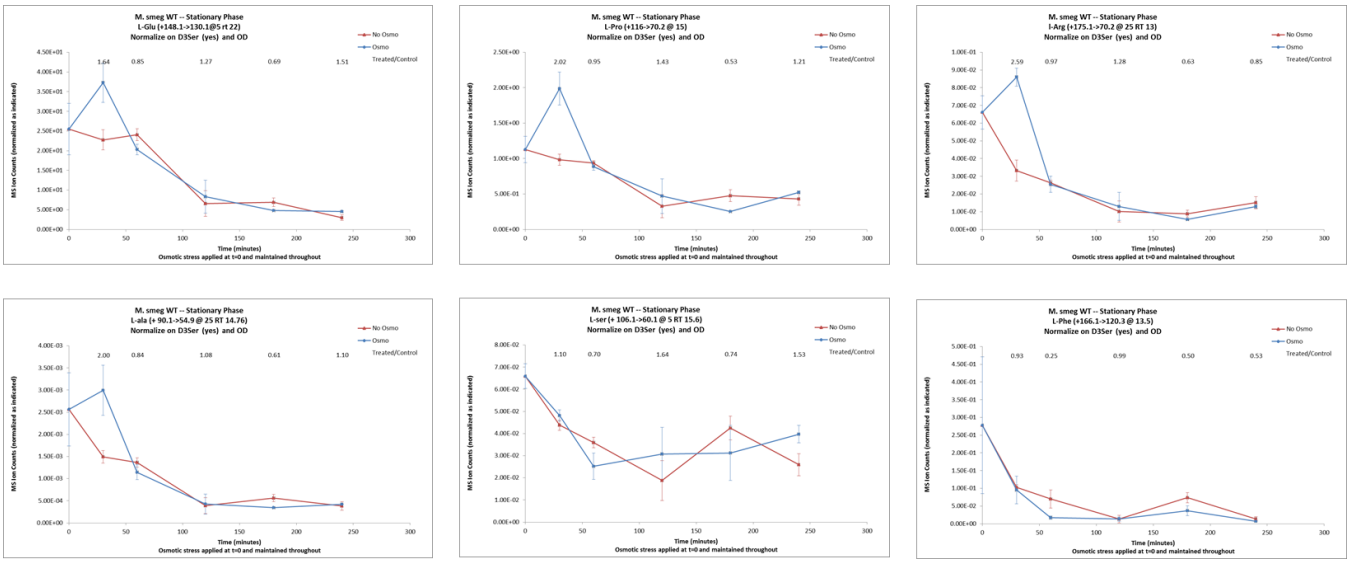



**Figure 1.9. Free amino acids in Msmeg.** Early stationary-phase *Msmeg* subjected to osmotic stress (blue) (140 mM NaCl) or dilution only (red). Soluble metabolites were collected at indicated timepoints by rapid-quenching and analyzed by LC-MS. Time point 0 was before introduction of stress or dilution alone for both conditions. Ion counts for each metabolite of interest were normalized by ion counts for D3-serine standard and OD. Data points represent mean +/- s.d. for three technical replicates. Data is representative of two independent experiments.

All the analyzed amino acids had a generally downward trend over six hours, possibly reflecting a declining demand for free amino acids as growth slows. Serine and phenylalanine showed no difference between stressed and unstressed conditions. Glutamate, proline, arginine and alanine, however, experienced a transient increase in abundance at the 30-minute mark which then disappeared at the 60 minute time point. Thereafter all free amino acids tracked closely between the stressed and unstressed conditions. These data suggest a sub-set of amino acids are accumulated shortly after imposition of osmotic stress but are returned to normal levels as the stress endures.

Over longer periods of time remodeling the cell wall is another potential adaptation to osmotic stress. Strengthening the cell wall may have advantages over maintaining large compatible solute pools for durable adaptation to osmotic stress.

If peptidoglycan remodeling is occurring in *Msmeg* altered abundance might be observed in the peptidoglycan precursors *meso*-DAPA and d-Ala-d-Ala. These metabolites were identified in log and stationary phase *Msmeg* under osmotic stress for at 30 minute intervals up to 6 hours after application of the stress (Figure 1.10).

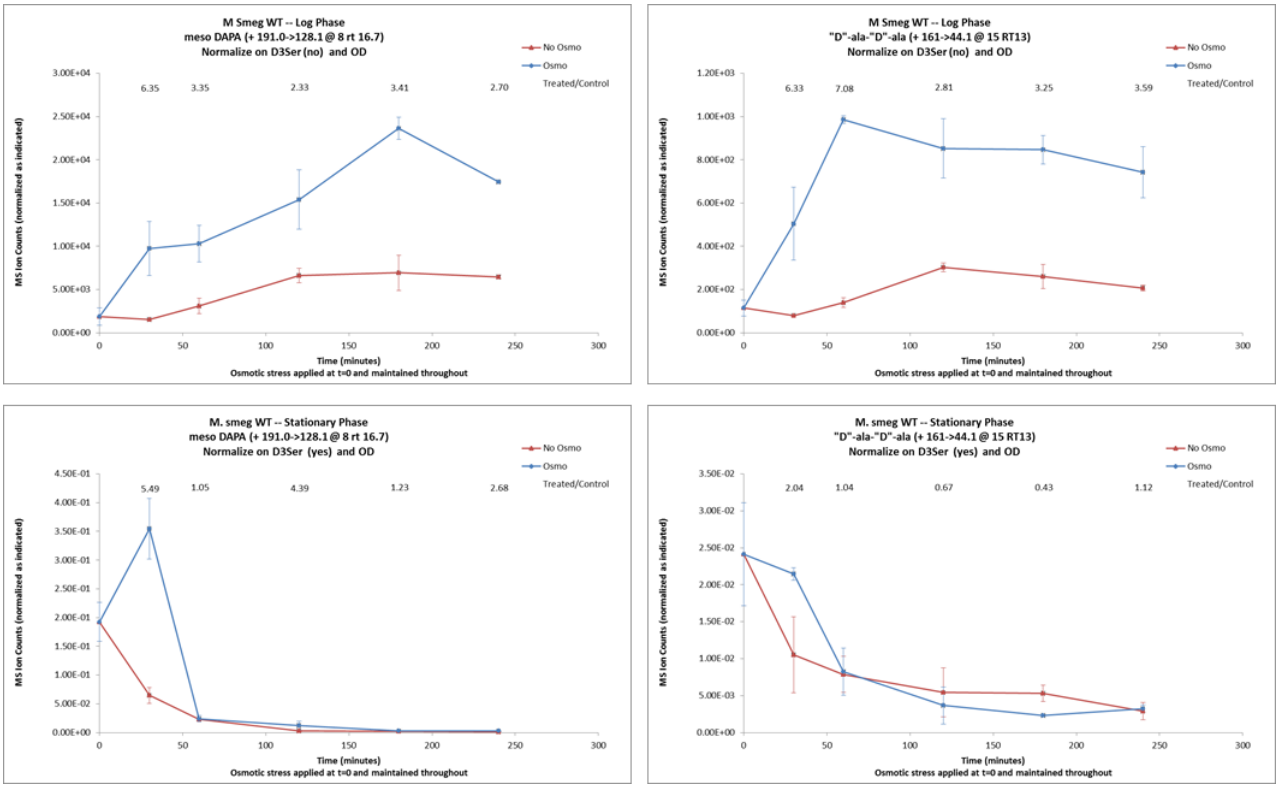



**Figure 1.10. Peptidoglycan precursors in *Msmeg*.** Log- and stationary-phase *Msmeg* subjected to osmotic stress (140 mM NaCl). Soluble metabolites were collected at indicated timepoints by rapid-quenching and analyzed by LC-MS. Ion counts for each metabolite of interest were normalized by ion counts for D3-serine standard and OD. Data points represent mean +/- s.d. for three technical replicates. Data is representative of two independent experiments.

In log phase d-Ala-d-Ala rises dramatically to seven times the level in unstressed bacteria within an hour of the stress and remains high for at least six hours. *meso*-DAPA also rises, though less dramatically, within 30 minutes and is maintained for at least six hours. In early stationary phase the first 30 minutes see a large spike in *meso*-DAPA and a smaller spike in d-Ala-d-Ala which then reverts to levels comparable to the unstress bacteria.

These data suggest a considerable peptidoglycan synthesis and remodeling is on-going in log phase as part of the osmotic stress response. In stationary phase, peptidoglycan remodeling may be less dramatic and limited to the first hour of stress response.

**Discussion**

This study demonstrates that *Mycobacterium smegmatis* and *Mycobacterium tuberculosis* regulate the size of their free trehalose pool (Figure 1.4). For *Msmeg* the base level of trehalose in unstressed conditions is varies modestly across growth phase and medium richness with a significantly smaller pool only seen in poor medium in stationary phase (range: ~30 fg/cell [167 mM] to 2 fg/cell [11 mM]). In response to osmotic stress the pool is increased 2.4 to 2.9 times (to > 400 mM) in the former cases and 5 times (to 55 mM) in the restrictive stationary phase, poor medium case. This suggests *Msmeg* finds it useful to maintain a minimum trehalose level in the face of osmotic stress even in a nutritionally challenging environment.

*Mtb* basal trehalose levels are lower than *Msmeg* in log phase (~12 fg/cell [70 mM]) and relatively constant across medium conditions and pH conditions. The osmotic stress response is present but proportionally smaller than in *Msmeg* (1.4 to 1.8 times increase). This may reflect a more constrained metabolic posture for *Mtb*, the presence of other more effective stress response options than increasing trehalose, or that osmotic stresses of this magnitude are beyond what *Mtb* is adapted to address.

Nevertheless, for both *Msmeg* and *Mtb* the upshift represents a large commitment of resources to the stress response. The trehalose pool is already very large. Compare, for examples, the absolute metabolite concentration in log phase *E. coli* in glucose rich media reported by Bennett [13]. The top metabolites (glutamate and glutathione) are present at much lower leves (96 mM and 17 mM respectively). Increasing an intracellular store of high energy metabolites like trehalose above those levels suggests a major metabolic commitment.

The kinetics of the trehalose response is, surprisingly, quite similar for both *Msmeg* and *Mtb* (Figure 1.5). The increase for *Msmeg* is abrupt at around the 30 minute post stress timepoint with very little increase seen before that. The smaller increase for *Mtb* happens at roughly the same time point. The delayed nature of the response suggests it is not the principal response to immediate osmotics shocks, such as the evaporating droplet on the milliseconds scale [14,15], or slower shocks, like phagosomal engulfment on the minutes scale [20]. Other stress response systems may address those time scales, or the robustness of the mycobacterial cell wall may provide adequate protection making more rapid responses less necessary.

The *otsA*-*otsB2* pathways is strongly implicated as driving the trehalose increase (Figure 1.6). Mutants lacking *otsA* have lower unstressed trehalose levels but also fail to increase trehalose to wild-type levels under stress. If the *otsA*-*otsB* functions to fill up the trehalose pool, the *treS* pathway seem to function mainly to drain the trehalose pool. Mutants lacking *treS* have slightly larger basal and stressed trehalose pools than wild-type.

Growth kinetics overall are not greatly perturbed by either the osmotic stress in this study or the individual gene knockouts although *otsA* mutants grow slightly slower and to a lower peak density (Figure 1.7). While the trehalose pools may vary somewhat across conditions the bacteria compensate, at least with respect to planktonic growth, and even the loss of *otsA* is not catastrophic. This is consistent with data from Woodruff et al. showing the full redundancy of all the trehalose synthesis pathways for normal growth [7].

Other stress responses may be coordinated with the trehalose response. Maltose is present at very low levels in *Mtb* and is not activated as part of the osmotic stress response (Figure 1.8). Rather the role of maltose seems to be simply as a metabolic intermediate on the pathway that transforms trehalose into glycogen. Conversely, in *Msmeg* amino acids that could act as compatible solutes (glutamate, proline, arginine, alanine) are transiently increased at 30 minutes post stress, sometimes quite dramatically before returning to normal at 60 minutes post stress. This may function to increase compatible solutes, to support synthesis of new proteins to support the stress response or may reflect an increased rate of protein degradation. The fact that serine and phenylalanine are not similarly pulsed suggests the response may be more specific. Similarly, the peptidoglycan precursors *meso*-DAPA and d-Ala-d-Ala also increase significantly and sustained at a higher level in log phase growth while falling back to normal in stationary phase.

How is the regulation trehalose and other stress responses accomplished? The literature has two studies of transcriptional responses to NaCl stress. The conditions used by Hatzios et al. [11] are most comparable to these studies (1 hour, 150 mM NaCl stress of *Mtb* in Sauton's medium). Tan et al. [12] looked at *Mtb* in rich medium stressed by 250 mM NaCl for 4 hours. Interestingly, neither identify differentially regulated genes (either up or down) in pathways immediately involved in trehalose synthesis or utilization (Figure 1.3). Transcriptional regulation, if it occurs, must be happening farther afield. Interestingly, Hatzios (but not Tan) identifies *pckA*, which controls the rate limiting step in gluconeogenesis, as strongly up-regulated under osmotic stress. However, TAG synthesis (t*gs1*) is upregulated and TAG hydrolysis (*lipC* esterase) is downregulated so the trehalose pool may compete with lipid droplet formation for enhanced gluconeogenic flux. No other central carbon metabolism or glycogen related genes are implicated.

Hatzios (but not Tan) also sees an increase in arginine biosynthesis genes, consistent with amino acid level results (Figure 1.9). No other amino acids or peptidoglycan precursors are implicated transcriptionally.

Both Hatzios and Tan identify strong increases in expression of several components of the ESX-1 secretion system (*espA*, *espC* and *espD*). This implies that *Mtb* may associate increased osmotic stress with an event like phagosomal engulfment that calls for an uptick of the host modulating activities facilitated by ESX-1.

If trehalose related genes are not directly regulated transcriptionally to produce the increase, it is possible they may be regulated post-translationally through protein phosphorylation or

protein degradation. Unfortunately, phosphoproteomics studies have not been performed under osmotic stress conditions and little is known about the direct regulation of trehalose synthesis enzymes by phosphorylation. This would be a useful area for future research and the osmotic stress model might prove useful in revealing regulation at this level.

## Materials and Methods

***Bacterial strains and culture conditions.*** The wild-type bacterial strains were *M. smegmatis* $mc^2155$, *M. tuberculosis* H37Rv. All handling of *Mtb* occurred in a certified BSL3 facility under protocols approved in advance by UC Berkeley's Environment Health and Safety (EH&S) office. Materials removed from the BSL3 for further analysis were neutralized according to procedures approved in advance by UC Berkeley's EH&S office. *Msmeg* mutant strains (*ΔotsA, ΔotsB1, ΔotsB1, ΔtreS, ΔtreYZ, Δ4535, ΔglgP*) were provided by Dr. Rainer Kalscheuer (Institute for Medical Microbiology and Hospital Hygiene, Heinrich-Heine-University Duesseldorf, Germany). All cultures were grown as liquid broths at 37 ˚C shaken at 220 rpm (*Msmeg*) or in roller bottles (*Mtb*). Growth phase was determined by $OD_{600nm}$.

Rich medium refers to 7H9/Glycerol (0.5 %w/v)/Tween 80 (0.05 %v/v) supplemented with ADC (10 %) for *Msmeg* and OADC (10 %) for *Mtb*. Sauton's medium is (per 1L): 0.5 g $KH_2PO_3$, 0.5 g $MgSO_4$, 4 g L-asparagine monohydrate, 2 g citric acid, 0.05 g ferric ammonium citrate, 60 mL glycerol, 0.1 mL 1 %w/v $ZnSO_4$, 2.5 mL 20 %v/v Tween 80, pH 7. Nitrogen-limited Sauton's refers to Sauton's medium modified to contain no asparagine, ferric citrate instead of ferric ammonium citrate, ammonium sulfate (10 mM) as the sole nitrogen source and only 0.2 % glycerol. This formulation is known to increase production of glycogen [7]. Sauton's Acetate is Sauton's medium modified with 10 mM sodium acetate replacing glycerol as the principal carbon source and induces predominantly gluconeogenic carbon flow.

**Rapid metabolite quenching.** Rapid metabolite quenching was adapted from methods adapted used in metabolomics studies [13] to rapidly quench cellular activity to minimize perturbations to dynamic metabolite pools. Cultures are filtered onto PES filter membranes under slight suction and quickly washed multiple times with equal volumes of PBS to remove extracellular metabolites. Filters were quenched in a petri dish containing an acetonitrile/methanol/water (40:40:20 by volume) solution cooled to -20 °C which halts all metabolism. Internal standards, if needed, may be spiked into the dish at this point. The steps from culture flask to metabolic quenching can be accomplished in 2-3 minutes thus minimizing metabolic changes during workup.

Bacteria were scraped off the membrane into an o-ring tube with 0.1-mm silica beads and cells are lysed by beat beating (4 cycles of 30 seconds with 1 minute rest periods on ice to prevent heating the solution). Supernatant was removed and frozen at −80 °C until analyzed. Aliquots were thawed, if necessary, and dried on a Labconco CentriVap at 40 °C and resuspended in medium suitable to the subsequent analytical workups.

Rapid metabolite quenching is performed in trehalose content assays, HPAEC-PAD analysis of trehalose and maltose and in LC-MS analysis of amino acids and peptidoglycan precursors.

***Trehalose content assay.*** Cultures were grown to the desired phase as determined by OD and split into 2 equal aliquots. Both aliquots were diluted by 10% with the same medium which included additional NaCl for osmotically stressed cultures to produce a final concentration of 140 mM additional salt (~280 mOsm/L) and grown for 1 hour. "Unstressed" samples do not experience osmotic stress but do undergo a 10 % dilution at the initial timepoint. Stressed samples experience both osmotic stress and 10 % dilution at $t_0$.

Rapid metabolite quenching is performed on samples. For *Mtb* samples, organic extracts are double filtered through 0.2 µM filter syringes before removal from the BSL3. Dried extracts are resuspended in citric acid buffer (135 mM, pH 5.7 @ 37 ˚C ) and digested for at least 15 hours with porcine trehalase (Sigma Aldrich). Trehalose content was determined by quantifying glucose released by the trehalase digest using a glucose oxidase assay (Sigma Aldrich). Trehalose was determined from a glucose standard curve after correcting for background glucose levels with a no-trehalase control. Each sample is analyzed in technical triplicates for both trehalose+ and trehalase- controls.

The trehalase/glucose-oxidase method was cross-validated by comparison with a low throughput trehalose quantification method based on Dionex high performance anion exchange chromatorgraphy with pulsed amperometric detection (HPAEC-PAD). Dionex HPAEC-PAD is designed specifically to chromatographically resolve and quantify carbohydrates. The method is capable of easily separating and quantifying similar carbohydrates such as trehalose and maltose (Supplemental Figure S.1.1).

**Extraction of Free Sugars for HPAEC-PAD.** Metabolite extracts were thawed and spiked with xylitol to a final concentration of 20 µM for use as an internal standard. Aliquots (300 µL) were dried on a Labconco CentriVap at 40 °C, resuspended in an equal volume of 18Ω water, and analyzed by high-performance anion exchange chromatography with pulsed amperometric detection (HPAEC-PAD).

**Analysis of Free Sugars by HPAEC-PAD.** The trehalose and maltose content of cytosolic extracts was determined by HPAEC-PAD performed on a Dionex ICS-5000 with a CarboPac MA-1 analytical column (4 mm × 250 mm) and MA-1 guard column (4 mm × 50 mm) maintained at 30 °C. The method was performed with eluents 18Ω water (E1) and 18Ω water and 1 M NaOH (E2) as follows: T0 min = 48% E2; T28 = 48% E2; T32 = 60% E2; T80 = 60% E2; and T85 = 48% E2. The flow rate was 0.4 mL/min. Pulsed amperometry with the Gold Standard PAD waveform was used for detection. The system autosampler was maintained at 10 °C and configured to inject 25 µL per sample. Chromeleon 7 software (Dionex) was used for generating chromatograms, peak area integration, and for data analysis. Disaccharide standards and xylitol were purchase from Sigma-Aldrich. Retention time for each analyte was determined by performing the HPAEC-PAD method on pure standards (100 µM each). Signal stability was confirmed by introducing an

internal standard (xylitol, 100 µM) into each experimental sample. Analyte concentration per cell was determined by reference to an external standard for each analyte.

**LC-MS quantification of metabolites.** Lysates for metabolic profiling were prepared as described above in rapid metabolic quenching except extracts were not dried by CentriVap. Instead D3-Serine (1 nmol) was added to each sample as an external standard. Samples were vigorously vortexed and sonicated, and insoluble material was removed by centrifugation. An aliquot of the supernatant (20 µL) was analyzed by selected reaction monitoring–based LC-MS-MS. Polar metabolite separation was achieved with a Luna normal-phase $NH_2$ column (50 x 4.6 mm, with 5-µm–diameter particles; Phenomenex, Torrance, CA). Mobile phase A was composed of 100% acetonitrile, and mobile phase B consisted of water and acetonitrile in a 95:5 ratio. Solvent modifier 0.2% ammonium hydroxide with 50 mM ammonium acetate was used to assist ion formation and to improve the LC resolution in negative ionization mode. The gradient started at 0% B and increased linearly to 100% B over the course of 30 min with a flow rate of 0.7 mL/min. Mass spectrometry analysis was performed with an electrospray ionization source on an Agilent 6430 QQQ liquid chromatography– tandem mass spectrometry (Agilent Technologies, Santa Clara, CA). The capillary voltage was set to 3.0 kV, and the fragmentor voltage was set to 100 V. The drying gas temperature was 350 ˚C, the drying gas flow rate was 10 L/min, and the nebulizer pressure was 35 ψ. Representative metabolites were quantified by selected reaction monitoring of the transition from precursor to product ions at associated optimized collision energies. Transitions for selected reaction monitored were developed by analysis of pure standards

**Acknowledgements.** We are grateful to Dr. Rainer Kalscheuer (Institute for Medical Microbiology and Hospital Hygiene, Heinrich-Heine-University Duesseldorf, Germany) for providing the *M. smeg.* mutants and Dr. Daniel Nomura at UC Berkeley provided access to LC-MS equipment. This research was supported by funding from the National Institutes of Health (NIH Grant No. AI51622).

**Supplemental Information**

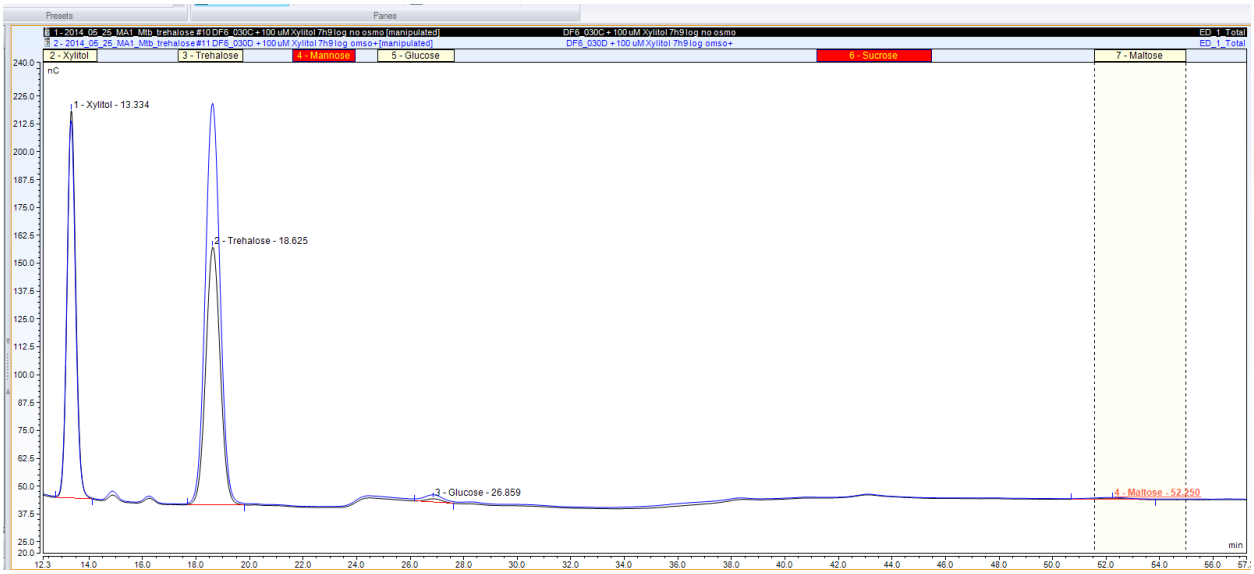



**Figure S.1.1 Dionex chromatogram for separation and quantification of xylitol, trehalose, glucose and maltose (see also Methods).**

## References

1. Elbein, A. D., Pan, Y. T., Pastuszak, I., & Carroll, D. (2003). New insights on trehalose: a multifunctional molecule. *Glycobiology*, *13*(4), 17R-27R. https://doi.org/10.1093/glycob/cwg047

2. Sambou, T.,Dinadayala, P., Stadthagen, G., Barilone, N., Bordat, Y., Constant, P., Levillain, F., Neyrolles, O., Gicquel, B., Lemassu, A., Daffé, M., & Jackson, M. (2008). Capsular glucan and intracellular glycogen of Mycobacterium tuberculosis: biosynthesis and impact on the persistence in mice. *Molecular Microbiology*, *70*(3), 762–774. https://doi.org/10.1111/j.1365-2958.2008.06445.

3. De Smet, K. A. L., Weston, A., Brown, I. N., Young, D. B., & Robertson, B. D. (2000). Three pathways for trehalose biosynthesis in mycobacteria. *Microbiology-Uk*, *146*, 199–208.

4. Kalscheuer, R., Weinrick, B., Veeraraghavan, U., Besra, G. S., & Jacobs, W. R. (2010). Trehalose-recycling ABC transporter LpqY-SugA-SugB-SugC is essential for virulence of Mycobacterium tuberculosis. *Proceedings of the National Academy of Sciences*, *107*(50), 21761–21766. https://doi.org/10.1073/pnas.1014642108

5. Elbein, A. D. (2010). Chapter 11 - Cytoplasmic carbohydrate molecules: Trehalose and glycogen. In H. Otto, J. B. Patrick, & I. Mark von (Eds.), *Microbial Glycobiology* (pp. 185–201). Academic Press.

6. Elbein, A. D., Pastuszak, I., Tackett, A. J., Wilson, T., & Pan, Y. T. (2010). Last Step in the Conversion of Trehalose to Glycogen. *Journal of Biological Chemistry*, *285*(13), 9803–9812. https://doi.org/10.1074/jbc.M109.033944

7. Woodruff, P. J., Carlson, B. L., Siridechadilok, B., Pratt, M. R., Senaratne, R. H., Mougous, J. D., Riley, L. W., Williams, S. J., & Bertozzi, C. R. (2004). Trehalose Is Required for Growth of Mycobacterium smegmatis. *Journal of Biological Chemistry*, *279*(28), 28835–28843. https://doi.org/10.1074/jbc.M313103200

8. Murphy, H. N., Stewart, G. R., Mischenko, V. V, Apt, A. S., Harris, R., McAlister, M. S. B., Driscoll, P. C., Young, D. B., & Robertson, B. D. (2005). The OtsAB Pathway Is Essential for Trehalose Biosynthesis in Mycobacterium tuberculosis. *Journal of Biological Chemistry*, *280*(15), 14524–14529. https://doi.org/10.1074/jbc.M414232200

9. Elbein, A. D. (1974). The metabolism of α, α-trehalose. *Advances in Carbohydrate Chemistry and Biochemistry*, *30*, 227–256.

10. Csonka, L. N. (1989). Physiological and genetic responses of bacteria to osmotic stress. *Microbiological Reviews*, *53*(1), 121–147. http://mmbr.asm.org/content/53/1/121.abstract

11. Hatzios, S. K., Baer, C. E., Rustad, T. R., Siegrist, M. S., Pang, J. M., Ortega, C., Alber, T., Grundner, C., Sherman, D. R., & Bertozzi, C. R. (2013). Osmosensory signaling in Mycobacterium tuberculosis mediated by a eukaryotic-like Ser/Thr protein kinase. *Proc Natl Acad Sci U S A*, *110*(52), E5069-77. https://doi.org/10.1073/pnas.1321205110

12. Tan, S., Sukumar, N., Abramovitch, R. B., Parish, T., & Russell, D. G. (2013). Mycobacterium tuberculosis Responds to Chloride and pH as Synergistic Cues to the Immune Status of its Host Cell. *PLoS Pathog*, *9*(4), e1003282. https://doi.org/10.1371/journal.ppat.1003282

13. Bennett, B. D., Yuan, J., Kimball, E. H., & Rabinowitz, J. D. (2008). Absolute quantitation of intracellular metabolite concentrations by an isotope ratio-based approach. *Nat. Protocols*, *3*(8), 1299–1311. http://dx.doi.org/10.1038/nprot.2008.107

14. Nicas, M., Nazaroff, W. W., & Hubbard, A. (2005). Toward Understanding the Risk of Secondary Airborne Infection: Emission of Respirable Pathogens. *Journal of Occupational and Environmental Hygiene*, *2*(3), 143–154. https://doi.org/10.1080/15459620590918466

15. Vejerano, E. P., & Marr, L. C. (2018). Physico-chemical characteristics of evaporating respiratory fluid droplets. *Journal of the Royal Society, Interface*, *15*(139), 20170939. https://doi.org/10.1098/rsif.2017.0939

16. Behrends, V. D., Williams, K., Jenkins, V., Robertson, B., & Bundy, J. G. (2012). Free glucosylglycerate is a marker of nitrogen stress in Mycobacterium smegmatis. *Journal of Proteome Research*. https://doi.org/10.1021/pr300371b

17. Elbein, A. D., & Mitchell, M. (1973). Levels of Glycogen and Trehalose in Mycobacterium smegmatis and the Purification and Properties of the Glycogen Synthetase. *J. Bacteriol.*, *113*(2), 863–873. http://jb.asm.org/cgi/content/abstract/113/2/863

18. Kalscheuer, R., & Koliwer-Brandl, H. (2014). Genetics of Mycobacterial Trehalose Metabolism. *Microbiol Spectr*, *2*(3).

19. Pan, Y.-T., Carroll, J. D., Asano, N., Pastuszak, I., Edavana, V. K., & Elbein, A. D. (2008). Trehalose synthase converts glycogen to trehalose. *FEBS Journal*, *275*(13), 3408–3420. https://doi.org/10.1111/j.1742-4658.2008.06491.x

20. Russell, D. G., Purdy, G. E., Owens, R. M., Rohde, K. H., & Yates, R. M. (2005). Mycobacterium tuberculosis and the four-minute phagosome. *ASM NEWS-AMERICAN SOCIETY FOR MICROBIOLOGY*, *71*(10), 459.

## Chapter 2: Cationic amphiphilic drugs (CADs) restrict *Mycobacterium tuberculosis* in infected macrophages.

### Introduction

*Mycobacterium tuberculosis*, the causative agent of tuberculosis (TB), and HIV, are the two infectious diseases which cause the most deaths annually [1]. As many as two billion people are estimated to be latently infected with *M. tuberculosis* [2]. Despite the existence of effective antibiotics treatment of TB is challenging due to the long duration of chemotherapy needed to sterilize infection [3] and the emergence and spread of drug resistance [4]. The standard regimen for uncomplicated, drug susceptible cases was shortened from 9-12 months to the current 6-month short course with the addition of pyrazinamide (PZA) [3, 5]. Because PZA is inactive *in vitro* at neutral pH most screens would not have been identified its efficacy. It is only because PZA was administered in a murine model of TB that its potent *in vivo* activity was discovered [5].

This demonstrates the need for more robust systems for screening potential novel antimicrobial drugs in relevant pharmacokinetic environments. Screening compounds against *M. tuberculosis* in its natural niche, the macrophage phagosome, rather than planktonic culture represents progress to that end, and this study takes as its starting point a hit from just such an intramacrophage screen [6]. Specifically, the antidepressant drug fluoxetine (FLX) was found to restrict *M. tuberculosis* growth inside macrophages at concentrations much lower than those required for direct antibacterial effect against bacteria in culture medium. While this effect was originally thought to indicate a host-mediated effect, several experimental approaches suggested that direct action of the compound occurred due to accumulation inside the acidic compartment of exposed cells.

Weakly basic compounds of moderate lipophilicity have been shown to accumulate in acidic organelles by a mechanism proposed in 1974 by de Duve called ion trapping [7–10] (Figure 2.1). Compounds in this class are frequently referred to as cationic amphiphilic drugs (CADs) and are characterized by pKa values which are basic relative to the acidic compartment (generally 7 to 11) and LogP values between 3 to 7, indicating modest lipophilicity (Figure 2.2 shaded region). de Duve's model predicts that deprotonated compounds passively diffuse across membranes due to their lipophilicity but become trapped when protonated in the acidic compartment. Compounds are predicted to accumulate relative to their extracellular concentration proportional to the difference between the pKa of the molecule and the pH of the compartment. For example, a compound with pKa of 9 would accumulate in a pH 6 compartment to 3 log units or 1000x higher than the concentration found in the culture medium. This approximation does not account for the potentially significant influence of transporters (both influx and efflux), detoxifying enzymes or compound binding proteins. Nevertheless, if accumulation on this scale does occur, compounds might reach intra lysosomal concentrations high enough to exceed their admittedly unimpressive extracellular $EC_{50}$s and thus become effective in an acidic niche.

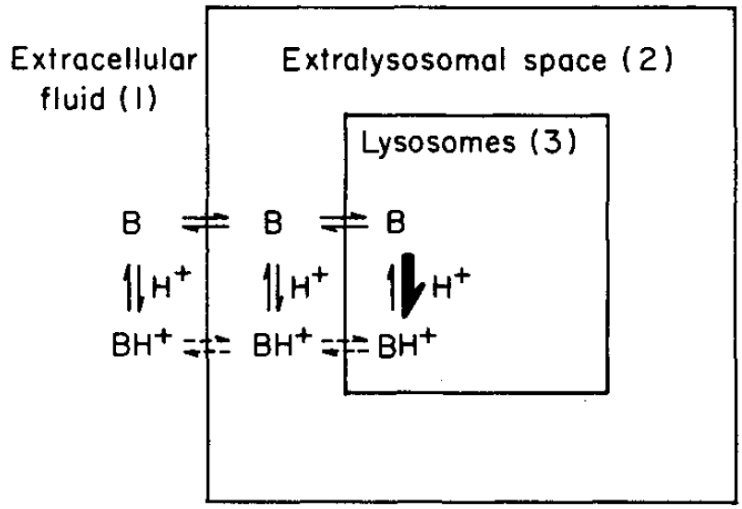



**Figure 2.1. de Duve's model of lysosomal accumulating by ion trapping** [reproduced from 9]**.**

*M. tuberculosis* is known to reside in a relatively acidic compartment [11, 12]. Some, but by no means all, current and emerging antitubercular drugs are CADs and acidic compartment accumulation might in part explain their efficacy (Figure 2.2).

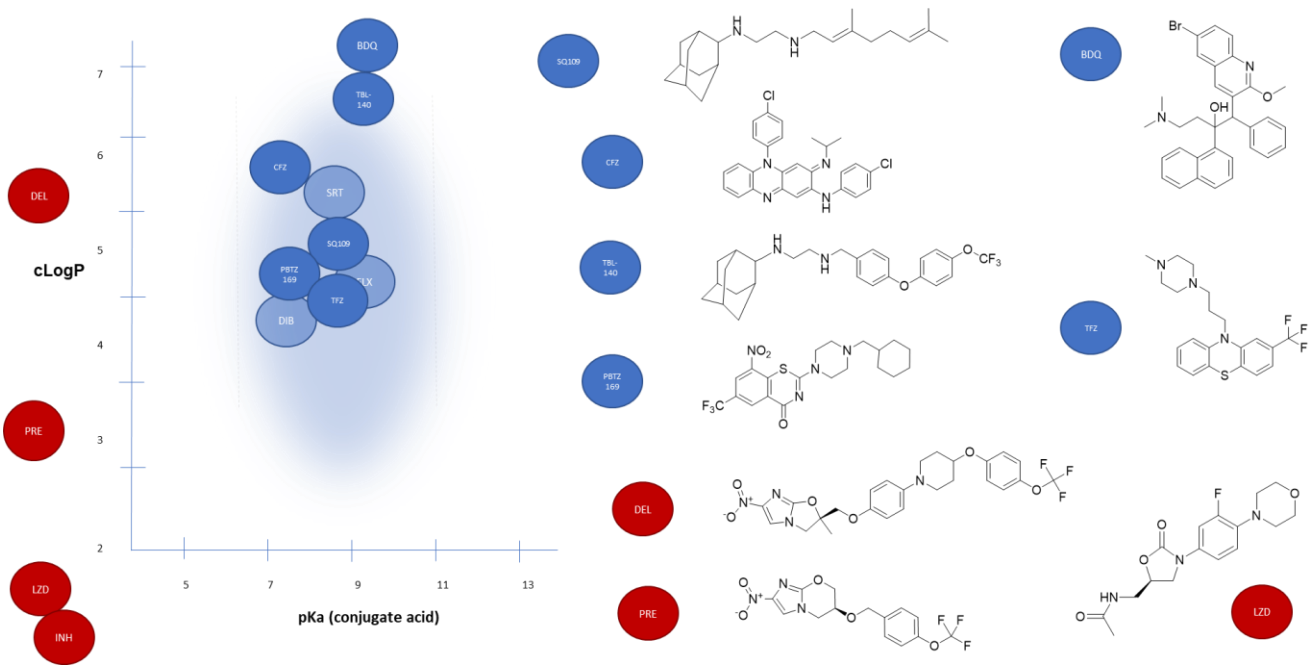



**Figure 2.2. Many TB pipeline drugs are CADs.** cLogP (octanol-water partition coefficient) and pKa are calculated from chemical structures (ChemAxon). Compounds in the shaded zone are

predicted to result in lysosomal accumulation. Red = predicted non-accumulator. Blue = predicted accumulator. Abbreviations: DEL = delamanid, PRE = pretomanide, LZD = linezolid, INH = isoniazid, BDQ = bedaquiline, CFZ = clofazimine, SRT = sertraline, FLX = fluoxetine, DIB = dibucaine, SRT = sertraline, FLX = fluoxetine, DIB = dibucaine.

The studies presented here investigated whether de Dube's ion trapping mechanism explains the increased activity of FLX and other chemically similar compounds when applied to *Mtb* infected macrophages relative to their activity against bacteria in broth culture. To make conditions as comparable as possible, the pH of the planktonic culture media was adjusted to match the approximate value encountered by *M. tuberculosis* inside phagosomes, i.e., pH 6.4 [13, 14].

Based on their pKa and cLogP values, several drugs in addition to FLX were examined (Supplemental Figure S.2.1). As a consequence of lysosomal accumulation CADs are known to induce phospholipidosis (PLD) at extracellular concentrations in the micromolar range. PLD may contribute to CADs' mechanism of action, or it may serve as a fortuitous biomarker for the compounds are effective against intracellular *Mtb*. Consequently, this study looks are whether antitubercular CADs also induce PLD during *Mtb* infection. Lastly, the tropism of CADs might make them useful scaffolds for tethering other hydrophilic antitubercular compounds to increase their effective concentration in *Mtb* infected phagosomes. This study further characterizes a pair of chemically manipulable CADs that might be developed as a carrier for isoniazid or other hydrazide bearing drugs.

**Results**

***M. tuberculosis* growth is restricted inside macrophages by CAD compounds.** Sertraline, fluoxetine and dibucaine, three compounds with predicted accumulation in acidic organelles, restricted the growth of a bioluminescent *M. tuberculosis* after 72 h of treatment in resting primary murine macrophages in a dose-dependent manner (Figure 2.3A). The level of restriction observed with fluoxetine was comparable to the original description of its activity in this context by Stanley et al. [6]. CFU enumeration tracked with the results of the luminescent assay (Figure 2.1B). All compounds demonstrated a dose-response gradient.

To rule out the possibility that the observed effect was a product of cell death, the CellTox green assay was used. CellTox green is excluded from living cells but is highly fluorescent when bound to the DNA of dead or dying cells. No significant cell death was observed relative to solvent control under drug treatment conditions, while cells exposed to the detergent Triton X-100 had a strong fluorescent signal, indicative of loss of plasma membrane integrity (Figure 2.3D).

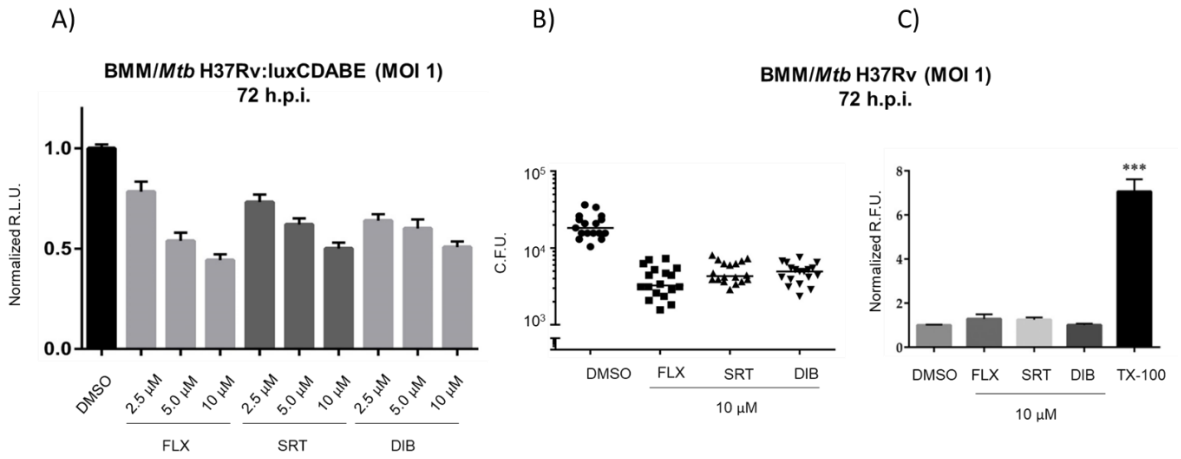



**Figure 2.3. CAD compounds restrict intracellular *Mtb*.** Intramacrophage growth restriction of an *Mtb* luciferase reporter strain by (A) luminescence (n = 3; ±SEM) or (B) CFU enumeration (n = 2;). All treatments show reduced relative luminescent units (RLU) or CFU compared to the DMSO control ($p < 0.05$ by analysis of variance with Bonferroni's adjustment for multiple comparisons). Effect is dose dependent for all compounds. (C) Study compounds do not induce cell death by CellTox Green assay (n = 2 to 4; all comparisons versus the DMSO control were nonsignificant except for the Triton X-100 positive control for membrane integrity loss, which had a p value of <0.001 [***]). All conditions in each experiment were tested as triplicate biological replicates; CFU experiments were plated in triplicate from triplicate biological replicates.

**Neutralization of acidic compartments reduces the growth-inhibitory effect of CADs.** To determine whether neutralization of the pH gradient would reduce or eliminate accumulation of CAD drugs, ammonium chloride was used to directly neutralize acidic compartments of infected, resting macrophages just after infection [17]. Alternately, bafilomycin A1 was used to achieve the same effect indirectly through inhibition of the vacuolar $H^+$ ATPase [18]. Concentrations were titrated such that the neutralization treatments alone did not affect bacterial load as measured by luminescence assay. Statistically significant reductions in the restriction of mycobacterial growth were observed with CAD compounds when they were applied with ammonium chloride (20 mM) or bafilomycin A1 (5 nM). Clinically important antimicrobial drug (isoniazid [INH]), which has a chemical profile not consistent with pH-based partitioning, was not affected by neutralization (Figure 2.4).

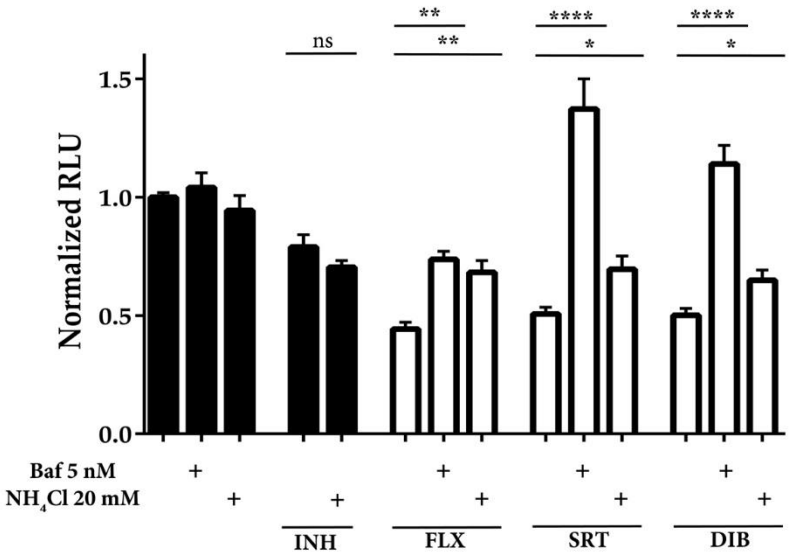



**Figure 2.4. CAD restriction is pH dependent.** Acidic compartments were neutralized directly with ammonium chloride or bafilomycin A1 treatment. Growth restriction by compounds SRT, FLX and DIB (10 µM) is partly abrogated by neutralization. Growth restriction by low-dose isoniazid (INH, 0.15 µM) is not dependent on neutralization. (* = $p < 0.05$; ** = $p < 0.005$; **** = $p < 0.0001$; all by ANOVA with Bonferroni adjustment for multiple comparisons; ns, not significant by unpaired, two-tailed Student's t test).

**Non-protonatable analogs of CAD compounds are inactive against intramacrophage bacteria.** To investigate if the secondary amines in FLX and SRT are the basic functional group governing the growth restriction observed, close analogs lacking that group were tested. Specifically, tests were performed on an analog of FLX which has a quaternary amine (qFLX) and an analog of sertraline which has a ketone in place of the secondary amine (kSRT) (Figure 2.5). The permanent quaternary amine in qFLX is positively charged at physiologic pH and kSRT lacks a protonatable amine altogether; neither would be capable of performing the accumulation describe by DeDuve's model.

These compounds showed weak extracellular activity (qFLX $EC_{50}$ 355 µM, kSRT $EC_{50}$ 305 µM) and similarly weak activity in infected primary murine bone marrow-derived macrophages (Figure 2.5 and Supplementary Table 2.1) even at the maximum dose tolerated by BMM (40 µM). These results suggest that a protonatable amine is key to intracellular efficacy. However, the possibility cannot be definitively ruled out that the amine itself, rather that it's acid-base function, is the relevant pharmacophore.

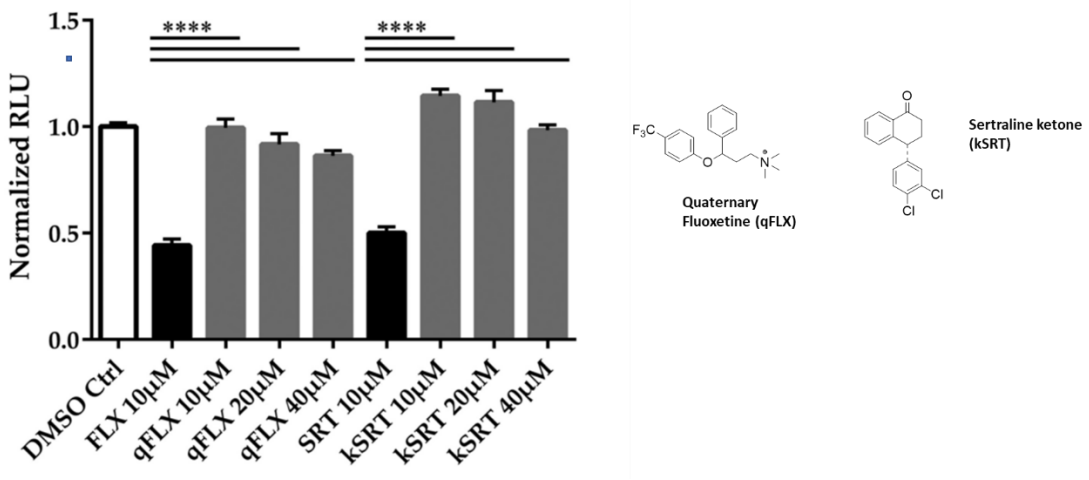



**Figure 2.5. Non-protonatable analogs do not restrict intracellular *Mtb*** by luminescent reporter (n ≥ 3, ±SEM). ****, P value of < 0.001 by ANOVA with Bonferroni's adjustment for multiple comparisons. Stepwise comparisons within each analog group are nonsignificant (P value of > 0.5 by the same test)

**Protonatable CAD compound accumulation in macrophages is partially pH dependent.** Tissue-level accumulation, especially in lung and spleen, has been demonstrated for established [20, 21] and emerging [22, 23] antitubercular compounds and is believed to enhance their efficacy against *M. tuberculosis* (see Figure 2.3). We sought to determine if CAD compounds accumulate within BMDM, and if so, the extent to which such accumulation depends on acidic compartments. Resting uninfected or infected BMDMs were exposed to 10 μM SRT, kSTR, FLX, qFLX, or clofazimine (CFZ) for 24 h under non-neutralizing or neutralizing (20 mM $NH_4Cl$) conditions. Analytes were extracted from macrophages, and the ratio of cellular concentration to medium concentration was compared to that of the vehicle control (Figure 2.6). SRT, FLX, and CFZ all showed accumulation that was stable enough to persist during the analyte extraction workup. Collecting cells by scraping at 4 °C, rather than trypsin treatment at 37 °C, did not affect the measured accumulation of a test compound (clofazimine; data not shown).

Accumulation was partially reversed by neutralizing acidic compartments. The partial attenuation of accumulation under neutralizing conditions suggests that SRT, FLX, and CFZ accumulate in acidic compartments but that acidic compartments are not the only reservoir for these compounds within cells. Flux into the phagosomal compartment may be sufficient, without accumulation, to restrict *Mtb*. Nonprotonatable analogs kSRT and qFLX did not accumulate stably under either condition. Infected macrophages showed significantly greater accumulation of SRT, FLX, and CFZ than uninfected cells, and that accumulation was similarly attenuated by neutralization with ammonium chloride.

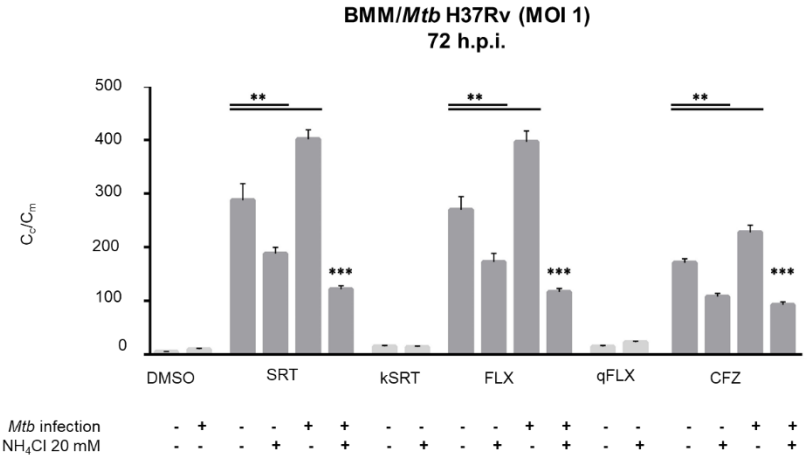
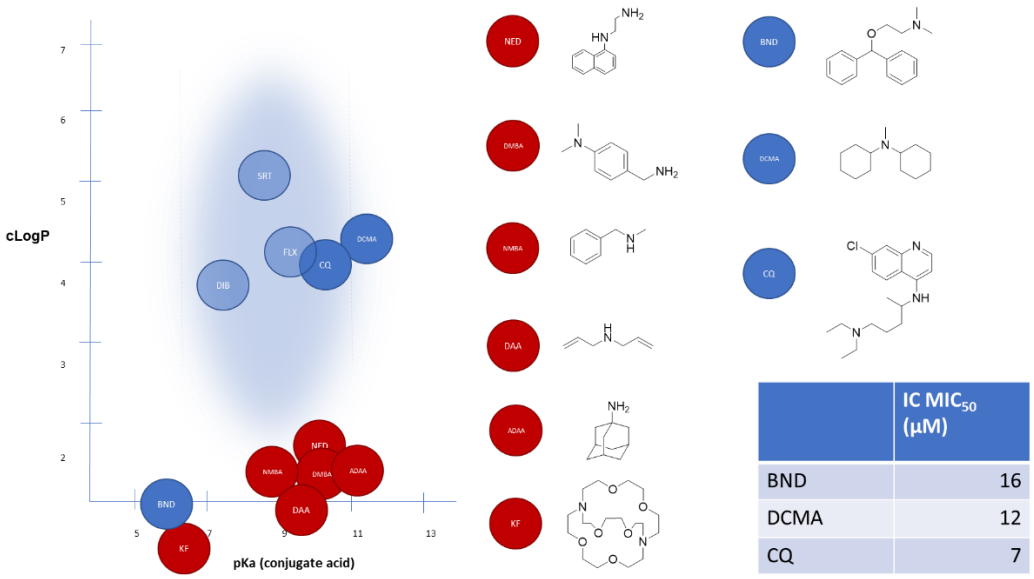



**Figure 2.6. CADs accumulate in infected and uninfected macrophages in a pH-dependent manner.** Intracellular concentration ($C_c$) of compounds relative to compound concentration in medium ($C_m$, 10 µM). BMM were exposed for 24 hours to sertraline (SRT), sertraline ketone (kSRT), fluoxetine (FLX), quaternary fluoxetine (qFLX), or clofazimine (CFZ) with or without ammonium chloride (20 mM) after 4 h of infection with M. tuberculosis (multiplicity of infection, 1:1) or mock infection. Analytes were quantified by UV absorbance (200 nm) by LC-MS at 72 hpi. SRT, FLX, and CFZ accumulation was partially reversible by ammonium chloride treatment, and accumulation was greater in *Mtb*-infected cells. Ammonium chloride also decreased accumulation in infected cells relative to infected cells without neutralization treatment. **(**** = $p \leq 0.01$ *** = $p \leq 0.001$ by ANOVA with Bonferroni's adjustment for multiple comparisons, n = 3, ±SEM).

**LogP and pKa alone do not define a pharmacophore for restriction of intracellular *Mtb*.** A vast number of small molecules possess chemical properties associated with lysosomal accumulation (LogP 3-7, pKa 7-11). The drugs tested thus far are all repurposed drugs or drug-like molecules and have chemical properties that place them solidly in the zone of predicted accumulators. Testing a wider array of compounds, including less lipophilic, but still protonatable, compounds would shed light on the physiochemical requirements for restricting intracellular *Mtb*.

BMM were infected with the luminescence Mtb reporter strain at an MOI of 1 and treated with the compounds in Figure 2.7 for 72 hours. All the protonatable, non-lipophilic, non-drug compounds failed to restrict intracellular Mtb. However, the lipophilic non-drug dicyclohexylmethylamine (DCMA) was found to have in intracellular $EC_{50}$ of 12 µM. Two other repurposed drugs, Benadryl (BND) and chloroquine (CQ) were also to have modest efficacy at 16 µM and 7 µM respectively. All three effective compounds have $EC_{50}$ in the high single-digit

to low double-digit micromolar range characteristic of other CADs effective against intracellular *Mtb*. While the drug CQ and the non-drug DCMA match the CAD model perfectly, the antihistamine BND is somewhat too hydrophilic to be a CAD yet still retains activity against intracellular *Mtb*. These results suggest lipophilicity and other drug-like properties are likely to be important for the sub-set of CADs that are effective against intracellular *Mtb*.




| | IC $MIC_{50}$ (μM) |
|---|---|
| BND | 16 |
| DCMA | 12 |
| CQ | 7 |

**Figure 2.7. Some unconventional CADs restrict intracellular Mtb.** Chemical structures (center) mapped on to calculated LogP and pKa (left). Intracellular IC $MIC_{50}$ for active compounds (table) determined by luminescent reporter at 72 hpi (representative of two independent experiments). $MIC_{50}$ is representative of two independent experiments. Abbreviations: NED = N-(1-Naphthyl)ethylenediamine, DMBA = Dimethylbenzylamine, NMBA = N-methylbenzylamine, DAA = Diallylamine, ADAA = adamanylamine, KF = Kryptofix 222, BND = benadryl, DCMA = dicyclohexylmethylamine, CQ = chloroquine.

**Some CADs and known antitubercular drugs induce phospholipidosis (PLD) in a pH-dependent manner.** Some CADs are known to be powerful inducers of phospholipidosis. In fact, phospholipidosis was first demonstrated in rat lung tissue following the systemic administration of chloroquine. The ability to induce PLD may be important to the mechanism of action for CAD efficacy, or it may be simply a correlate of efficacy. Even if PLD is only an artifact of CAD accumulation and not mechanistically important for restricting intracellular *Mtb*, many other PLD inducing compounds are known and some of them may prove valuable leads. Furthermore, the several emerging antitubercular drugs including bedaquiline (BDQ) and SQ-109 are perfect candidates for lysosomal accumulation and may also, therefore, induce PLD.

I sought to find direct evidence of PLD in macrophages treated with sertraline or the emerging antitubercular drug SQ-109 and, if PLD were present, to determine if PLD was pH-dependent. BMM infected at an MOI of 1 with a GFP-expressing strain of *Mtb* were treated with SRT or SQ-109 (10 µM) for 24 hours under non-neutralizing or neutralizing (20 mM $NH_4Cl$) conditions. Cells were treated with LipidTox, fixed and imaged by confocal microscopy. Sertraline and SQ-109 both induced strong phospholipidosis which was partly or near completely attenuated, respectively, under neutralizing conditions. DMSO treated controls shows no evidence of PLD under either condition.

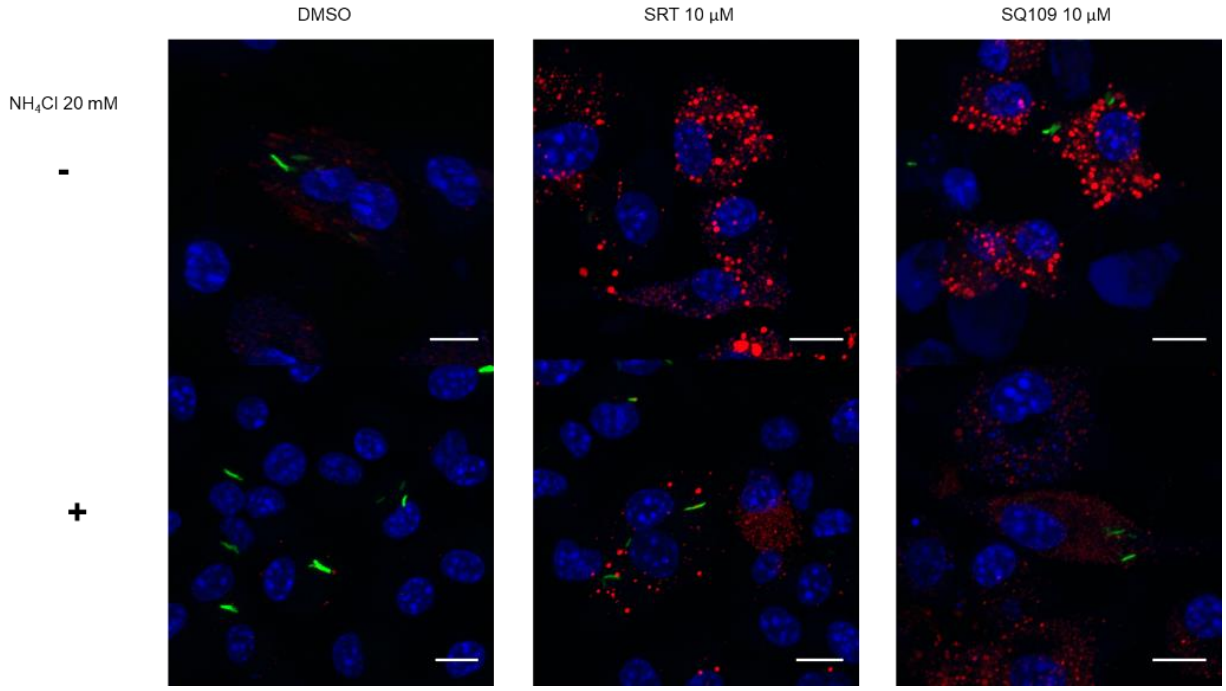



**Figure 2.8. Sertraline and SQ-109 induce pH-dependent PLD in infected macrophages.** BMM infected with Mtb:GFP at an MOI 1 were treated for 24 hours with CAD compounds sertraline (SRT) and SQ109 at 10 µM with or without concurrent neutralization by 20 mM $NH_4Cl$. Images are representative of two independent experiments. DAPI nuclear stain (blue), LipidTox stain (red), Mtb:GFP (green). Scale bar = 10 µm.

To determine if the PLD is present during treatment with a broader range of effective CADs and selected CAD and non-CAD antitubercular drugs, BMM were plated in 96-well plates and infected at an MOI of 1 with GFP expressing *Mtb*. Most compounds were applied at 10 µM with or without neutralizing conditions (20 mM $NH_4Cl$); Isoniazid was treated at 1 µM and Benadryl at 25 µM. 10 µM was chosen for all drugs to compare the drugs' relative ability to induce PLD while maintaining some likely efficacy against *Mtb* (Supplemental Table S.2.1). Infection and drug treatment proceeded for 48 hours after which cells were stained with LipidTox and

fluorescent signals measured on a plate reader. Results for PLD (left panel) and *Mtb* restriction (right panel) are shown in Figure 2.9.

As expected BMM not treated with drug showed no evidence of PLD and neutralization had only minimal effect on *Mtb* growth. Sertraline and SQ-109 performed similarly as in the experiment in Figure 2.8. PLD was strongly induced in SQ-109 and nearly eliminated with $NH_4Cl$ treatment, and SQ-109s ability to restrict *Mtb* was almost entirely pH dependent. Sertraline also produced PLD that was not entirely relieved by $NH_4Cl$ treatment. Restriction was partially pH-dependent for sertraline, fluoxetine and dibucaine similar to that the results found in Figure 2.4 with $NH_4Cl$ neutralization. These results support the validity of the plate reader assay for assessing both PLD with LipidTox and restriction with GFP-expressing *Mtb*.

The ability of CADs to induced PLD was highly variable. Bedaquiline and SQ-109 induced very strong PLD that was almost entirely pH-dependent. Fluoxetine, thioridazine and fluphenazine induced modest PLD that was largely pH-dependent, while sertraline induced more PLD that was less pH-dependent. Interestingly, clomipramine (CLO) produced no PLD. Likewise, somewhat against expectations, dibucaine and Benadryl produced no PLD and hydroxyzine produced very little. None of the non-CAD antitubercular drugs (ethambutol, isoniazid, linezolid) induced PLD.

The pH-dependence of restriction is more consistent for CADs than their ability to induce PLD. Only clomipramine shows no pH-dependence and several are strongly pH-dependent. Bedaquiline and SQ-109, whose PLD induction is so strongly pH-dependent, showed very little pH-dependence for restriction, suggesting that induction of PLD is not necessary for their activity. Ethambutol loses about half its efficacy under neutralized conditions which may be consistent with reports that ethambutol itself neutralizes to cause $Zn^{2+}$ accumulation in lysosomes [49]. However, only for hydroxyzine does neutralization completely abrogate restriction.

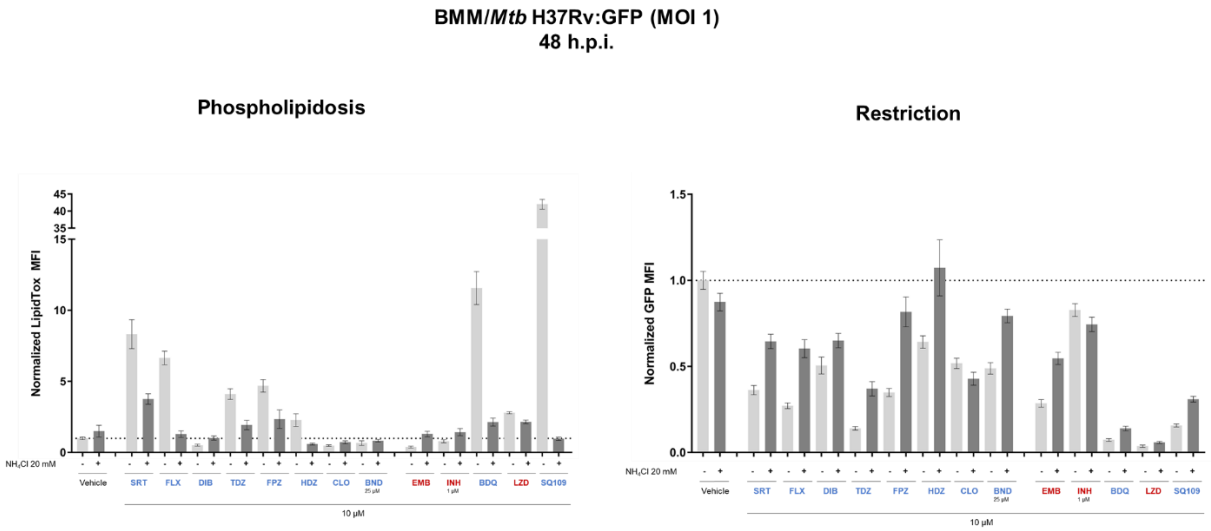



**Figure 2.9. CADs and known antituberculars assessed for pH-dependent phospholipidosis and Mtb restriction in BMM.** BMM infected with Mtb:GFP at an MOI 1 were treated with various CAD (blue) and non-CAD (red) known antitubercular compounds. At 48 hpi LipidTox staining was performed, cells were fixed and measured on a spectrophotometer. LipidTox MFI per and GFP MFI were normalized to untreated cells (untreated = 1). Error bars represent ±SEM for n = 3. Results are representative of two independent experiments. For abbreviations, see above. TDZ = thioridazine, EMB = ethambutol, CLO = clomipramine.

**Chemically modifiable CADs fluphenazine and hydroxyzine have efficacy against intracellular *Mtb*.** The modest efficacy of CADs limits their attractiveness as antitubercular agents. Their mechanisms of actions appear largely non-specific and their intracellular $EC_{50}$s would generally be difficult to obtain *in vivo*. However, their tropism and 100- to 400-fold intracellular accumulation suggest they might be useful as lipophilic carriers for more potent small molecules, particularly more hydrophilic compounds that have difficulty crossing membranes.

Most CADs, however, are not easily modifiable in their finished chemical form (Supplemental Figure S.2.1). Hydroxyzine (HDZ) and fluphenazine (FPZ), however, contain a primary alcohol that could be easily oxidized to an aldehyde which would allow the condensation of isoniazid or thiosemicabazides to create a two-component drug. An HDZ-INH or FPZ-INH two-component drug might achieve an enhanced intracellular $EC_{50}$ that could shorten treatment, lower dosing to avoid liver damage, or overcome INH resistance.

Therefore, this study sought to characterize the antitubercular and PLD inducing behavior of HDZ and FPZ as potential carrier moieties.

BMM were infected with the GFP-expressing Mtb strain in a 96-well format in Figure 2.10 and treated with compounds in a 2-fold dilution series for 72 hours post infection. FPZ was tested from 0.2 – 25 µM and HDZ was tested from 0.78 to 50 µM. Extracellular $EC_{50}$s were determined for planktonic cultures as above.

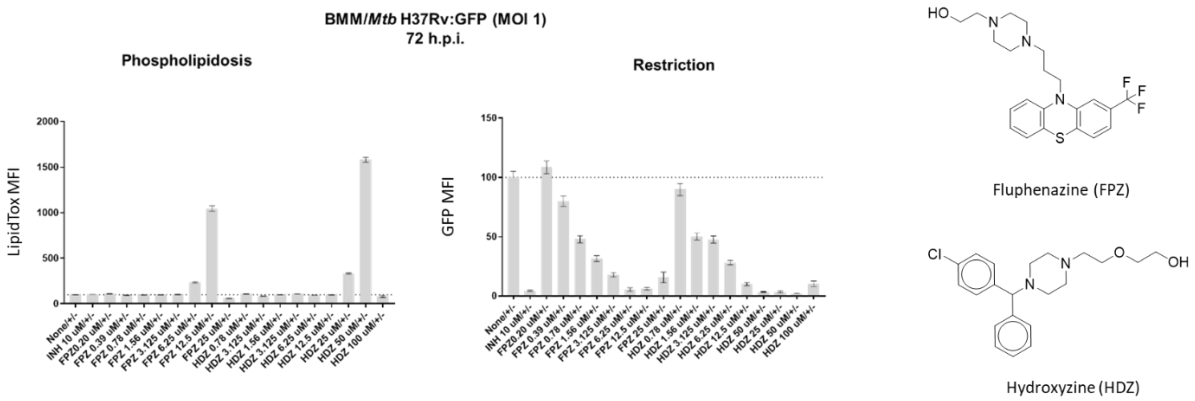



**Figure 2.10. Chemically modifiable PLD inducers restrict intracellular *Mtb*.** BMM infected with Mtb:GFP at an MOI 1 were treated with compounds fluphenazine (FPZ) and hydroxyzine (HDZ). At 72 hpi LipidTox staining was performed, cells were fixed and imaged. LipidTox MFI per cell and GFP MFI per cell were calculated will CellProfiler and normalized to untreated cells (untreated = 100). Error bars represent ±SEM for n = 3. Results are representative of two independent experiments.

Both compounds had IC $EC_{50}$ in the range common for CADs with an EC and IC ratio also typical of CADs demonstrating modest activity against intracellular *Mtb* (Table 2.1).

| Compound | EC $EC_{50}$ (µM) | IC $EC_{50}$ (µM) |
|---|---|---|
| **Hydroxyzine (HDZ)** | 150 | 5 |
| **Fluphenazine (FPZ)** | 45 | 1.5 |

**Table 2.1. Extracellular and intracellular $EC_{50}$ of hydroxyzine and fluphenazine.**

Both compounds also induced phospholipidosis with a very sharp on-set around 5 – 10 µM for FPZ and 25 µM for HDZ. The drop of PLD signal to undetectable at the top dose is caused by cytotoxicity and suggests a narrow therapeutic window if CADs were to be used as a single agent.

These results suggest HDZ and FPZ might be suitable scaffolds for conjugating isoniazid and other aldehyde reactive antitubercular drugs.

## Discussion

In his seminal 1974 work on the subject, Christian de Duve proposed that antibiotics with "lysosomotropic" properties should be more effective against intracellular pathogens than they are against the same pathogens in planktonic cultures [9]. Four decades later, the studies here

are, to my knowledge, the first investigation of that theory with regard to mycobacterial infection. Weak bases are more membrane permeable in their nonionized form [24] but become trapped inside acidic compartments when protonated. Actively maintained pH gradients give rise to orders-of-magnitude-sized asymmetric distributions of weak bases across cellular membranes such as lysosomal membranes. Dibucaine, a compound used in this study to restrict *M. tuberculosis* growth in macrophages, exhibits this behavior, in agreement with de Duve's theory, and produces large unilamellar vesicles, which are a model for membrane-enclosed compartments [15].

Although other groups have looked at the impact of pH-based partitioning on antibiotic pharmacokinetics generally [25, 26], and apparent accumulation of drugs used in the treatment of TB has been observed [27, 28], the basis for this accumulation has never been demonstrated in the context of mycobacterial infection. Our results demonstrate intracellular accumulation of several drugs to approximately 200 to 400 times the concentration present in the extracellular space. This accumulation was partially dependent on the pH gradient (Figure 2.6). This degree of concentration enables weakly antimycobacterial compounds fluoxetine, sertraline, and dibucaine to restrict *M. tuberculosis* in macrophages at when applied to cells at concentrations well below the level that would be needed for these same compounds to restrict *M. tuberculosis* in broth cultures (Figure 2.3). Non-protonatable analogs of these compounds were only able to restrict *M. tuberculosis* in broth and were not seen to accumulate in macrophages. However, we cannot rule out the possibility that dissipation of non-CAD compounds into wash buffers during workup obscured rapidly reversible accumulation. The enhanced accumulation of CAD compounds in *M. tuberculosis*-infected was even greater than in uninfected cells suggesting this phenomenon influences TB drug pharmacokinetics generally despite the well-documented ability of *M. tuberculosis* to limit acidification of its phagosomal environment.

The non-CAD compound isoniazid has been shown to be present at similar or lower concentrations inside macrophages relative to the extracellular space [27], and consistent with that finding, our results show no pH dependence in isoniazid restriction of *M. tuberculosis* during macrophage infection (Figure 2.4). The partial neutralization of (phago)lysosomes by CAD drugs due to their basicity may represent a countervailing effect to the direct antimicrobial action of some drugs [12]. This effect, if present, would decrease with more potently antimicrobial CAD drugs, though, since they would require much lower molar concentrations and would therefore have less alkalinizing effect than the CAD drugs in this study. It has been shown that chloroquine, a known lysosomal accumulator, does not decrease the activity of pyrazinamide, a drug only active at acidic pH, when applied to infected macrophages [30]. This suggests that strong alkalization of *M. tuberculosis*-containing compartments does not occur with that compound and may be generalizable. That finding, and the results with ammonium chloride and bafilomycin treatment alone (Figure 2.4), which were similar to published results reported by another group [18], suggests that acidic compartment neutralization alone does not profoundly impact the course of infection of macrophages with wild-type *M. tuberculosis*. Bafilomycin showed enough variability that it was necessary to pursue a second neutralization mechanism to confirm the result (e.g., Figure 2.4 results for Baf in combination with SRT and DIB).

The results here do not explain completely the mechanism by which CAD compounds achieve enhanced restriction. Accumulation of drugs (Figure 2.6) to levels that are directly bactericidal is only one possible mode of action. Physical accumulation is well supported by observations regarding clofazimine in the clinical literature [31–34], wherein crystals of drug have been observed in lung tissue of treated patients. Interest in clofazimine has recently intensified due to its successful use against multi-drug resistant *M. tuberculosis* [35, 36] and the demonstration that it can shorten treatment in a murine model of TB [37]. Still, a host-directed effect cannot be totally excluded, and evidence exists to suggest that loading lysosomes with clofazimine impacts the expression of lysosomal enzymes [38].

The impact of CAD drugs on the endogenous functions of the structures they accumulate within is difficult to predict. Host-directed effects that are beneficial for restriction may also result from CAD drug deposition such as phopholipidosis [39]. More speculatively, expanded lysosomal volume associated with PLD may prevent the close apposition of the bacterial cell wall to the host membrane, which has been reported to be necessary for phagosome maturation arrest [40], a key survival strategy of *M. tuberculosis*.

The results here demonstrate that some CADs do induce PLD to a very high degree (Figure 2.8, 2.9) including the emerging antitubercular drugs bedaquiline and SQ-109. Not all candidate CADs induce PLD at 10 µM while still producing pH-dependent restriction (Figure 2.9, dibucaine, Benadryl) suggesting phenotypically detectable PLD is not required for restriction. PLD is highly dose-dependent, emerges sharply with increasing doses and tends to lead to cytotoxicity at slightly higher doses (Figure 2.11). Cytotoxicity and narrow therapeutic windows with PLD-inducing drugs has always been a red flag in drug development.

The contention here is not that FLX, SRT, DIB are other CADs are viable drugs for the treatment of TB. Indeed, they do not appear to be clinically relevant despite previous reports of their antimicrobial activity [44–47]. Only for cryptococcal infection has the therapeutic index of one of the drugs (i.e., SRT) been suggested to be compatible with clinical treatment [47]. However, they do demonstrate a phenomenon which could increase the local concentration of antimicrobial drugs to which *M. tuberculosis* is exposed intracellularly. Rational modification of antibiotics to endow them with an CAD profile has been demonstrated. Renard and colleagues modified penicillin G (an otherwise non-accumulating, predominantly extracellular drug) by removing a carboxylic acid moiety and replacing it with a basic, amine functional group. That alteration was sufficient to cause a shift toward accumulation of the drug in the acidic compartment, primarily lysosomes, as identified by co-fractionation [48].

The CADs hydroxyzine and fluphenazine demonstrate pH-dependent mild PLD and intracellular restriction with intracellular $IC_{50}$s of 5 µM and 1.5 µM (Figure 2.10, Table 2.1). The primary alcohol on these compounds could be oxidized to form an aldehyde that would be perfectly suitable to conjugate isoniazid or carbazide bearing drugs to form a two component drug that would, ideally, accumulate in *Mtb* containing compartments.

**Materials and Methods**

**Macrophage cell culture.** All experiments were performed on resting primary murine bone marrowderived macrophages (BMDM) from C57BL/6 mice at a density of $5x10^4$/well in 200 µL of medium in 96-well cluster plates. BMDM medium was composed of Dulbecco's modified Eagle's medium (DMEM) supplemented with 10% fetal bovine serum (references 11960 and 10082; Gibco), glutamine as GlutaMAX (reference 35050; Gibco) at 2 mM, and 10 % 3T3-macrophage colony-stimulating factor cell conditioned medium. Macrophages were maintained at 37 °C, 5% $CO_2$ in a humidified incubator, and handling steps were executed as quickly as safely possible to minimize exposure to ambient conditions. For cytotoxicity measurement, CellTox green was used according to the manufacturer's instructions (G8741; Promega). For phospholipidosis measure and

**Bacterial culture.** All experiments were conducted with *M. tuberculosis* grown to mid-log phase. Bacteria were grown in 50 mL of Middlebrook 7H9 broth (271310; Difco) supplemented with 0.5 %v/v glycerol, 0.05 %w/v Tween 80 (P1754; Sigma), and 10 %v/v oleate-albumin-dextrose-catalase enrichment (Middlebrook OADC; catalog no. 212351; BBL). Cultures were maintained at 37 °C in 1-liter roller bottles. The Erdman strain of *M. tuberculosis* was used for all experiments except for those performed for liquid chromatography-mass spectrometry (LC-MS) analysis, for which the strain-matched control was H37Rv. The autoluminescent strain of *M.tuberculosis* Erdman, carrying the *luxCDABE* operon, was provided by Jeffrey Cox.

**MIC experiments and growth curves.** MICs were determined by a standard microtiter dilution protocol (49). Extracellular $IC_{50}$s were determined by monitoring growth of *M. tuberculosis* using optical density (600 nm) in 240 µL of complete 7H9 in 96-well plates in triplicate across a range of concentrations for each study drug and extrapolating the value which gave half-maximal inhibition. For growth curves, plates were maintained at 37 °C with 60-rpm circular agitation. All MIC experiments used 7H9 medium at pH 6.4 to mimic the physiologic pH of the niche inhabited by *M. tuberculosis*.

**Infection.** Bacteria were washed thrice in phosphate-buffered saline (PBS), resuspended, and centrifuged at 500 *g* to pellet clumps. Bacterial suspension was added to DMEM with 10 % horse serum substituted for FBS to produce infection medium at $5x10^5$ CFU/mL in 100 µL per well. Phagocytosis was allowed to proceed for 4 h, after which macrophages were washed twice with warm PBS and returned to BMDM growth medium.

**Drug treatment.** Immediately after infection, macrophages were returned to BMDM medium with or without experimental compounds as appropriate. For experiments involving neutralization of acidic organelles, macrophages were returned to 100 µl of BMDM medium with or without neutralization agent for 1 h, followed by a further 100 µl of medium containing 2-fold concentrated experimental compound or control dissolved in BMDM medium of the same composition as the first 100 µl to yield the target concentration of experimental drug.

**Bacterial load quantification.** To enumerate bacterial CFU, macrophages were lysed by adding 50 µl of 0.5% Triton X-100 to give a final concentration of 0.1% detergent. Serial dilutions were produced in complete 7H9 medium and plated on Middlebrook 7H10 agar plates (262710; Difco) containing 10% OADC and no antibiotics. CFU were counted after 17 to 21 days of incubation at 37°C in a humidified incubator.

For luminescence experiments, macrophages were maintained in white 96-well cluster plates (3610; Costar) with white vinyl sealing tape attached to the bottom (236272; Thermo Scientific) and read at 32 °C with a SpectraMax L luminometer (Molecular Devices). Triplicate reads were averaged for each of three biological replicates at each time point.

**Reagents.** The following compounds were purchased from Sigma-Aldrich: dibucaine (D0638), resazurin (R7017), ammonium chloride (A-9434), bafilomycin A1 (B1793), isoniazid (I3377), racemic fluoxetine (F132), serotonin (H9523), Triton X-100 (T8787), and clofazimine (C8895). The quaternary amine analog of fluoxetine was generous gifts of Eli Lilly and Co. Sertraline was from Enzo (BML-NS115), and the ketone analog was from Matrix Scientific (072144). Hoechst 33342 was from Anaspec (AS-83218). Calcein AM (C3100MP) and Vybrant DiI (V22885) were from Thermo Fisher. Drugs for use in infection experiments were dissolved in Hybri-Max dimethyl sulfoxide (DMSO) (D2650; Sigma) to give stock solutions at 1,000-fold their intended final concentration and filter sterilized via 0.2-µm nylon syringe filters. Solvent controls contained 0.125 %v/v DMSO.

**Compound extraction and LC-MS quantification.** BMDMs were plated on non-tissue culture treated 6-well plates (0877249; Corning Life Sciences) at $8x10^5$ cells/well and grown overnight in BMDM medium at 37 °C in humidified 5 % $CO_2$. Cells were mock infected by treatment with infection medium for 4 h or infected as described above. BMDMs were washed twice with warm PBS and then grown in BMDM medium with DMSO vehicle (0.1%) or compounds dissolved in DMSO at 10 µM with or without $NH_4Cl$ (20 mM) to accomplish acidic compartment neutralization. After 24 h, cells were washed twice in warm PBS and detached by incubation with 1 ml/well trypsin-EDTA (0.25%; Gibco) for 10 min at 37 °C. Trypsin was inactivated and cells transferred to 15-ml centrifuge tubes by gently aspirating wells with 2 ml warm PBS. Cells were collected by centrifugation (500 *g*/5 min/25 °C) and supernatants were fully decanted. Analytes were extracted from cell pellets in organic solvent (500 µL acetonitrile-methanol-water [2:2:1]), and 1 µL of freshly prepared 10 mM stocks of clomipramine or clofazimine was used as an internal standard. Cells were disrupted by adding 0.1-mm glass beads and beating in an MP Biomedicals FastPrep-24 homogenizer (two cycles of 30 s at 6.0 m/s). Cellular debris was pelleted by centrifugation (2,800 *g*/5 min/25 °C) and the organic supernatant collected. A second extraction (500 µL; organic solvent without internal standard) was followed by vigorous vortexing (30 s twice) and centrifugation as described above. The organic extracts were combined and stored at -80°C. Analytes extracted from *M. tuberculosis* infection experiments were additionally filter sterilized (0.2 µm; polyvinylidene difluoride [PVDF]) twice prior to removal from the biosafety level 3 facility. Analytes were quantified by UV absorbance (200 nm) on an Agilent 1260 infinity high-performance liquid chromatograph in

tandem with an Agilent 6120 quadrupole mass spectrometer. Separation was performed on Agilent Poroshell 120 EC-C18 2.7-µm columns (4.6 by 50 mm for SRT, kSRT, and FLX; 4.6 by 150 mm for qFLX) at 25 °C and a flow rate of 0.4 ml/min. Mobile-phase solvents were H2O plus 0.1 % trifluoroacetic acid (TFA) (solvent A) and acetonitrile plus 0.1 % TFA (solvent B). The eluent profile for SRT and FLX was the following: *T*0: 35 % solvent B, *T*20: 35 % solvent B, *T*21: 80 % solvent B, *T*26: 80 % solvent B, *T*27: 35 % solvent B, and *T*30: 35 % solvent B. The eluent profile for qFLX, kSRT, and clofazamine had the same time increments but contained 50 % solvent B for the isocratic and re-equilibration segments. Samples were thawed and passed throughout 0.2-µm filters (PVDF; EMD Millipore), and equal volumes (15 µL) were analyzed for all samples. UV detection was carried out at 200 nm, and *m/z* was determined in positive mode. Analyte peak retention times and mass signatures were determined from pure standards. Experimental samples were analyzed in duplicate, and concentration was determined from a standard curve run in triplicate in the same analytical sequence as the experimental samples.

**Imaging.** BMDM were grown at a density of $1x10^5$/well in eight-chambered coverglass culture slides (155411; Nunc) overnight, infected with *Mtb* at an MOI of 1 followed by drug treatment for 24 hours. Cells were treated with LipidTox Red (ThermoFisher H34351) according to manufacturer's instructions. Cells were washed twice with PBS, fixed with 4 % paraformaldehyde and removed from the BSL3 for imaging.

For cellular volume studies, cells were grown on glass coverslips, treated as described above, and then stained with Hoechst 33342 (3.25 µM), calcein AM (1 µM), and Vybrant DiI (3.5 µM) for 20 min prior to fixation with 4 % paraformaldehyde (15 min). Coverslips were mounted in Vectashield mounting medium (Vector Laboratories). Imaging was performed on a Nikon Ti-E fluorescence microscope coupled with an A1R confocal system (60x objective, 0.5-µm Z-step size). Three-dimensional image reconstruction and cell volume calculations were performed in Imaris (v. 8.2.0; Bitplane) for at least 500 cells from a minimum of eight fields of view distributed across two biological replicates, each containing two technical replicates. Images were processed and analyzed by ImageJ software (U.S. National Institutes of Health, Bethesda, MD).

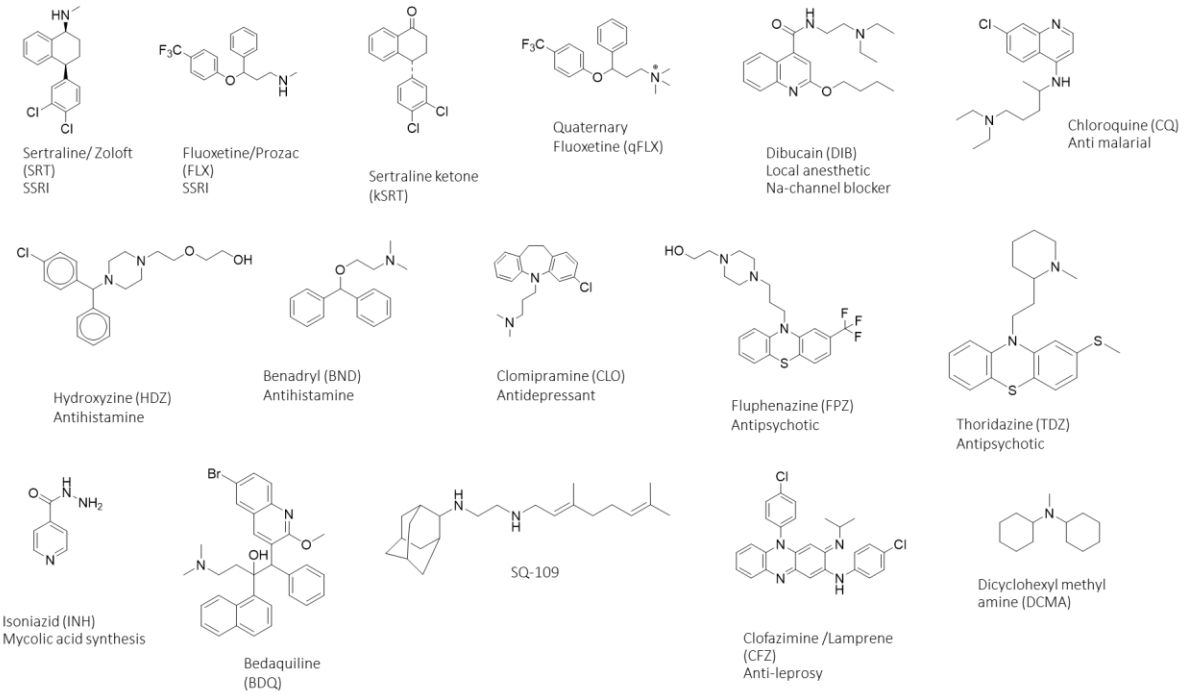
**Statistics and chemical property prediction.** All statistical analyses were performed with Prism (GraphPad Software, San Diego, CA). Marvin was used to draw structures, and calculator plugins were used for structure property prediction and calculation, including CLogP, LogD, and pKa (Marvin, version 15.5.11.0; ChemAxon; chemaxon.com).

**Supplemental Information**

Table S.2.1. Summary of CAD accumulation and extracellular and intracellular restriction metrics.

| Compound | Accumulation $C_c/C_m$ (infected MO) | EC $MIC_{50}$ (µM) | IC $MIC_{50}$ (µM) |
|---|---|---|---|

| | | | |
|---|---|---|---|
| **Sertraline (SRT)** | 400 | 137 | 10 |
| **SRT ketone (kSRT)** | NA | 355 | Inactive |
| **Fluoxetine (FLX)** | 400 | 164 | 8 |
| **qFluoxetine (qFLX)** | ND | 305 | Inactive |
| **Dibucaine (DIB)** | 120 | 771 | 10 |
| **Clofazimine (CFZ)** | 240 | 40 | 20 |
| **Hydroxyzine (HDZ)** | ND | 150 | 5 |
| **Fluphenazine (FPZ)** | ND | 45 | 1.5 |
| **Bedaquiline (BDQ)** | 340 | 10 | 0.6 |
| **Benadryl (BND)** | ND | ND | 16 |
| **Dicyclohexylmethylamine (DCMA)** | ND | ND | 12 |
| **Chloroquine (CQ)** | NA | ND | 7 |
| **Isoniazid (INH)** | ND | 0.31 | 0.63 |




**Supplemental Figure S.2.1. Chemical structures of selected CAD compounds in this study.**

## Acknowledgements

The quaternary amine analog of fluoxetine was generous gifts of Eli Lilly and Co. This research was supported by funding from the National Institutes of Health (NIH Grant No. AI51622).

**References**

1. Global Burden of Disease Study. 2015. Global, regional, and national age-sex specific all-cause and cause-specific mortality for 240 causes of death, 1990-2013: a systematic analysis for the Global Burden of Disease Study 2013. Lancet 385:117–171. https://doi.org/10.1016/S0140-6736(14)61682-2.

2. Dye C, Scheele S, Dolin P, Pathania V, Raviglione MC. 1999. Consensus statement. Global burden of tuberculosis: estimated incidence, prevalence, and mortality by country. WHO Global Surveillance and Monitoring Project. JAMA 282:677– 686.

3. Blumberg HM, Burman WJ, Chaisson RE, Daley CL, Etkind SC, Friedman LN, Fujiwara P, Grzemska M, Hopewell PC, Iseman MD, Jasmer RM, Koppaka V, Menzies RI, O'Brien RJ, Reves RR, Reichman LB, Simone PM, Starke JR, Vernon AA. 2003. American Thoracic Society/Centers for Disease Control and Prevention/Infectious Diseases Society of America: treatment of tuberculosis. Am J Respir Crit Care Med 167:603– 662. https://doi.org/10.1164/rccm.167.4.603.

4. Gandhi NR, Nunn P, Dheda K, Schaaf HS, Zignol M, van Soolingen D, Jensen P, Bayona J. 2010. Multidrug-resistant and extensively drug resistant tuberculosis: a threat to global control of tuberculosis. Lancet 375:1830 –1843. https://doi.org/10.1016/S0140-6736(10)60410-2.

5. Zhang Y, Mitchison D. 2003. The curious characteristics of pyrazinamide: a review. Int J Tuberc Lung Dis 7:6 –21.

6. Stanley SA, Barczak AK, Silvis MR, Luo SS, Sogi K, Vokes M, Bray M-A,Carpenter AE, Moore CB, Siddiqi N, Rubin EJ, Hung DT. 2014. Identification of host-targeted small molecules that restrict intracellular *MycobaMycobacterium tuberculosis* growth. PLoS Pathog 10:e1003946. https://doi.org/10.1371/journal.ppat.1003946.

7. MacIntyre AC, Cutler DJ. 1988. The potential role of lysosomes in tissue distribution of weak bases. Biopharm Drug Dispos 9:513–526. https://doi.org/10.1002/bod.2510090602.

8. Daniel WA, Wojcikowski J. 1997. Contribution of lysosomal trapping to the total tissue uptake of psychotropic drugs. Pharmacol Toxicol 80:62–68. https://doi.org/10.1111/j.1600-0773.1997.tb00285.x.

9. de Duve C, de Barsy T, Poole B, Trouet A, Tulkens P, Van Hoof F. 1974. Lysosomotropic agents. Biochem Pharmacol 23:2495–2531. https://doi.org/10.1016/0006-2952(74)90174-9.

10. Kaufmann AM, Krise JP. 2007. Lysosomal sequestration of amine containing drugs: analysis and therapeutic implications. J Pharm Sci 96:729 –746. https://doi.org/10.1002/jps.20792.

11. Rohde K, Yates RM, Purdy GE, Russell DG. 2007. Mycobacterium tuberculosis and the environment within the phagosome. Immunol Rev 219:37–54. https://doi.org/10.1111/j.1600-065X.2007.00547.x.

12. Vandal OH, Nathan CF, Ehrt S. 2009. Acid resistance in Mycobacterium tuberculosis. J Bacteriol 191:4714 – 4721. https://doi.org/10.1128/JB.00305-09.

13. Pethe K, Swenson DL, Alonso S, Anderson J, Wang C, Russell DG. 2004. Isolation of Mycobacterium tuberculosis mutants defective in the arrest of phagosome maturation. Proc Natl Acad Sci U S A 101:13642–13647. https://doi.org/10.1073/pnas.0401657101.

14. Sturgill-Koszycki S, Schlesinger P, Chakraborty P, Haddix P, Collins H, Fok A, Allen R, Gluck S, Heuser J, Russell D. 1994. Lack of acidification in Mycobacterium phagosomes produced by exclusion of the vesicular proton-ATPase. Science 263:678 – 681. https://doi.org/10.1126/science.8303277.

15. Mayer LD, Wong KF, Menon K, Chong C, Harrigan PR, Cullis PR. 1988. Influence of ion gradients on the transbilayer distribution of dibucaine in large unilamellar vesicles. Biochemistry 27:2053–2060. https://doi.org/10.1021/bi00406a036.

16. Hiemke C, Hartter S. 2000. Pharmacokinetics of selective serotonin reuptake inhibitors. Pharmacol Ther 85:11–28. https://doi.org/10.1016/S0163-7258(99)00048-0.

17. Poole B, Ohkuma S. 1981. Effect of weak bases on the intralysosomal pH in mouse peritoneal macrophages. J Cell Biol 90:665– 669. https://doi.org/10.1083/jcb.90.3.665.

18. Sullivan JT, Young EF, McCann JR, Braunstein M. 2012. The Mycobacterium tuberculosis SecA2 system subverts phagosome maturation to promote growth in macrophages. Infect Immun 80:996 –1006. https://doi.org/10.1128/IAI.05987-11.

19. Anonymous. 2008. Clofazimine. Tuberculosis 88:96 –99. https://doi.org/10.1016/S1472-9792(08)70006-4.

20. Liu L, Xu Y, Shea C, Fowler JS, Hooker JM, Tonge PJ. 2010. Radiosynthesis and bioimaging of the tuberculosis chemotherapeutics isoniazid, rifampicin and pyrazinamide in baboons. J Med Chem 53:2882–2891. https://doi.org/10.1021/jm901858n.

21. Weinstein EA, Liu L, Ordonez AA, Wang H, Hooker JM, Tonge PJ, Jain SK. 2012. Noninvasive determination of 2-[18F]-fluoroisonicotinic acid hydrazide pharmacokinetics by positron emission tomography in Mycobacterium tuberculosis-infected mice. Antimicrob Agents Chemother 56:6284–6290. https://doi.org/10.1128/AAC.01644-12.

22. Jia L, Tomaszewski JE, Hanrahan C, Coward L, Noker P, Gorman G, Nikonenko B, Protopopova M. 2005. Pharmacodynamics and pharmacokinetics of SQ109, a new diamine-based antitubercular drug. Br J Pharmacol 144:80–87.

23. Prideaux B, Dartois V, Staab D, Weiner DM, Goh A, Via LE, Barry CE, III, Stoeckli M. 2011. High-sensitivity MALDI-MRM-MS imaging of moxifloxacin distribution in tuberculosis-infected rabbit lungs and granulomatous lesions. Anal Chem 83:2112–2118. https://doi.org/10.1021/ac1029049.

24. Milne MD, Scribner BH, Crawford MA. 1958. Non-ionic diffusion and the excretion of weak acids and bases. Am J Med 24:709 –729. https://doi.org/10.1016/0002-9343(58)90376-0.

25. Lemaire S, Van Bambeke F, Tulkens PM. 2009. Cellular accumulation and pharmacodynamic evaluation of the intracellular activity of CEM-101, a novel fluoroketolide, against Staphylococcus aureus, Listeria monocytogenes, and Legionella pneumophila in human THP-macrophages. Antimicrob Agents Chemother 53:3734 –3743. https://doi.org/10.1128/AAC.00203-09.

26. Togami K, Chono S, Seki T, Morimoto K. 2010. Intracellular pharmacokinetics of telithromycin, a ketolide antibiotic, in alveolar macrophages. J Pharm Pharmacol 62:71–75. https://doi.org/10.1211/jpp.62.01.0007.

27. Hand WL, Corwin RW, Steinberg TH, Grossman GD. 1984. Uptake of antibiotics by human alveolar macrophages. Am Rev Respir Dis 129: 933–937.

28. Pascual A, Tsukayama D, Kovarik J, Gekker G, Peterson P. 1987. Uptake and activity of rifapentine in human peritoneal macrophages and polymorphonuclear leukocytes. Eur J Clin Microbiol 6:152–157. https://doi.org/10.1007/BF02018197.

29. Rastogi N, Potar M-C, David H. 1987. Intracellular growth of pathogenic mycobacteria in the continuous murine macrophage cell line J-774: ultrastructure and drug-susceptibility studies. Curr Microbiol 16:79 –92. https://doi.org/10.1007/BF01588176.

30. Crowle AJ, May MH. 1990. Inhibition of tubercle bacilli in cultured human macrophages by chloroquine used alone and in combination with streptomycin, isoniazid, pyrazinamide, and two metabolites of vitamin D3. Antimicrob Agents Chemother 34:2217–2222. https://doi.org/10.1128/AAC.34.11.2217.

31. Harbeck RJ, Worthen GS, Lebo TD, Peloquin CA. 1999. Clofazimine crystals in the cytoplasm of pulmonary macrophages. Ann Pharmacother 33:250. https://doi.org/10.1345/aph.18170.

32. Sandler ED, Ng VL, Hadley WK. 1992. Clofazimine crystals in alveolar macrophages from a patient with the acquired immunodeficiency syndrome. Arch Pathol Lab Med 116:541–543.

33. Silverman JF, Holter JF, Berns LA, Benning TL, Neill JS. 1993. Negative images due to clofazimine crystals simulating MAI infection in a bronchoalveolar lavage specimen. Diagn Cytopathol 9:534 –540. https://doi.org/10.1002/dc.2840090512.

34. Hudson V, Cox F, Taylor L, Guill M, Wray B, Steele J. 1988. Pulmonary clofazimine crystals in a child with acquired immunodeficiency syndrome and disseminated Mycobacterium avium-intracellulare infection. Pediatr Infect Dis J 7:880–882.

35. Caminero JA, Sotgiu G, Zumla A, Migliori GB. 2010. Best drug treatment for multidrug-resistant and extensively drug-resistant tuberculosis. Lancet Infect Dis 10:621– 629. https://doi.org/10.1016/S1473-3099(10)70139-0.

36. Dey T, Brigden G, Cox H, Shubber Z, Cooke G, Ford N. 2013. Outcomes of clofazimine for the treatment of drug-resistant tuberculosis: a systematic review and meta-analysis. J Antimicrob Chemother 68:284 –293. https://doi.org/10.1093/jac/dks389.

37. Tyagi S, Ammerman NC, Li S, Adamson J, Converse PJ, Swanson RV, Almeida DV, Grosset JH. 2015. Clofazimine shortens the duration of the first-line treatment regimen for experimental chemotherapy of tuberculosis. Proc Natl Acad Sci U S A 112:869–874. https://doi.org/10.1073/pnas.1416951112.

38. Sarracent J, Finlay CM. 1982. The action of clofazimine on the level of lysosomal enzymes of cultured macrophages. Clin Exp Immunol 48: 261–267.

39. Mesens N, Steemans M, Hansen E, Verheyen GR, Van Goethem F, Van Gompel J. 2010. Screening for phospholipidosis induced by central nervous drugs: comparing the predictivity of an in vitro assay to high throughput in silico assays. Toxicol In Vitro 24:1417–1425. https://doi.org/10.1016/j.tiv.2010.04.007.

40. de Chastellier C, Forquet F, Gordon A, Thilo L. 2009. Mycobacterium requires an all-around closely apposing phagosome membrane to maintain the maturation block and this apposition is re-established when it rescues itself from phagolysosomes. Cell Microbiol 11:1190 –1207. https://doi.org/10.1111/j.1462-5822.2009.01324.x.

41. Wong DT, Perry KW, Bymaster FP. 2005. The discovery of fluoxetine hydrochloride (Prozac). Nat Rev Drug Discov 4:764 –774.

42. Jackson JC, Walker RF, Brooks WH, Roszman TL. 1988. Specific uptake of serotonin by murine macrophages. Life Sci 42:1641–1650. https://doi.org/10.1016/0024-3205(88)90443-2.

43. Koch S, Perry KW, Nelson DL, Conway RG, Threlkeld PG, Bymaster FP. 2002. R-fluoxetine increases extracellular DA, NE, as well as 5-HT in rat prefrontal cortex and hypothalamus: an in vivo microdialysis and receptor binding study. Neuropsychopharmacology 27:949 –959. https://doi.org/10.1016/S0893-133X(02)00377-9.

44. Munoz-Bellido JL, Munoz-Criado S, Garcia-Rodriguez JA. 2000. Antimicrobial activity of psychotropic drugs: selective serotonin reuptake inhibitors. Int J Antimicrob Agents 14:177–180. https://doi.org/10.1016/S0924-8579(99)00154-5.

45. Bohnert JA, Szymaniak-Vits M, Schuster S, Kern WV. 2011. Efflux inhibition by selective serotonin reuptake inhibitors in Escherichia coli. J Antimicrob Chemother 66:2057–2060. https://doi.org/10.1093/jac/dkr258.

46. Coban AY, Tanriverdi Cayci Y, Keles Uludag S, Durupinar B. 2009. Investigation of antibacterial activity of sertralin. Mikrobiyol Bul 43:651– 656.

47. Zhai B, Wu C, Wang L, Sachs MS, Lin X. 2012. The antidepressant sertraline provides a promising therapeutic option for neurotropic cryptococcal infections. Antimicrob Agents Chemother 56:3758 –3766. https://doi.org/10.1128/AAC.00212-12.

48. Renard C, Vanderhaeghe HJ, Claes PJ, Zenebergh A, Tulkens PM. 1987. Influence of conversion of penicillin G into a basic derivative on its accumulation and subcellular localization in cultured macrophages. Antimicrob Agents Chemother 31:410 – 416. https://doi.org/10.1128/AAC.31.3.410.

49. Yamada, D., Saiki, S., Furuya, N., Ishikawa, K.-I., Imamichi, Y., Kambe, T., Fujimura, T., Ueno, T., Koike, M., Sumiyoshi, K., & Hattori, N. (2016). Ethambutol neutralizes lysosomes and causes lysosomal zinc accumulation. *Biochemical and Biophysical Research Communications*, *471*(1), 109–116. https://doi.org/https://doi.org/10.1016/j.bbrc.2016.01.171

## Chapter 3: Assessment of the *in vivo* virulence of B.1.427/1.429 (epsilon) SARS-CoV-2 variants relative ancestral B.1 (614G).

### Introduction

SARS-CoV-2 variants are defined as novel viruses that contain one or more mutations relative to ancestral viruses. SARS-CoV-2 variants are designated by public health agencies as "variants of concern" (VOC) or "variants of interest" (VOI) if they seem to have enhanced human transmission or pathology based on epidemiology or enhanced resistance to vaccine-induced immune responses [1]. With the identification in humans of at least five circulating variants of concern (VOC) in the last 12 months from the UK, South Africa, Brazil, India, and California [2-4], it is apparent that SARS-CoV-2 VOCs will continue to emerge for the foreseeable future in the human population. These new variants are replacing formerly dominant variants and sparking new COVID-19 outbreaks. To avoid an uncontrolled SARS-CoV-2 pandemic, an ongoing effort is needed to monitor, collect, and analyze data on new SARS-CoV-2 variants, identify VOCs and determine their impact on the performance of COVID-19 diagnostics and the efficacy of available treatments and vaccines.

In early January 2021, two novel SARS-CoV-2 lineages, designated B.1.427 and B.1.429 (epsilon variants), were detected in California (CA) [5]. Epidemiologic studies suggest that the variants originated in CA and were responsible for an increasing proportion of cases beginning in November 2020 until more than 50% of the cases in in the state were due to the epsilon variant in February 2021 [5]. This suggested that epsilon (B.1.427/B.1.429) variant had a moderately increased transmission efficiency in the population relative to the previously dominant B.1 (614G). In spring 2021, the WHO and CDC listed B.1.429/B.1.427 (epsilon) as a VOC. However, by July 2021 the epsilon variant had been dropped as a VOC and by October 2021 had been downgraded to "variant under montoring" (VUM). [1,6]

In-vitro studies demonstrated that the L452R spike mutation found in the B.1.427/B.1.429 variant increases infectivity and decreases susceptibility to antibody neutralization, rendering these CA VOCs completely resistant to one therapeutic monoclonal antibody, bamlanivimab [5]. B.1.427/429 has also been shown to partially escape vaccine elicited polyclonal and monoclonal neutralizing antibodies, using a novel mechanism of immune evasion [7,8]. A 2- to 3-fold reduction in the plasma neutralizing antibody titers against B.1.427/B.1.429 compared to ancestral B.1 (614G) variants in recipients of the Moderna mRNA vaccine was observed [7]. This finding was confirmed by a recent report showing that neutralizing titers in plasma from Wu-1 based mRNA vaccinees or from recovered patients were 2- to 3.5-fold lower against the B.1.427/B.1.429 variant relative to B.1 (614G) pseudoviruses [8]. Further, the L452R mutation reduced neutralizing activity in a subset of receptor binding domain-specific monoclonal (m)Abs tested, and the S13I and W152C mutations abrogated neutralization by all N-terminal domain-specific mAbs tested [8]. Taken together these data provide evidence that the epsilon (B.1.427/B.1.429) variant partially evades the human immune response [7,8].

Syrian hamsters are a widely used small animal model to study the infectivity and virulence of clinical SARS-CoV-2 isolates [9-13]. Following intranasal inoculation, hamsters are infected with SARS-CoV-2 and develop moderate to severe lung pathology. SARS-CoV-2–infected hamsters mount neutralizing antibody responses and are protected against homologous and heterologous re-challenge with SARS-CoV-2 [12,14,15]. In this study, the hamster model is used to determine the relative fitness and transmissibility of the ancestral SARS-CoV-2 and the B.1.427/429 variants in hamsters, and whether hamsters previously infected with the ancestral B.1 (614G) are susceptible to acute reinfection with B.1.427 or B.1.429.

This study demonstrates that the B.1.427/429 variants are more virulent than the ancestral B.1 (614G) variant, as measured by weight loss of infected animals, viral RNA levels in oral swabs and histopathology of the lungs. These findings are consistent with human clinical data and help explain the emergence and rapid spread of this variant in early 2021.

**Results**

**Body weight loss in hamsters inoculated with SARS-CoV-2 epsilon (B.1.429/427) is more severe and sustained than in hamsters infected with ancestral B.1 (614G) SARS-CoV-2.** To assess the virulence of SARS-CoV-2 variants, hamsters were infected intranasally with approximately 5000 PFU of B.1 (614G, B.1.427), or B.1.429 (Table S.3.1). Body weights and oral swabs were obtained daily, and lungs collected at necropsy on 2-, 4-, 6-, and 10-days post-inoculation were examined for pathologic changes and to determine the extent and level of virus replication (Table S.3.1.1). Hamsters inoculated with SARS-CoV-2 began losing weight at day 2-3 PI with a nadir lasting from 4-6 days PI in B.1 (614G) animals, from 4-7 days PI in B.1.427 animals and from 4-8 days PI in B.1.429 animals. The difference in weight loss between the B.1 (614G) animals and epsilon (427/429) animals was statistically significant (Figure 3.1A).

**Intranasal inoculation of hamsters with SARS-CoV-2 B.1.429 results in more severe pulmonary pathology compared to B.1.427 or ancestral B.1 (614G) SARS-CoV-2.** All hamsters inoculated with the 3 SARS-CoV-2 variants developed moderate to severe broncho-interstitial pneumonia. To quantify the extent and severity of lung pathology, 2 scoring systems were used: the first evaluated all relevant changes in the lungs of the infected animals (Figure 3.1B) and the second evaluated only the pathology associated with the pulmonary vasculature (Figure 3.1C). In all animals, the extent of lung pathology increased from days 2-6 and decreased dramatically by 10 days post-infection (Figure 3.1B and C). However, the lungs from hamsters infected with B.1.429 had a trend toward higher overall pathology scores compared to animals infected with B.1 (614G) or B.1.427 (Figure 3.1B). B.1.429 inoculated animals exhibited more widespread and severe lesions at 2 days PI than B.1 (614G) and B.1.427 inoculated animals. These early severe histopathological changes also persisted for a longer time in B.1.429 infections as seen by comparison of the scores at days 2 and 10 (Figure 3.1B). Thus, the area under the curve for overall lung pathology for the animals in Figure 3.1B was 150, 147 and 169.7 for B.1 the (614G), B.1.427and B.1.429, respectively.

Vascular pathology does not seem to contribute to the weight loss in SARS-CoV-2 infection, as hamsters infected with B.1.429 tended to have less vascular pathology than animals infected with B.1 (614G) or B.1.427 (Figure 3.1C). It must be noted however that lungs of only 3 animals/group at each time point were adequately perfused for scoring, which limits the strength of the conclusions that can be drawn from comparing these scores. Despite that limitation, it seems clear that B1.429 infection induces moderate to severe lung pathology more quickly and for a longer duration than B.1. (614G) and B.1.427 infections.

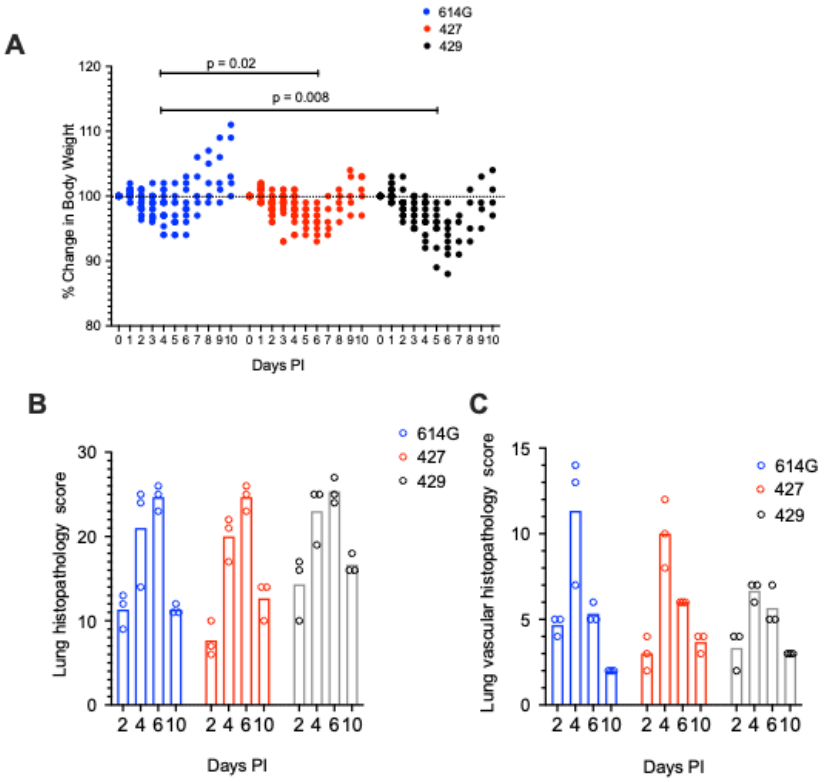



**Figure 3.1. Change in body weight and lung histopathology scores in hamsters after intranasal inoculation with B.1 (614G), B.1.427 and B.1.429. A)** Change in body weight relative to the day of inoculation. Mean values from all groups were compared by fitting a mixed model, and a post-hoc multiple comparison test was used to compare the mean values of the 427 or 429 groups individually to the 614G group. **B)** Total lung histopathology score (see methods for explanation). **C)** Lung vascular histopathology score (see methods for explanation). In A, top of bars indicate mean values in B and C.

Although the extent, severity and timing of the lesions differed among animals infected with the different variants, the overall nature of the broncho-interstitial pneumonia was similar in all animals infected with any of the 3 variants. At day 2 PI, lesions were centered on large airways and ranged from mild bronchitis to patchy, moderate bronchiolitis, bronchiolar epithelial cell necrosis and rupture of bronchiolar wall with limited extension of a mixed inflammatory

infiltrate (composed of neutrophils, macrophages, fewer lymphocytes and scattered multinucleated syncytial cells) into adjacent alveolar septa (Figures 3.2 and 3.3 B, G, and L). The affected pulmonary surface area in examined sections ranged from 2 to 20% (Figure 3.2 B, G, and L). Perivascular cuffing, intramural inflammatory cells and endothelialitis (sub-and intra-endothelial inflammatory cell infiltration), was noted in association with all SARS-CoV-2 variants, although more prominently in animals inoculated with B.1 (614G) and B.1.427. As noted above, the B.1.429 inoculated animals exhibited much more widespread and severe lesions at day 2 PI than B.1 (614G) and B.1.427 inoculated animals.

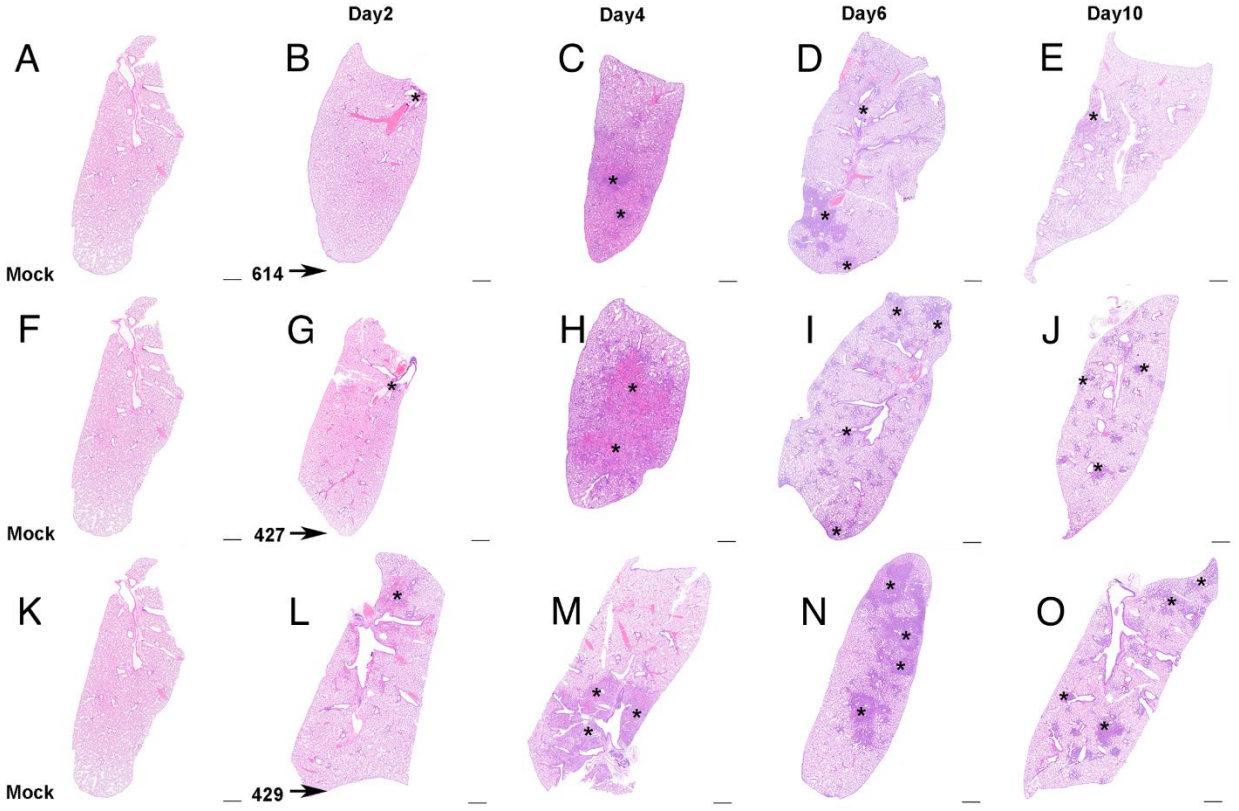



**Figure 3.2. Lung histopathology in hamsters after intranasal inoculation with B.1.429 is more acute and prolonged than in hamsters inoculated with B.1 (614G) and B.1.427. A, F, K) Sub-gross** histology of normal lungs from uninfected hamsters. Top row: **Sub-gross** histology of B.1 (614G) infection after **B)** 2 days PI, **C)** 4 days PI, **D)** 6 days PI, **E)** 10 days PI. Middle row: **Sub-gross** histology of B.1.427 infection after **G)** 2 days PI, **H)** 4 days PI, **I)** 6 days PI, **J)** 10 days PI. Bottom row: **Sub-gross** histology of B.1.429 infection after **L)** 2 days PI, **M)** 4 days PI, **N)** 6 days PI, **O)** 10 days PI. Asterisks= foci of inflammation, necrosis and/or hemorrhage. Hematoxylin and eosin stain. Original magnification: 1x. Scale bars equal 1 mm.

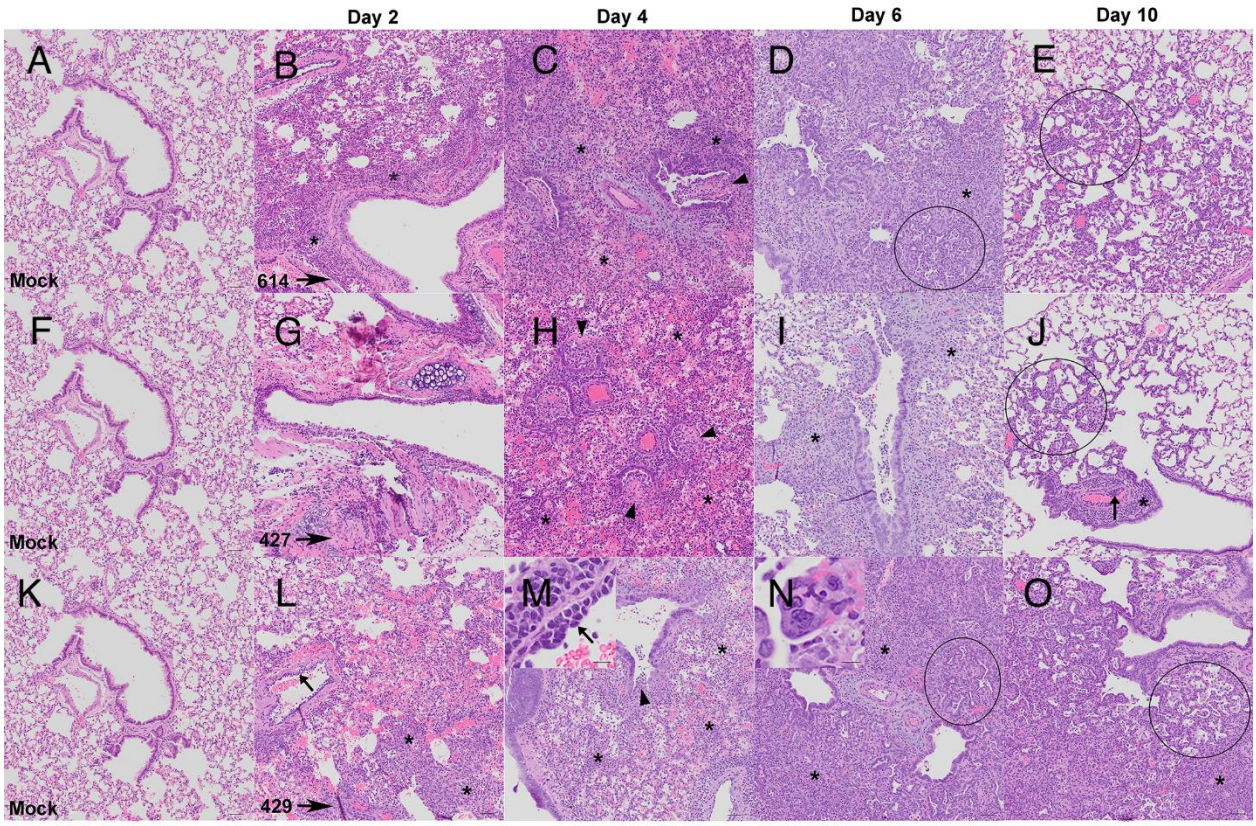



**Figure 3.3. The nature of lung histopathology in hamsters after intranasal inoculation with B.1 (614G), B.1.427 and B.1.429 is similar. A, F, K)** histology of normal lungs from uninfected hamsters. Top row: Histology of B.1 (614G) infection after **B)** 2 days PI, **C)** 4 days PI, **D)** 6 days PI, **E)** 10 days PI. Middle row: Histology of B.1.427 infection after **G)** 2 days PI, **H)** 4 days PI, **I)** 6 days PI, **J)** 10 days PI. Bottom row: Histology of B.1.429 infection after **L)** 2 days PI, **M)** 4 days PI, inset: and Perivascular cuffing with endothelium of a small vessel lifted off basal lamina by inflammatory infiltrate of lymphocytes and a few polymorphonuclear leukocytes (PMNs). **N)** 6 days PI, inset: multinucleate syncytial giant cell in bronchiolar epithelium. **O)** 10 days PI. Asterisks= mixed inflammatory infiltrate (lymphocytes, PMNs and macrophages); arrowheads= suppurative bronchiolitis with rupture of bronchiolar wall; arrows= endotheliitis; circles= foci of type II pneumocyte hyperplasia. Hematoxylin and eosin stain. Original magnification: 100x. Scale bars equal 50 µm, Inset scale bars equal 20 µm.

By day 4 PI, in all animals infected with all variants, bronchiolar and alveolar lesions had progressed to necro-suppurative bronchiolitis with loss of normal alveolar septal architecture and replacement by hemorrhage, edema, fibrin, necrotic debris, mixed inflammation, and frequent multinucleated syncytial cells (Figure 3.2 and 3.3: C, H, and M), affecting up to 50% of the pulmonary surface area (Figure 3.2 C, H, and M). Perivascular cuffing and endothelialitis remained prominent features, with mononuclear cells frequently extending from endothelium to adventitia in many small arteries (Figure 3.3 M, inset). Variable bronchiolar epithelial hyperplasia (characterized by epithelial cell piling up and increased mitotic figures) and

scattered type II pneumocyte hyperplasia were also noted, particularly in those animals inoculated with B.1.429 (Figure 3.3 M). In all animals infected with all variants, similar microscopic features, including necrotizing neutrophilic and histiocytic broncho-interstitial pneumonia with syncytial cells, perivascular cuffing, and endothelialitis, were observed at day 6 PI (Figures 3.2 and 3.3: D, I, and N). These lesions affected 25-50% of the pulmonary surface area in examined sections (Figure 3.2 D, I, and N). Reparative changes, including bronchiolar epithelial hyperplasia and type II pneumocyte hyperplasia, were also prevalent at day 6 PI (Figures 3.2 and 3.3: D, I, and N).

By day 10 PI, the lung pathology in all animals infected with all variants had dramatically decreased. In animals inoculated with B.1 (614G) and B.1.427, necrosis, neutrophilic inflammation and vascular lesions appeared largely resolved, with replacement by patchy foci of mononuclear alveolar septal inflammation with bronchiolar epithelial and type II pneumocyte hyperplasia (Figures 3.2 and 3.3: E, J, O). The affected surface area in the lungs of these animals ranged from 2-10% (Figure 3.2 E, J, O). However, the animals inoculated with the B.1.429 variant exhibited more severe and widespread pulmonary lesions at day 10 PI (Figure 3.3 O), with persistence of neutrophilic to histiocytic alveolar septal inflammation with scattered syncytial cells and occasional endothelialitis as well as reparative changes. The affected surface area ranged from 15-20% in this group (Figure 3.2 O).

**Intranasal inoculation of hamsters with B.1.427 results in similar distribution of virus in lungs compared to ancestral B.1 (614G) SARS-CoV-2, while B.1.429 infects the lung parenchyma more rapidly.** In-situ hybridization (ISH) was used to localize viral RNA (vRNA) to specific structures and cell types in the lung (Figure 3.4). The findings were similar in animals infected with either B.1 (614G) or B.1.427. At day 2 PI, bronchiolar epithelial cells were intensely labelled with infected cells extending along the entire length of main stem bronchi and smaller airways (Figure 3.4 A, E). In addition, rare focal areas of vRNA positive pneumocytes were found in the lung parenchyma. At day 4 PI in B.1 (614G) and B.1.427 animals, airway epithelial cells remained intensely labelled, with many of the infected cells detached from the basal lamina (Figure 3.4 B, F). However, most of the vRNA positive cells at day 4 were now found in the lung parenchyma, with type I and II pneumocytes and alveolar macrophages strongly positive (Figure 3.4B, F). In contrast, in the B.1.429 infected animals intense labeling of vRNA positive cells in the parenchyma and airways was already present at day 2 PI, and this persisted to day 4 PI (Figure 3.4 I, J). Of the 5-6 animals infected with each variant that were necropsied at day 6 PI, one animal from each group had a few vRNA positive cells in isolated foci in the lung parenchyma. The lungs from the remaining 4-5 animals in each group were negative (Figure 3.4 C, G, and K). At day 10 PI, vRNA+ cells were not found in the lungs of any of the animals (Figure 3.4 D, H, and L). Although B.1.429 disseminated to lung parenchyma more rapidly than B.1.427 or B.1 (614G), all 3 variants seemed to infect the same populations of cells in the lung: mainly airway epithelial cells and type I and type II pneumocytes (Figure 3.4). Alveolar macrophages were also labeled but this was likely to due to phagocytosis of infected cell debris rather than productive infection.

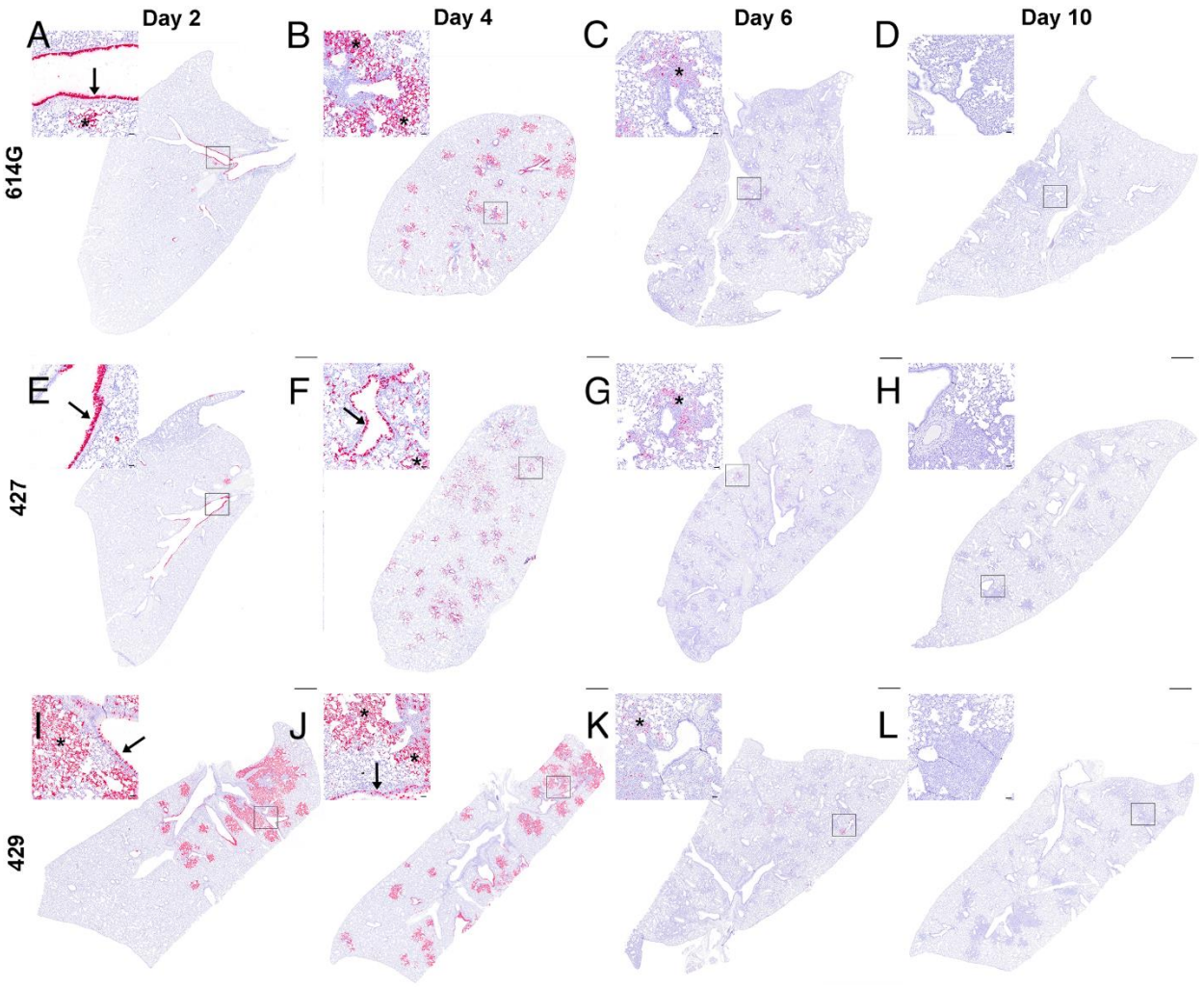



**Figure 3.4. Distribution of SARS-CoV-2 RNA+ cells in lungs of hamsters after intranasal inoculation with B.1 (614G), B.1.427 and B.1.429 by in-situ hybridization (ISH).** Sub-gross histology and magnified regions (inset denoted by black box) of ISH-labeled lung sections from hamsters infected with B.1 (614G) for **A)** 2 days PI, **B)** 4 days PI, **C)** 6 days PI and **D)** 10 days PI; or B.1.427 for **E)** 2 days PI, **F)** 4 days PI, **G)** 6 days PI and **H)** 10 days PI; or B.1.429 for **I)** 2 days PI, **J)** 4 days PI, **K)** 6 days PI and **L)** 10 days PI. Cells labeled by riboprobe in-situ hybridization stain red. Arrows= labeled bronchial/bronchiolar epithelial cells lining airways; asterisks= regions of lung parenchyma with labeled alveolar septal cells (type I/II pneumocytes and macrophages). Original magnification: 1x. Scale bars equal 1 mm. Inset scale bars equal 50 µm

**Intranasal inoculation of hamsters with B.1.429/427 results in similar sgRNA levels in lung and upper respiratory tract washes but sgRNA levels in oral swabs from B.1.429 infected animals were higher compared animals infected with to ancestral B.1 (614G) SARS-CoV-2.** In all the SARS-CoV-2 infected hamsters, the levels of sgRNA in daily oral swabs were highest at 1 or 2 days PI and then declined steadily to day 4 PI. However, the sgRNA levels were significantly higher in the oral swabs of B.1.429 animals compared to the B.1.427 or B.1 (614G) animals (Figure 3.5A). The levels of sgRNA in URT washes collected at necropsy were highest at day 2 PI

but had declined dramatically by day 10 PI (Figure 3.5B) in all animals and sgRNA levels were similar in all hamster groups (Figure 3.5B). The levels of infectious virus and sgRNA in the lungs of hamsters inoculated with all 3 viruses were very similar: high at days 2 and 4 PI but undetectable infectious virus and low sgDNA at days 6 and 10 PI (Figures 3.5C and D).

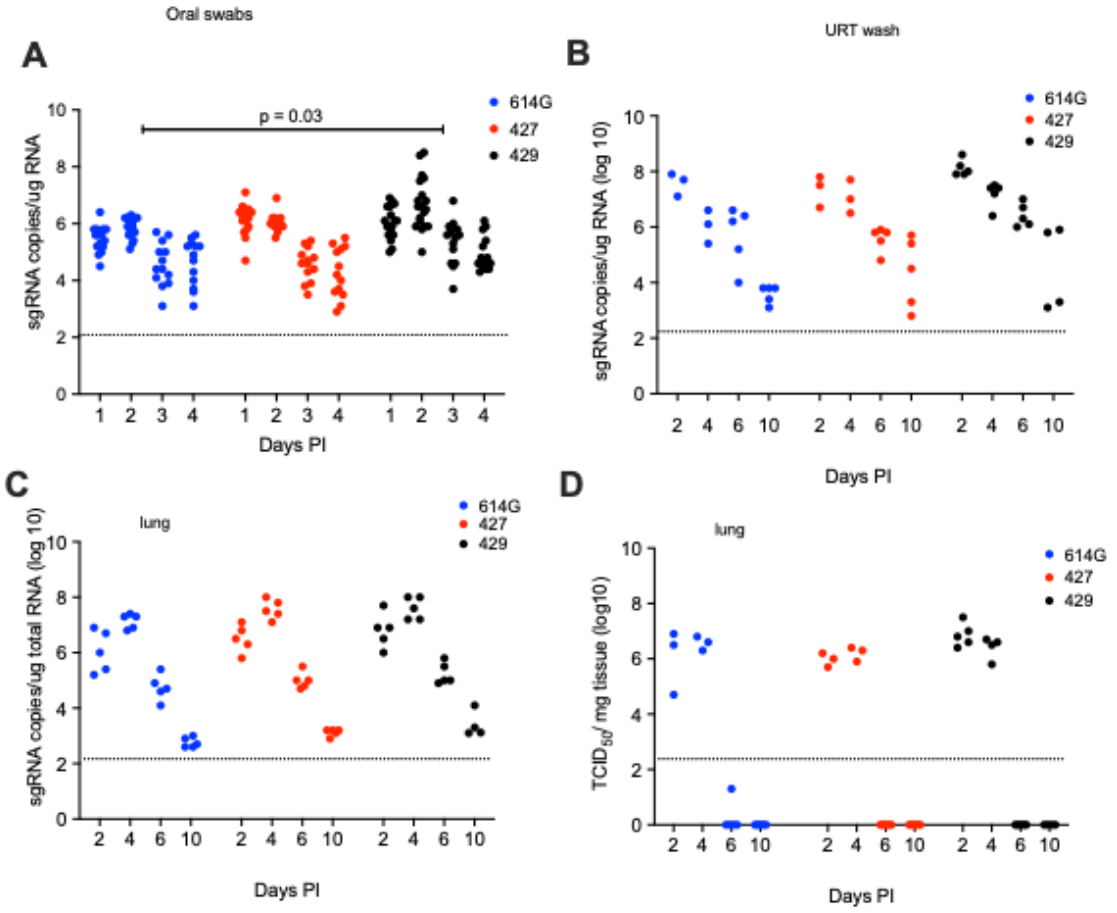



**Figure 3.5. Viral loads in hamsters after intranasal inoculation with B.1 (614G), B.1.427 or B.1.429.** **A)** sgRNA copies in oral swabs collected daily until day 4 or necropsy. Mean values from all groups were compared by fitting a mixed model, and a post-hoc multiple comparison test was used to compare the mean values of the B.1.427 or B.1.429 groups individually to the 614G group. **B)** sgRNA copies in upper respiratory tract (URT) washes collected at necropsy on 2, 4, 6 or days 10 PI. **D)** sgRNA copies in lungs collected at necropsy on 2, 4, 6 or days 10 PI. **D)** Infectious virus titers in lungs collected at necropsy on 2, 4, 6 or 10 days PI.

**Specific variants predominate in lungs and nasal cavity of hamsters after intranasal inoculation with a mixture of SARS-CoV-2 variants.** To determine if there is a relative fitness advantage among the circulating VOCs, hamsters were inoculated intranasally with a mixture of

viruses and the proportion of each inoculated virus in the lungs and nasal cavity was determined. In the first experiment, animals (Table S.3.1) were inoculated with 5000 PFU of SARS-CoV-2 that was either a 1:1 or 9: 1 mixture of B.1 (614G) and B.1.427 based on PFU. In hamsters inoculated with mixtures of 2 viruses, the level of sgRNA in the oral swabs were highest at day 1 then declined until day 4 PI (Supplemental Figure S.3.1 A) while sgRNA levels in lungs and URT were higher at day 2 PI than day 4 PI (Supplemental Figure S.3.1A, B and C). The sgRNA levels in the oral swabs, lungs and URT of hamsters infected with the 2 virus mixtures were very similar to animals inoculated with a single virus (Supplemental Figure S.3.1, Figure 3.5).

To determine if B.1 (614G) or B.1.427 had a competitive advantage over the other, RNA from the lungs and upper respiratory tract from the animals was sequenced to determine the proportion of each virus in the sample. In the URT and lung samples of the 1:1 inoculated animals, B.1.427 made up between 39-57% of the virus population at day 2 PI and 21-58% at day 4 PI (Figure 3.6A and B). In the lung samples of the 9:1 inoculated animals, B.1.427 made up about 10% of the virus population in the lungs at day 2 and 4 PI (Figure 3.6A), while in the URT, B.1.427 made up from 8% to 35% of the virus population at day 2 and 4 PI (Figure 3.6B). These results suggest that B.1.427 may have slight replicative advantage in the URT compared to B.1 (614G). However, there was no indication that B.1.427 had an enhanced ability to replicate in lungs compared to B.1 (614G).

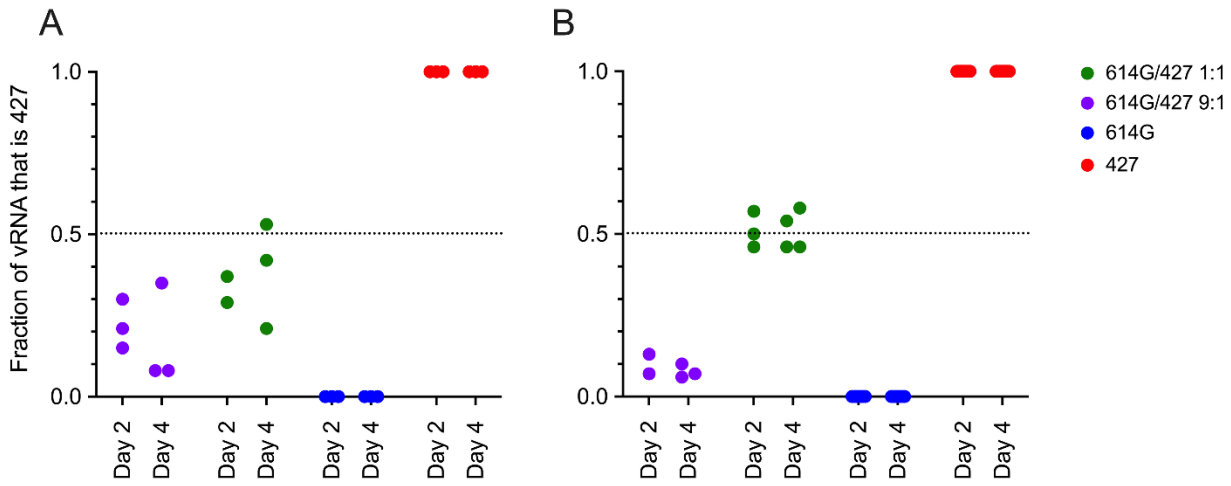



**Figure 3.6. sgRNA levels and the proportion of each virus in hamsters after intranasal inoculation with a 1:1 or 9:1 mixed inoculum of B.1 (614G) and B.1.427; and sgRNA levels in hamsters inoculated with a mixed inoculum of 7 SARS-CoV-2 variants: B.1 (614G), B.1.427, B.1.427, P.1, P.2, B.1.1.7 and B.1.351. A)** proportion of the vRNA in lungs collected at necropsy on 2 and 4 days PI that was B.1.427. **B)** proportion of the vRNA in URT washes collected at necropsy on 2, and 4 days PI that was B.1.427.

To simultaneously determine the relative fitness of a larger number of variants, in a third experiment, 10 animals (Table S.3.1) were inoculated with 5000 PFU of SARS-CoV-2 that was composed of an equal mixture, based on PFU, of 7 SARS-CoV-2 variants: ancestral B.1 (614G) [16], B.1.427 [5], B.1.429[5], P.1 [17], P.2 [17], B.1.1.7 [18] and B.1.351 [19]. The amplicon sequencing strategy named QUILLS (QUasispecies Identification of Low-Frequency Lineages of SARS-CoV-2) was used to identify relative frequencies of viral variants within a mixed population by sequencing of key single nucleotide mutations in the spike and orf1ab genes (see Methods). QUILLS analysis of the pure viral stocks used to generate the mixture revealed > 99.5% of the RNA sequences obtained from the stocks were identical to the published sequence of the respective VOC; analysis of mixture showed that each VOC comprised between 4% and 25% of the RNA in the mixed virus inoculum (Figure 3.7A), as expected based on PFU normalization. In the hamsters inoculated with this mixture of 7 viruses, the levels of sgRNA in the lungs, orophayrnx and URT were very high at days 2 and 4 PI Supplemental Figure S.3.1 and were similar to the levels found in animals inoculated with a single virus (Figure 3.5).

To determine if one or more of the 7 variants in the inoculum had a competitive advantage over the others, RNA from the lungs and upper respiratory tract from animals necropsied at day 2 PI (n=5) and day 4 P (n=5) was sequenced and the proportion of each virus in the samples was determined. In the day 2 lung samples, B.1 (614G), P.1 and epsilon (B.1.427/B.1.429) predominated (mean: 32.8%/ range: 0-84%, 38.8%/0-98% and 25.4%/1-45% respectively) with P.2, and 351 making up less than 2% of the vRNA (Figure 3.7D). On day 4, the lung vRNA was B.1(614G): 38.1%/11.2-51%, epsilon (B.1.427/ B.1.429) 38.2%/4-49%, P.1: 21.6%/0.1-47.2%, with B.1.1.7, P.2 and B.1.351 making up less than 2% of the vRNA (Figure 3.7E). Thus, in the lung, B.1 (614G), P1 and epsilon (B.1.427/ B.1.429) were the most frequent variants while B.1.1.7, B.1.351 and P.2 were only found at low levels.

In the day 2 PI URT washes, the vRNA was B.1 (614G): 35%/20-48%, P1: 28%/19.4-57%, epsilon (B.1.427/ B.1.429): 27.7%/14.1-49.9%, B.1.1.7: 8.8%/2-37.9%, with P2 and 351 making up less than 1% of the vRNA (Figure 3.7B). On day 4, the URT vRNA was B.1 (614G): 29.6%/0-70.2%, P.1: 33%/9.7-60%, epsilon (B.1.427/ B.1.429): 31.9%/14-63.3%, B.1.1.7: 5%/1-13%, with P.2 and B.1.351 making up less than 1% of the vRNA (Figure 3.7C). Thus, in the URT, B.1 (614G), epsilon (B.1.427/ B.1.429) and P.1 were the most frequent variants, B.1.1.7 was intermediate and B.1.351 and P.2 were infrequent. These results demonstrate that B.1, P.1 and epsilon (B.1.427/ B.1.429) have a competitive advantage over the other variants in the lung but that B.1.1.7 can compete with P.1 and epsilon (B.1.427/ B.1.429) in the URT.

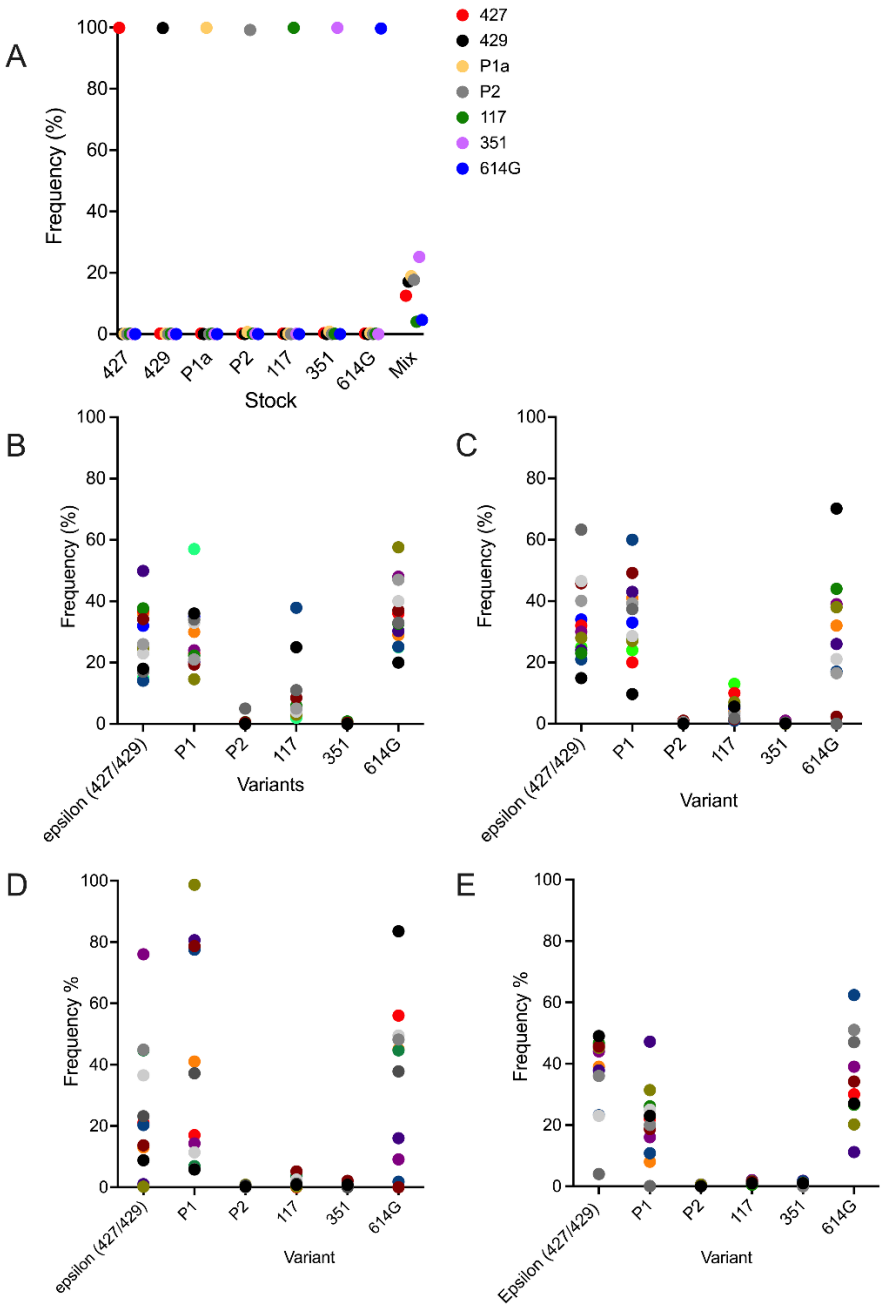



**Figure 3.7. Relative levels of SARS-CoV-2 variants in hamsters after intranasal inoculation with a mixed inoculum of 7 SARS-CoV-2 variants: B.1 (614G), B.1.427, B.1.429, P.1, P.2, B.1.1.7 and B.1.351. A)** Proportion of each variant RNA in the total vRNA of each virus in **(A)** stock and the mixed inoculum, in the URT washes of hamsters at **(B)** day 2 PI or **(C)** day 4 PI, in the lungs of hamsters at **(D)** day 2 PI or **(E)** day 4 PI. In all panels, each dot represents the frequency of that variant in one sample. Each animal is denoted by a color.

**Prior Infection with B.1 (614G) protects hamsters from subsequent challenge with B.1.427/429.** To confirm protection from homologous challenge, hamsters (Table S.3.1) were inoculated intranasally with 5000 PFU B.1 (614G) and then were rechallenged with 5000 PFU B.1 (614G) 21 days later (Figure 3.8A); another group of hamsters (Table S.3.1) was infected with B.1.427 and rechallenged with B.1.427 21 days later (Figure 3.8B). To determine if B.1.427 and B1.429 are susceptible to the immune responses elicited by prior infection with B.1 (614G), hamsters (Table S.3.1) were inoculated intranasally with 5000 PFU of B.1 (614G) and then were challenged 21 days later by intranasal inoculation of 5000 PFU of B1.427 or B1.429. To document infection and to determine the levels of vRNA at time of challenge, five animals in each group were necropsied at day 2 and day 21 respectively (Table S.3.1). Rechallenged animals were necropsied on day 2 days after re-challenge (day 23) (Table S.3.1). Viral titer and sgRNA levels in lungs were determined for all groups and timepoints (Figure 3.8).

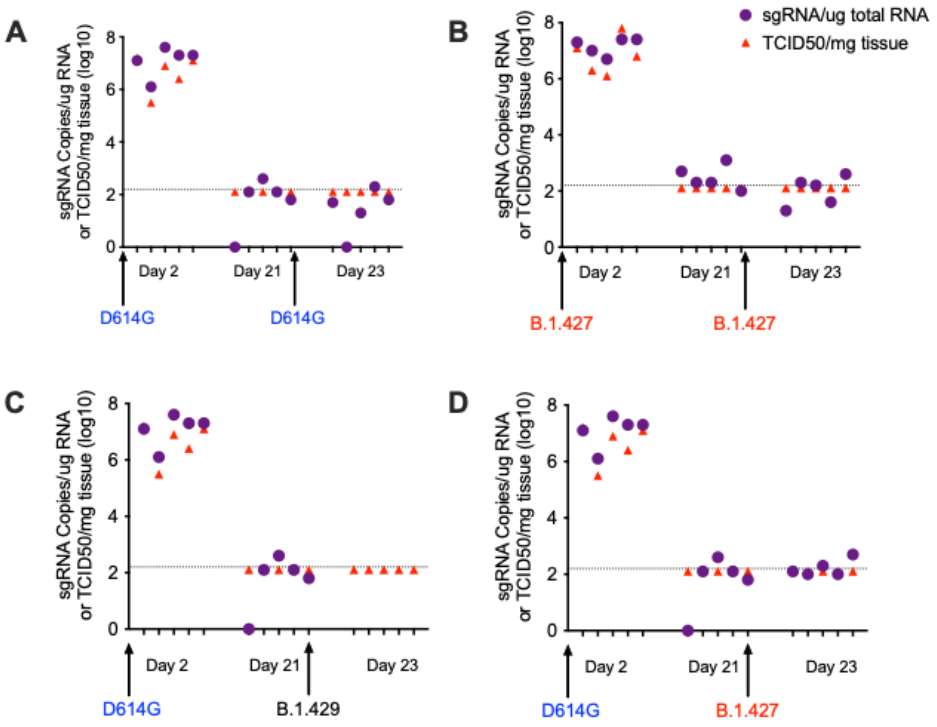



**Figure 3.8. Prior infection with B.1 (614G) protects hamsters from subsequent challenge with B.1.427 or B.1.429. A) s**gRNA levels and infectious virus titer in hamster infected with B.1 (614G) and then challenged 21 days later with homologous B.1 (614G). **B)** sgRNA levels and infectious virus titer in hamster infected with B.1.427 and then challenged 21 days later with homologous B.1.427. **C)** sgRNA levels and infectious virus titer in hamster infected with B.1 (614G) and then challenged 21 days later with heterologous B.1.429. **C)** sgRNA levels and

infectious virus titer in hamster infected with B.1 (614G) and then challenged 21 days later with heterologous B.1.427.

All animals had high levels of sgRNA and infectious virus in lungs at day 2 PI, but no infectious virus and only very low levels of sgRNA were detected in animals at day 21 PI (Figure 3.8), confirming that the animals had been infected by the initial inoculum and then cleared the infection. Two days after re-challenge (day 23 PI) neither viable virus nor detectable sgRNA were found in the lungs of any of the animals (Figure 3.8). Thus, prior infection with ancestral B.1 (614G) protects hamsters from challenge 21 days later with either B.1.427 or B.1.429, with protection defined as no virus replication in lungs.

**The efficiency of airborne transmission between hamsters infected with (B.1.427/429) and B.1 (614G) is similar.** To determine if the airborne transmission of B.1.427 and B1.429 between hamsters is more efficient than B.1 (614G) airborne transmission, four groups of eight "donor" hamsters (Table S.3.1) were inoculated intranasally with $10^4$ PFU of either B.1 (614G), A.1 (WA-1), B.1.427 or B.1.429 (Figure 3.9). Six to 8 hours after donor inoculation, naïve "sentinel" animals were added to one end of the cage separated from the donor animals by a barrier that prevents large particles but allows smaller particles to pass between the co-housed animals [20]. Oral swabs were collected at day 1 PI from donor animals that were later necropsied at Day 7 or 8 PI. Sentinel animals were monitored for virus in oral swabs collected for up to 14 days after exposure. High levels of sgRNA were detected in the oral swabs of all the donor animals at day 1 PI confirming that they were infected (Figure 3.9A). It is worth noting that the day 1 PI sgRNA levels in the swabs of B.1.429 infected animals were the highest and the difference compared to WA-1 infected animals was significant ($p= 0.0146$ mixed effects analysis and post hoc test, Figure 3.9A). Of the eight sentinels exposed to the B.1.427 donors, all 8 were infected by 2 days post-exposure (PE). By comparison, 100% of B.1 (614G) sentinels were infected by 3 days PE and 100% of WA-1 sentinels were infected by 5 days PE (Figure 3.9B). Thus, B.1.427 was transmitted marginally more rapidly than WA-1 and B.1 (614G). In contrast among the B.1.429 sentinels, 7 out of 9 animals were infected by 3 days PE and 8 of 9 animals were infected by 5 days PE (Figure 3.9B). Thus, B.1.427 transmits between hamsters marginally more efficiently than B.1 (614G) and WA-1, while B.1.429 transmits marginally less efficiently than B.1 (614G) and WA-1. Taken together, these data suggest that airborne transmission of epsilon (B.1.427/429) and B.1 (614G) between hamsters is similar.

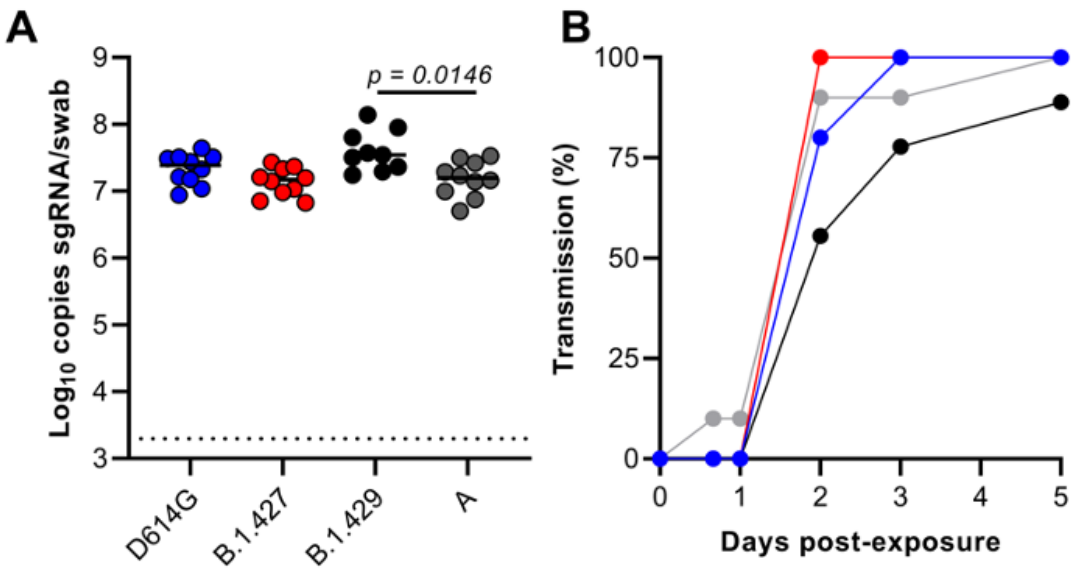



**Figure 3.9. Relative efficiency of B.1 (614G), B.1.427 and B.1.429 airborne hamster to hamster transmission. A)** sg RNA levels in oral swabs collected from donors 1 day after intranasal inoculation. Mean values from all groups were compared by fitting a mixed model, and a post-hoc multiple comparison test was used to compare the mean values of the B.1.429 group to the other 3 groups individually. **B)** the percent of sentinel animals that are infected each day based on detection of sgRNA in oral swabs collected at least daily after co-housing.

**Discussion**

The SARS-CoV-2 epsilon variant is comprised of 2 separate lineages, B.1.427 and B.1.429, with each lineage rising in parallel in California and other western states [5]. The variant is predicted to have emerged in California in May 2020 and increased in frequency from 0% to >50% from September 2020 to January 2021. The B.1.427/B.1.429 variant is no longer the predominant circulating variant in California, as it was replaced first by the B.1.1.7 (alpha) variant, which has since been replaced by the B.1.617.2 (delta) variant. The SARS-CoV-2 B.1.427/B.1.429 (epsilon) variant has a characteristic triad of spike protein mutations (S13I, W152C, and L452R) [5]. Epidemiologic and in-vitro studies found that the variant is approximately 20% more transmissible with 2-fold increased shedding in patients compared to ancestral B.1 (614G) [5] and that the spike L452R mutation conferring increased the infectivity of pseudoviruses in vitro [5]. It was not clear if the B.1.427/B.1.429 variants caused more severe disease; however, as the frequency of infection with the B.1.427/B.1.429 variants increased, the number of cases increased [5], followed by an increase in COVID-19 associated hospitalizations and deaths

(https://covid19.ca.gov/state-dashboard/). This study demonstrates that, based on differences in weight loss, the SARS-CoV-2 epsilon variant (B.1.429 and B.1427) is more virulent than ancestral B.1 (614G) SARS-CoV-2; and B.1.429 is more virulent than B.1.427 in Syrian hamsters. The more rapid dissemination of virus from the airways to the alveoli in the lungs and higher levels of virus replication in the oropharynx of B.1.429 infected animals provide a biologically plausible explanation for the higher virulence of this L452R carrying variant.

The significantly higher sgRNA levels in the oral swabs collected daily over the first 4 days of B.1.429 infection suggests that this variant has enhanced fitness in the oropharynx of hamsters compared to B.1 (614G) or B.1.427. This finding is consistent with the finding that there is a 2-fold increase in median viral loads in nasal swabs of patients infected with B.1.427/B.1.429 SARS-CoV-2 (epsilon) compared to patients infected with ancestral B.1 (614G) [5]. However, it is important to note that the levels of sgRNA in the lungs of animals infected with all three viruses were similar. Although not statistically significant, it should also be noted that the sgRNA levels in the B.1.429 infected animals were higher at all time points compared to levels in B.1 and B.1.427 infected animals (Figure 3.5B). The inability to detect a significant difference in sgRNA levels in URT washes collected at necropsy is likely due to the fact only 3-5 URT wash samples were collected from each group of hamsters on days 2 and 4 PI, while 16-19 oral swab samples were collected daily from each group of hamsters on days 1-4 PI. The URT-specific enhanced fitness of B.1.429 could be explained by a higher density of susceptible and permissive cells for B.1.429 in the URT compared to the lung or by the presence of mutations in B.1.429 that makes it more adapted for replication in the URT. Prior studies have suggested that the L452R mutation may increase infectivity because it stabilizes the interaction between the spike protein and its human ACE2 receptor [21] [22]. In-vitro studies found that the L452R mutation that defines the epsilon VOC enhances pseudovirus infection of 293T cells and lung organoids [5]. Our finding in hamsters of higher replication levels of B.1.429 in the URT, but not the lung, compared to the ancestral B.1 (614G) variant extends these in-vitro findings to intact animals. Notably, our competition experiments demonstrated that the L452R containing B.1.427 and B.1.429 variants outcompeted many other variants that do not contain L452R (B.1.1.7, P.2, B.1.351) in the lungs and URT. The exceptions were B.1 (614G) and the P1 variant, which replicated to levels that were similar to (epsilon) B.1.427/B.1.429 in both lungs and URT; and the B.1.1.7 variant that was able to compete with B.1 (614G), B.1.427/429 and P.1 in the URT but not the lung. Our results are consistent with a previous report that the B.1.1.7 variant replicates to higher levels in the nose of Syrian hamsters than the ancestral B.1 variant [23]. Both the P.1 and B.1.1.7 variants carry the N501Y-mutation that also enhances infectivity in-vitro [22] and this may explain why they can successfully compete with the L452R variants in the nose of hamsters. It is also possible to conclude from these results that the relative fitness of different variants depends, at least to some extent, on the anatomic site of the infection.

The QUILLS strategy to identify relative frequencies of viral variants within a mixed population by sequencing of key single nucleotide mutations has limitations in that only variants with known mutations can be identified. All the variants used in the mixed inoculum experiments in this study, have lineage-defining mutations in spike and orf1ab on the backbone of ancestral B.1 (614G) and these 6 variants are unambiguously identified in the infected animals by

QUILLS. However, the variant identified as B.1(614G) using QUILLS is an aggregate of all variants carrying 614G that cannot be otherwise be assigned to one of the other 6 variants in the inoculum. This would include novel variants arising from the inoculum B.1(614G) and revertants that may arise in each VOC quasispecies. Because of this, the relative frequency assigned to the ancestral B.1(614G) is less reliable than the frequencies of the other 6 variants that are based on positively identified sequences in the samples. Similarly, a single point mutation in orf1ab, that can arise or revert spontaneously, distinguishes B.1.427 and B.1.429. This makes it difficult to unambiguously identify B.1.429 and B.1.427 in mixtures and thus are reported the results as the frequency of the "epsilon", the aggregate of the B.1.429 and B.1.427 frequencies.

As previously reported with ancestral B.1 and other VOC [13,23,24], in this study intranasal inoculation of hamsters with the SARS-CoV-2 B.1 (614G) or epsilon variants (B.1.247/B.1.249) induced progressive moderate to severe broncho-interstitial pneumonia with vasculitis, beginning as early as day 2 PI. By day 10 PI, lesions were largely resolved, with only residual mononuclear interstitial inflammation and reparative changes. While the pulmonary pathology in hamsters largely mirrored that of humans, unlike humans that die of COVID [25-28], thrombosis, microangiopathy or necrotic vessel walls were not observed in any of the hamsters. However, all hamsters recover from the SARS-CoV-2 infection, and thus do not model fatal COVID disease. This difference makes the comparison of lung pathology of hamsters and humans imperfect. While the nature and distribution of the lesions were similar with all variants, by analyzing histologic changes frequently (day 2, 4, 6 and 10 PI), differences are detectable in the timing of the onset and resolution of the lesions in animals infected with different variants. Hamsters infected with B.1(614G) and B.1.427 tended to have more severe vascular changes than animals infected with B.1.429, however this increased vascular disease was not associated with more weight loss or higher levels of viral replication and may be an incidental finding. Studies, like those performed here, employing sequential analysis of pathologic changes in larger numbers of inoculated hamsters can detect differences in the time course of disease between SARS-CoV-2 variants. Studies that examine one or two timepoints PI are less likely to be informative. In fact, although a study comparing B.1.1.7 and B.1.351 infection in female Syrian hamsters found no major differences in lung histology, only one time point after infection, day 4 PI, was examined [24]. Even at this single time point however, compared to ancestral B.1 variants, the proinflammatory cytokine response was more intense in lungs of B.1.1.7 infected hamsters [24]. This discordance between the relative intensity of inflammation and the relative levels of inflammatory mediators reported demonstrates that sequential examination of both parameters is needed to determine how the lung inflammatory cell infiltrates drive the differential expression of inflammatory cytokines.

The ISH results demonstrated that B.1.427 and B.1 (614G) SARS-CoV-2 variants disseminate from the airways to the lung parenchyma at between days 2 and 4 PI, at least 24 hours after B.1.429 has begun replicating in alveoli. The faster observed dissemination of virus to alveoli in B.1.429 is consistent with the more rapid onset of histologic changes in the lung. The combination of ISH and histopathologic examination of lungs collected at frequent intervals

post-inoculation seems to be a good strategy to detect differences in SARS-CoV-2 VOCs virulence.

An ongoing concern is the extent to which newly emerging variants can evade preexisting immunity that was generated from infections with ancestral SARS-CoV-2 variants. These concerns have been validated by the P.1 epidemics in Manaus, Brazil that occurred despite seropositivity rates of up to 76% prior to P.1 emergence [17]. The result of our serial infection experiments clearly demonstrate that immune responses present 21 days after primary infection by ancestral B.1 (614G) infection protect hamsters from challenge with both epsilon variants (B.1.427/B.1.429). In fact, virus replication or infectious virus was undetectable in the lungs of any of the previously infected hamsters 2 days after the heterologous challenge. Thus, the immunity induced by the prior B.1 (614G) infection completely protected the lung from the epsilon infections and thus the animal from significant disease. Similarly, strong protection is found in hamsters infected with B.1 and rechallenged with B.1.1.7 [23]. The levels of virus replication in the URT after heterologous challenge, however, were not assessed, thus the degree to which prior infection affects replication in the URT, and therefore transmission between hamsters, is unknown. In addition, as the rechallenge occurred at day 21 PI, mature antiviral immune responses are expected to be present in blood and secretions [12,15], however, the immune mechanism associated with the heterologous protection was not characterized.

Epidemiologic studies led to the estimate that the epsilon (B.1.427/B.1.429) variant is 20% more transmissible than the ancestral B.1 (614G) and this was attributed to higher viral loads in the URT [5] . However, the hamster transmission studies reported here failed to show a consistent or large difference in transmission efficiency, between the epsilon (B.1.427/ B.1.429) variant and the ancestral B.1 (614G) variant, despite the higher viral load in the URT of B.1.429 infected hamsters. The inability to model increased airborne transmission of the epsilon (B.1.427/ B.1.429) variant was likely due to a combination of the experimental design and the relatively small differences in human transmission efficiency between B.1 (614G) and epsilon (B.1.427/ B.1.429). Differences in hamster transmission would likely be apparent with a variant that was at least 50% more transmissible than the ancestral variant and/or if the sentinel animals were exposed to donor animals when virus shedding is no longer at its peak, 2-3 days after they were inoculated. This may detect differences in transmission based on duration of URT shedding, while the 24 hour PI donor exposure approach attempts to detect differences due to the levels of URT shedding at the peak of virus replication.

As novel SARS-CoV-2 variants continue to emerge, it is critical that their pathogenic potential be rapidly assessed in animal models. The Syrian hamster model proved useful to detect differences in virulence of ancestral B.1 and the B.1.427 and B.1.429 epsilon VOCs by comparing body weight changes over 10 days. The timing and severity of lung pathology also distinguished the variants and correlated with the timing of virus dissemination into deep lung tissues based on ISH labelling. Further, the multi-virus in-vivo competition experiments provided insight into the relative fitness of the different SARS-CoV-2 variants and revealed that the anatomic site (lung vs. URT) can affect the relative fitness of the variants. Clinical and epidemiologic studies

are needed to confirm that the increased virulence and high relative fitness of the epsilon (427/429) variant in Syrian hamsters is mirrored in human infections.

## Materials and Methods

**Ethics statement.** Approval of all animal experiments was obtained from the Institutional Animal Care and Use Committee of UC Davis (Protocol # 22233, approved 3/18/21), UC Berkeley (AUP-2020-04-13242), or the Rocky Mountain Laboratories. Experiments were performed following the guidelines and basic principles in the United States Public Health Service Policy on Humane Care and Use of Laboratory Animals and the Guide for the Care and Use of Laboratory Animals. Work with infectious SARS-CoV-2 variants under BSL3 conditions was approved by the Institutional Biosafety Committees (IBC). The male and female Syrian Hamsters used at UCD and UCB were 7-9 weeks old, and they were purchased from Charles River Inc. The male and female Syrian Hamsters used for the airborne transmission experiments at RML were 4-6 weeks old, and they were purchased from ENVIGO Inc. Inactivation and removal of samples from high containment was performed per IBC-approved standard operating procedures.

**Viruses and cells.** SARS-CoV-2 variant variants ancestral B.1 (614G), B.1.427, B.1.429, B.1.1.7 were isolated from patient swabs by CDPH, Richmond CA, and P.2 and 351 were isolated from patient swabs at Stanford University, Stanford CA, USA. The “ancestral B.1 (614G)” SARS-CoV-2 variant had no defining mutations other than the B.1 (614G) mutation in spike. The P.1 variant was expanded by CDPH from a sample originally obtained from BEI Resources to produce the P1a stock. SARS-CoV-2 variant nCoV-WA1-2020 (lineage A) was provided by CDC, Atlanta, USA. Virus propagation was performed in Vero-86 cells in Dulbecco's Modified Eagle Medium (DMEM) supplemented with 5% fetal bovine serum (FBS), 2 mM L-glutamine, 100 U/mL penicillin and 100 g/mL streptomycin. No contaminants were detected in any of the virus stocks except in the P.1 stock in which mycoplasma was detected. There is no indication that this contamination affected the experimental outcomes. All virus stocks except P1a were the second passage of the patient isolate on Vero cells, the original isolation being the first passage on Vero cells. The virus stocks were deep sequenced and the RNA sequences of all the virus stocks used were 100% identical to the corresponding variant sequences deposited in GenBank.

**Hamster inoculations.** For experimental inoculations, 7-9 week old Syrian hamsters (Charles River) were infected intranasally with a total dose of approximately 5000 PFU of SARS-CoV-2 suspended in 50 µL sterile DMEM. This virus dose was chosen as it reliably infected hamsters in a series of preliminary experiments. For experiments in which mixtures of viruses were used, the dose of all variants was approximately equal (< 10-fold difference) and the total virus dose was approximately 5000 PFU. The airborne transmission experiments are described below.

**Infectious virus titer determination by $TCID_{50}$ assay.** Virus titer in lung was determined by a $TCID_{50}$ assay in Vero E6 cells. Briefly, 10,000 cells per well were plated in 96-well plates and cultured for 24 hours at 37 °C/5% $CO_2$. Lung tissue collected from hamsters was weighed and homogenized by bead beating. Homogenates were serial 10-fold diluted in Vero E6 growth

medium and added to Vero E6 cells. Cells were observed for cytopathic effect for 5 days. $TCID_{50}$ results were calculated using the Spearman and Kärber method (LOD 200 $TCID_{50}$/mL) and normalized by lung tissue mass.

**qPCR for sub-genomic RNA quantitation.** Quantitative real-time PCR assays were developed for detection of full-length genomic vRNA (gRNA), sub-genomic vRNA (sgRNA), and total vRNA. Upper respiratory tract washes and oral swabs were lysed in Trizol LS in BSL-3 and RNA was extracted from the aqueous phase in BSL-2. RNeasy mini kits (Qiagen) were used to purify the extracted RNA. Following DNAse treatment (ezDNAse; Invitrogen), complementary DNA was generated using superscript IV reverse transcriptase (ThermoFisher) in the presence of RNAseOUT (Invitrogen). A portion of this reaction was mixed with QuantiTect Probe PCR master mix and optimized concentrations of gene specific primers. All reactions were run on a Quantstudio 12K Flex real-time cycler (Applied Biosystems). sgRNA was quantified using primers sgLeadSARSCoV2_F (CGATCTCTTGTAGATCTGTTCTC) and wtN_R4 (GGTGAACCAAGACGCAGTAT), with probe wtN_P4 (/56-FAM/TAACCAGAA/ZEN/TGGAGAACGCAGTGGG/3IABkFQ/). Standard curves generated from PCR amplicons of the qPCR targets were used to establish line equations to determine RNA copies/mL of sample.

**Histopathology.** Histopathology preparation and analysis was performed at the Department of Pathology, Microbiology and Immunology, School of Veterinary Medicine, University of California Davis. At necropsy, lung was inflated with 10% buffered formalin (Thermo Fisher) and hamster tissues were fixed for 48 hours at room temperature in a 10-fold volume of 10% buffered formalin. Tissues were embedded in paraffin, thin-sectioned (4µm) and stained routinely with hematoxylin and eosin (H&E). H&E slides were scanned to 40x magnification by whole-slide image technique using an Aperio slide scanner with a magnification doubler and a resolution of 0.25 µm/pixel. Image files were uploaded on a Leica hosted web-based site and a board certified veterinary anatomic pathologist at UC Davis blindly evaluated sections for SARS-CoV-2 induced histologic lesions. For semi-quantitative assessment of lung inflammation, the pathologist estimated the area of inflamed tissue (visible to the naked eye at subgross magnification) as a percentage of the total surface area of the lung section. Each section of lung was further scored as described in Supplementary Table S.3.1.

**In situ hybridization (ISH).** ISH was performed at the Department of Pathology, Microbiology and Immunology, School of Veterinary Medicine, University of California Davis. RNAscope® ISH was performed according to the manufacturer's protocol (Document Number 322452-USM and 322360-USM, ACD) with modifications. Briefly, RNAscope 2.5 HD Red Detection Kit (ACD) and RNAscope Probe - V-nCoV2019-S (cat# 848561, ACD) was used in the ISH assay. At each run of the ISH, RNAscope® Negative Control Probe – DapB (cat# 310043) and tissues from a SARS-CoV-2 uninfected animal hybridized with the SARS-CoV-2 probes served as negative controls. RNAscope® Probe - Mau-Ppib (cat# 890851, ACD) was used as a positive control for RNA quality and constancy of the ISH assay. Four-micron deparaffinized paraffin sections were pretreated with 1x Target Retrieval Buffer at $100^0$C for 15 minutes and RNAscope Protease Plus at 40 $^0$C for 30 minutes before hybridization at $40^0$C for 2 hours. A cascade of signal amplification was

carried out after hybridization. The signal was detected using a Fast Red solution for 10 minutes at room temperature. Slides were counterstained with hematoxylin, dehydrated, cover-slipped, and visualized by using a bright field microscope.

**Virus genome sequencing and Quasispecies identification of low-frequency lineages of SARS-CoV-2 (QUILLS)**. The amplicon strategy named QUILLS (QUasispecies Identification of Low-Frequency Lineages of SARS-CoV2) was developed and performed in the laboratory of Charles Y. Chiu at the University of California at San Francisco. QUILLS is a method by which all of the major circulating variants of concern (VOCs) and variants of interest (VOIs) could be identified on the basis of lineage-defining mutations in the SARS-CoV-2 spike and orf1b genes (Supplementary Figure S.3.1). Five pairs of forward and reverse primers (Table S.3.1, "QUILLS primer set") were designed to span the nucleotide sites associated with the spike S13, W152, K417, L452, E484, N501, A570, D614, H665, P681, T1027, and V1176 and orf1b P976 and D1183 positions. Thus, these primers were designed to target mutations that would be able to discriminate between all VOCs and nearly all VOIs in a mixed population.

Extracted RNA was diluted 1:3, and 7 microliters of diluted material were used for first strand cDNA synthesis using ProtoScript® II First Strand cDNA Synthesis Kit (New England Biolabs #E6560) with random hexamers and following manufacturer's instructions. PCR amplification was performed using the QUILLS primer set and Q5® High-Fidelity DNA Polymerase (NEB #M0491) as follows: 15.4 µl of water, 5 µl of Q5 reaction buffer, 0.5 µl of dNTPS (NEB N0447S), 0.25 µl of enzyme and 1.35 µl of primer for each pool (pool 1 and pool 2). Reactions were incubated at 98 °C for 30s, 35 cycles of 98 °C for 15s and 65 °C for 5m, 4 °C until use. Amplification product was bead washed with .8X CleanNGS Beads (CNGS-0500), DNA concentration was measured with qubit and all samples were normalized to 60 ng to avoid contamination. Libraries were prepared using NEBNext® Ultra™ II DNA Library Prep Kit for Illumina® (NEB #E7645L) following manufacturer's instructions and NEB Next Multiplex Oligos for Illumina (96 Index Primers, NEB #E6609) for multiplexing. Final concentration was measured with qubit and final libraries were pooled for sequencing in a concentration between 20 and 40 ng. Final pool was diluted to 6.5 picomolar and spiked with 10% PhiX. MiSeq Reagent Kit v2 (300-cycles single-end) was used for sequencing on the Illumina MiSeq (Illumina MS-102-2002) following manufacturer's specifications.

Raw FASTQ sequences were preprocessed using an in-house computational pipeline that is part of the SURPI software package [29,30]. The preprocessing step consisted of trimming low-quality and adapter sequences using cutadapt [31], retaining reads of trimmed length >75 bp, and then removing low-complexity sequences using the DUST algorithm in PrinSeq [32]. After filtering the preprocessed dataset for SARS-CoV-2-specific viral reads using the nucleotide BLAST algorithm with an e-value threshold cutoff of $10^{-8}$, lineage-specific mutation single nucleotide polymorphisms (SNPs) were identified and counted using a custom in-house computational script. The relative proportions of each SARS-CoV-2 variant in the mixture were estimated by manual analysis of the mutational frequencies at each of the lineage-defining SNPs.

**Airborne Transmission experiments.** The airborne transmission experiments were performed at the Rocky Mountain Laboratories, NIAID, NIH as previously described [33]. Hamsters were co-housed (1:1) in specially designed cages with a perforated plastic divider dividing the living space in half, preventing direct contact between animals and movement of bedding material (alpha-dri bedding). Donor hamsters were infected intranasally with $10^4$ PFU of the different SARS-CoV-2 variants. This virus dose was chosen because it has been used with success in previously published studies [33]. Sentinel hamsters were placed on the other side of a divider 6-8 hours later. Sentinel hamsters received an oropharyngeal swab on 16 hours post exposure (PE), 24 hours PE, 2, 3, 5, 7, 10, and 14 days PE. Donors received an oropharyngeal swab 1 day post inoculation. Donors were euthanized at 7 or 8 days PI, sentinels were followed until 14 days PE. Experiments were performed with cages placed into a standard rodent cage rack, under normal airflow conditions. Sentinels were placed downstream of air flow.

Hamsters were weighed daily, and oropharyngeal (OP) swabs were taken daily until day 7 and then thrice a week. OP swabs were collected in 1 mL DMEM with 200 U/mL penicillin and 200 µg/mL streptomycin. Then, 140 µL was utilized for RNA extraction using the QIAamp Viral RNA Kit (Qiagen) using QIAcube HT automated system (Qiagen) according to the manufacturer's instructions with an elution volume of 150 µL. Sub-genomic (sg) viral RNA and genomic (g) was detected by qRT-PCR [34,35]. Five µL RNA was tested with TaqManTM Fast Virus One-Step Master Mix (Applied Biosystems) using QuantStudio 6 Flex Real-Time PCR System (Applied Biosystems) according to instructions of the manufacturer. Ten-fold dilutions of SARS-CoV-2 standards with known copy numbers were used to construct a standard curve and calculate copy numbers/ml.

**Statistical analysis**. Because the number of hamsters in each animal group was not uniform, mean values from all groups were compared mixed effects analysis which compares data by fitting a mixed model, rather than by using a one-way ANOVA. A post-hoc multiple comparison test was used to compare the mean values of the B.1.427 or B.1.429 groups individually to the other groups. Graph Pad Prism 9.0 (San Diego, CA was used for the analysis.

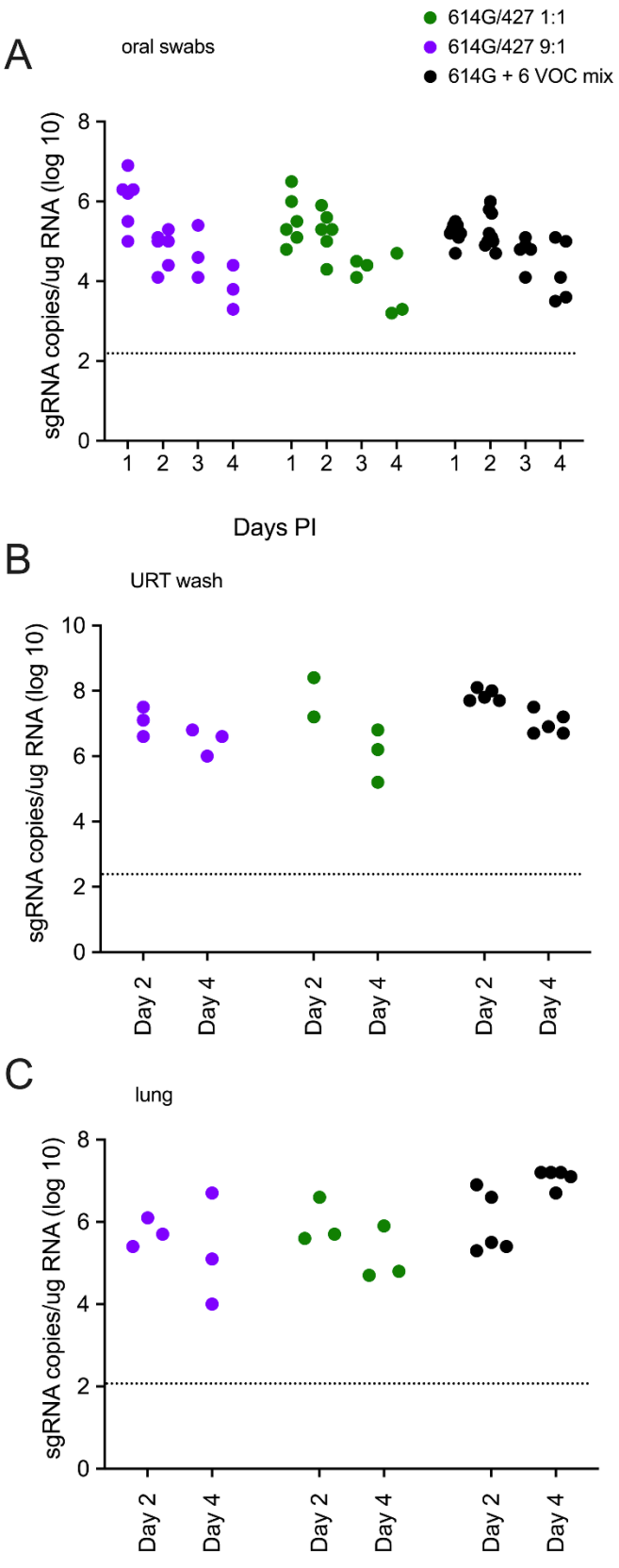
**Acknowledgements**

We thank M. Ott, M. Busch, J. Derisi and D. Wadford and other members of the NorCal SARS-CoV-2 Variant Assessment Group for helpful discussions and K. Keel for assistance with slide scanning. This work was supported by Intramural funding from the Center for Immunology and Infectious Diseases, UC Davis and NIH/R01-AI118590 to C.J. Miller; Fast Grants (part of Emergent Ventures at George Mason University) to S. Stanley; the Intramural Research Program of the National Institute of Allergy and Infectious Diseases, National Institutes of Health (1ZIAAI001179-01) to RML, a T32 AI007502-23 to A. Rustagi, NIH/R33-AI129455 and the US Centers for Disease Control and Prevention (contract 75D30121C10991) to C.Y. Chiu. The funders had no role in study design, data collection and analysis, decision to publish, or preparation of the manuscript.

**Supplemental Information**

**Table S.3.1: Summary of the experiments.**

| Experiment | virus dose (PFU) | Virus | Oral swabs (Day PI) | Necropsy time points and animal numbers (Day PI/hamster number) | Figures |
|---|---|---|---|---|---|
| Pathogenesis/virulence | 5000 | B.1(614G) | d1, d2, d3, d4 | d2/6, d4/6, d6/6, d10/5 | 3.1,3.2, 3.3, 3.4, 3.5 |
| Pathogenesis/virulence | 5000 | B.1.427 | d1, d2, d3, d4 | d2/6, d4/9, d6/6, d10/6 | 3.1,3.2, 3.3, 3.4, 3.5 |
| Pathogenesis/virulence | 5000 | B.1.429 | d1, d2, d3, d4 | d2/4, d4/5, d6/5, d10/4 | 3.1,3.2, 3.3, 3.4, 3.5 |
| | | | | | |
| Fitness/competition | 5000 | B.1.(614G) /B.1.427 - 1:1 | d1, d2, d3, d4 | d2/3, d4/3 | 3.6, Sup. Figure S.3.1 |
| Fitness/competition | 5000 | B.1.(614G) /B.1.427 - 1:9 | d1, d2, d3, d4 | d2/3, d4/3 | 3.6,, Sup. Figure S.3.1 |
| Fitness/competition | 5000 | B.1.(614G)/B.1.427/B.1.429/P.1/P.2/B.1.1.1.7/ B.1.351 | d1, d2, d3, d4 | d2/5, d4/5 | 3.6, 3.7, Sup. Figure S.3.1 |
| | | | | | |
| Prior infection/cross protection | 5000 | B.1(614G) then at 21 days PI B.1.(614G) | - | d2/5, d21/5, d23/5 | 3.8 |
| Prior infection/cross protection | 5000 | B.1.427 t then at 21 days PI B.1.427 | - | d2/5, d21/5, d23/5 | 3.8 |
| Prior infection/cross protection | 5000 | B.1(614G) then at 21 days PI B.1.427 | - | d23/5 | 3.8 |
| Prior infection/cross protection | 5000 | B.1(614G) then at 21 days PI B.1.429 | - | d23/5 | 3.8 |
| | | | | | |
| Airborne transmission | $10^4$ | WA-1 | donors: d1<br>sentinels: DPE 0.5 -14 | donors: d 7 or 8/8<br>sentinels: up to DPE 14/8 | 3.9 |
| Airborne transmission | $10^4$ | B.1.(614G) | donors: d1<br>sentinels: DPE 0.5 -14 | donors: d 7 or 8/8<br>sentinels: up to DPE 14/8 | 3.9 |
| Airborne transmission | $10^4$ | B.1.427 | donors: d1<br>sentinels: DPE 0.5-14 | donors: d 7 or 8/8<br>sentinels: up to DPE 14/8 | 3.9 |
| Airborne transmission | $10^4$ | B.1.429 | donors: d1<br>sentinels: DPE 0.5 -14 | donors: d 7 or 8/8<br>sentinels: up to DPE 14/8 | 3.9 |




**Supplemental Figure S.3.1. sgRNA levels isolated from mixed infections of B.1 (614G) and B.1.427.** sgRNA isolated from mixed infections of B.1 (614G) and B.1.427 at 1:1 (blue) or 9:1 (green) ratios or G14G and 6 VOC cocktail (black) at indicated days post infection. sgRNA is isolated from **(A)** oral swabs, **(B)** URT washes or **(C)** lung lobes. Each data point represents one animal.

**References**

1. CDC (2021) SARS-CoV-2 Variant Classifications and Definitions. https://www.cdc.gov/coronavirus/2019-ncov/variants/variant-info.html: Centers for Disease Control.

2. Otto SP, Day T, Arino J, Colijn C, Dushoff J, et al. (2021) The origins and potential future of **SARS-CoV-2 variants of concern in the evolving COVID-19 pandemic. Curr Biol 31: R918-R929.**

3. Gomez CE, Perdiguero B, Esteban M (2021) Emerging SARS-CoV-2 Variants and Impact in Global Vaccination Programs against SARS-CoV-2/COVID-19. Vaccines (Basel) 9.

4. Harvey WT, Carabelli AM, Jackson B, Gupta RK, Thomson EC, et al. (2021) SARS-CoV-2 variants, spike mutations and immune escape. Nat Rev Microbiol 19: 409-424.

5. Deng X, Garcia-Knight MA, Khalid MM, Servellita V, Wang C, et al. (2021) Transmission, infectivity, and neutralization of a spike L452R SARS-CoV-2 variant. Cell 184: 3426-3437 e3428.

6. WHO (2021) Tracking SARS-CoV-2 variants. https://www.who.int/en/activities/tracking-SARS-CoV-2-variants/: World Health Organization.

7. Wu K, Werner AP, Koch M, Choi A, Narayanan E, et al. (2021) Serum Neutralizing Activity Elicited by mRNA-1273 Vaccine. N Engl J Med 384: 1468-1470.

8. McCallum M, Bassi J, De Marco A, Chen A, Walls AC, et al. (2021) SARS-CoV-2 immune evasion by the B.1.427/B.1.429 variant of concern. Science.

9. Boudewijns R, Thibaut HJ, Kaptein SJF, Li R, Vergote V, et al. (2020) STAT2 signaling restricts viral dissemination but drives severe pneumonia in SARS-CoV-2 infected hamsters. Nat Commun 11: 5838.

10. Munoz-Fontela C, Dowling WE, Funnell SGP, Gsell PS, Riveros-Balta AX, et al. (2020) Animal models for COVID-19. Nature 586: 509-515.

11. Chan JF, Zhang AJ, Yuan S, Poon VK, Chan CC, et al. (2020) Simulation of the Clinical and Pathological Manifestations of Coronavirus Disease 2019 (COVID-19) in a Golden Syrian Hamster Model: Implications for Disease Pathogenesis and Transmissibility. Clin Infect Dis 71: 2428-2446.

12. Imai M, Iwatsuki-Horimoto K, Hatta M, Loeber S, Halfmann PJ, et al. (2020) Syrian hamsters as a small animal model for SARS-CoV-2 infection and countermeasure development. Proc Natl Acad Sci U S A.

13. Zhou B, Thao TTN, Hoffmann D, Taddeo A, Ebert N, et al. (2021) SARS-CoV-2 spike D614G change enhances replication and transmission. Nature 592: 122-127.

14. Yinda CK, Port JR, Bushmaker T, Fischer RJ, Schulz JE, et al. (2021) Prior aerosol infection with lineage A SARS-CoV-2 variant protects hamsters from disease, but not reinfection with B.1.351 SARS-CoV-2 variant. Emerg Microbes Infect 10: 1284-1292.

15. Brocato RL, Principe LM, Kim RK, Zeng X, Williams JA, et al. (2020) Disruption of Adaptive Immunity Enhances Disease in SARS-CoV-2 Infected Syrian Hamsters. bioRxiv 20200619161612.

16. Korber B, Fischer WM, Gnanakaran S, Yoon H, Theiler J, et al. (2020) Tracking Changes in SARS-CoV-2 Spike: Evidence that D614G Increases Infectivity of the COVID-19 Virus. Cell 182: 812-827 e819.

17. Faria NR, Mellan TA, Whittaker C, Claro IM, Candido DDS, et al. (2021) Genomics and epidemiology of the P.1 SARS-CoV-2 lineage in Manaus, Brazil. Science 372: 815-821.

18. Davies NG, Abbott S, Barnard RC, Jarvis CI, Kucharski AJ, et al. (2021) Estimated transmissibility and impact of SARS-CoV-2 lineage B.1.1.7 in England. Science 372.

19. Madhi SA, Baillie V, Cutland CL, Voysey M, Koen AL, et al. (2021) Efficacy of the ChAdOx1 nCoV-19 Covid-19 Vaccine against the B.1.351 Variant. N Engl J Med 384: 1885-1898.

20. Port JR, Kwe Yinda C, Avanzato VA, Schulz JE, Holbrook MG, et al. (2021) Increased aerosol transmission for B.1.1.7 (alpha variant) over lineage A variant of SARS- CoV-2. bioRxiv.

21. Teng S, Sobitan A, Rhoades R, Liu D, Tang Q (2021) Systemic effects of missense mutations on SARS-CoV-2 spike glycoprotein stability and receptor-binding affinity. Brief Bioinform 22: 1239-1253.

22. Chen J, Wang R, Wang M, Wei GW (2020) Mutations Strengthened SARS-CoV-2 Infectivity. J Mol Biol 432: 5212-5226.

23. Nunez IA, Lien CZ, Selvaraj P, Stauft CB, Liu S, et al. (2021) SARS-CoV-2 B.1.1.7 Infection of Syrian Hamster Does Not Cause More Severe Disease, and Naturally Acquired Immunity Confers Protection. mSphere: e0050721.

24. Abdelnabi R, Boudewijns R, Foo CS, Seldeslachts L, Sanchez-Felipe L, et al. (2021) Comparing infectivity and virulence of emerging SARS-CoV-2 variants in Syrian hamsters. EBioMedicine 68: 103403.

25. Carsana L, Sonzogni A, Nasr A, Rossi RS, Pellegrinelli A, et al. (2020) Pulmonary post-mortem findings in a series of COVID-19 cases from northern Italy: a two-centre descriptive study. Lancet Infect Dis 20: 1135-1140.

26. Mosleh W, Chen K, Pfau SE, Vashist A (2020) Endotheliitis and Endothelial Dysfunction in Patients with COVID-19: Its Role in Thrombosis and Adverse Outcomes. J Clin Med 9.

27. Ackermann M, Verleden SE, Kuehnel M, Haverich A, Welte T, et al. (2020) Pulmonary Vascular Endothelialitis, Thrombosis, and Angiogenesis in Covid-19. N Engl J Med 383: 120-128.

28. Calabrese F, Pezzuto F, Fortarezza F, Hofman P, Kern I, et al. (2020) Pulmonary pathology and COVID-19: lessons from autopsy. The experience of European Pulmonary Pathologists. Virchows Arch 477: 359-372.

29. Naccache SN, Federman S, Veeraraghavan N, Zaharia M, Lee D, et al. (2014) A cloud-compatible bioinformatics pipeline for ultrarapid pathogen identification from next-generation sequencing of clinical samples. Genome Res 24: 1180-1192.

30. Miller S, Naccache SN, Samayoa E, Messacar K, Arevalo S, et al. (2019) Laboratory validation of a clinical metagenomic sequencing assay for pathogen detection in cerebrospinal fluid. Genome Res 29: 831-842.

31. Martin M (2011) Cutadapt removes adapter sequences from high-throughput sequencing reads. EMBnetjournal 17: 10-12.

32. Schmieder R, Edwards R (2011) Quality control and preprocessing of metagenomic datasets. Bioinformatics 27: 863-864.

33. Port JR, Yinda CK, Owusu IO, Holbrook M, Fischer R, et al. (2020) SARS-CoV-2 disease severity and transmission efficiency is increased for airborne but not fomite exposure in Syrian hamsters. bioRxiv.

34. Corman VM, Landt O, Kaiser M, Molenkamp R, Meijer A, et al. (2020) Detection of 2019 novel coronavirus (2019-nCoV) by real-time RT-PCR. Euro Surveill 25.

35. Wolfel R, Corman VM, Guggemos W, Seilmaier M, Zange S, et al. (2020) Virological assessment of hospitalized patients with COVID-2019. Nature 581: 465-469.